Diagnostics and selective nano-therapeutics to combat multidrug-resistant bacteria

Partha Pratim Chowdhury

Master of Technology

Indian Institute of Technology Kharagpur

2014

A thesis submitted to the

Faculty of the Graduate School of the

University of Colorado Boulder in Partial fulfillment

Of the requirements for the degree of

Doctor of Philosophy

Department of Chemical and Biological Engineering

2019

This Thesis entitled:
Diagnostics and selective nanotherapeutics to combat multidrug resistant bacteria
written by Partha Pratim Chowdhury
has been approved by the Department of Chemical and Biological Engineering

_____
Chair: Prashant Nagpal

_____
Anushree Chatterjee

Date _____

The final copy of this thesis has been examined by the signatories, and we find that
both the content and the form meet acceptable presentation standards of scholarly
work in the above-mentioned discipline

Chowdhury, Partha Pratim (Ph.D. Department of Chemical and Biological Engineering)

Diagnostics and selective nanotherapeutics to combat multidrug resistant bacteria

Thesis directed by **Assistant Professor Prashant Nagpal**

Due to extensive use of antibiotics various strains multidrug resistant bacteria are emerging rapidly. In USA alone according to CDC report 2013 more than 2 million is affected by these strains of multidrug resistant bacteria causing several deaths. Hence an effective way of diagnostics and therapeutics need to be designed which can successfully combat the menace of multidrug drug resistant bacteria.

In the present thesis, we discuss about novel strategies for both diagnostics and therapeutics for multidrug resistant bacteria. In the 1st chapter we discuss a novel DNA sequencing technique utilizing purely optical spectroscopy techniques like surface enhanced Raman and FTIR spectroscopy using 3D plasmonic nano focusing. This technique can be effective in doing single molecular study, detecting any mutations or epigenetic influences that can result in development of multi drug resistance in bacteria.

In the 2nd chapter we show that among different ROS, only superoxide was found to be bactericidal, killing a range of multidrug-resistant (MDR) pathogens without affecting the viability or growth of mammalian cells. In our in vitro studies, intracellular superoxide generation using light-activated quantum dots yielded highly selective and effective antimicrobial action. These results can pave the way for rational design of nanoscale therapies as precision medicine.

In the 3rd chapter we show the design of superoxide-generating QDs using optimal QD material and size well-matched to superoxide redox potential, negatively charged ligands

tomodulate their uptake in cells and selective redox interventions, and core/shell structures to improve their stability for therapeutic action.

In the 4th chapter we discuss about alloy quantum dots lowering cadmium content and replacing it with more benign zinc content. Using QDs with low cadmium content as alternative candidates for selective light-activated therapy, we show negligible toxicity of these QDs to mammalian cells, while maintaining high treatment efficacy against MDR pathogens. These results provide design principles for developing different QDs as selective therapeutics to counter the growing threat of antimicrobial resistant infections.

Acknowledgements

I want to thank Dr. Annette Erbse for training me on Electron Paramagnetic Resonance and Fluorescence spectroscopy of biochem core.

I also want to express my gratitude to Prof. Hans Funke to let me use the centrifuge and muffle furnace in his lab. I want to thank Prof. Theodore Randolph to let me use the zetasizer in his lab for DLS and zeta potential measurement.

I also want to express my deepest gratitude to Dominique de Vangel for his assistance in various administrative aspects.

Finally, I want to thank my parents Sudatta Chowdhury and Tamal Tanu Chowdhury for their immense contribution and sacrifice in the process of making me who I am today.

Partha Pratim Chowdhury

Contents

Chapters

List of Figures

Chapter 1

Chapter 2

Chapter 3

Chapter 4

List of Tables

Chapter 1

Chapter 3

Chapter 1

Block Optical DNA Sequencing using Vibrational Spectroscopy as a diagnostic method

Introduction

DNA sequencing of single molecules can provide vital information about genetic heterogeneity and its role in defining bio- logical functions by controlling the downstream expression of genes, proteins, and other cell-regulatory processes.[1–4] Small variations in genetic coding across individual cells, both through mutations or epigenetic influences, play a key role in physiology and provide new targets for diagnostics, vaccine development, and therapeutics.[5–9] To realize the benefits of single-molecule sequencing, several fundamental elements of the technology must be further developed. Improvements would result from high-throughput and multiplexed data acquisition, data compression to rap- idly extract useful information from large sets of raw sequence data, and a novel platform that does not rely on expensive labels or sample preparation.[10] Optical sequencing of DNA (deoxy ribonucleic acid) addresses these elements with parallel optics and data acquisition, multiplexed label-free probes, and inexpensive processing steps. To achieve this, light photons with several hundred-nanometer wavelengths must be squeezed into molecular length-scales, photon interactions with single molecules must be measured using

optical spectroscopy and multiplexed parallel probes must be developed for simultaneous reading. Characterization of optical measurements could then be used as robust fingerprints for DNA sequence identification. Storing and analyzing massive amounts of sequence data can create potential issues. [3,4] For example, storing single DNA nucleotide letters (adenine (A), guanine (G), cytosine (C), and thymine (T) for a nominal human genome requires several gigabytes of space per sequence so 100 DNA sequences need terabytes of space and data mining to extract useful information. Similarly, a few thousand bacterial genomes to map the microbiome would require similar space and data processing. To remedy this, data compression techniques use lossless and lossy compression. Here, we show advances toward a proposed label-free, high-throughput block optical sequencing (BOS) method with inherent lossy compression, where k-mer blocks of DNA are read using 3D (3 dimensional) nano-focusing of light.

Since the different nucleobases in DNA are biochemically distinct, their unique interactions with light photons (observable optical fingerprints) can be used to discriminate them.[11−15] Surface-enhanced Raman spectroscopy (SERS) is an optical method routinely used for identification of unknown chemical and biochemical compounds from their vibrational fin-gerprints.[13,16−18] In this technique, surface plasmon polaritons lead to 3D nano-focusing and enhancement of near field signal at the apex of rough features or patterned nanostructures. Applying SERS, or tip-enhanced Raman spectroscopy (TERS), for reproducible single-molecule DNA sequence identification has proven difficult. Previous studies have used SERS/ TERS measurements on DNA for label-free chemical fingerprinting; however, mixing of a large number of DNA molecules with metal nanoparticles provides an ensemble spectra and poses uncertainties in signal strengths.[11−15] Furthermore,

DNA molecules have varied enhancement due to differences in their location from the plasmonic antenna, and thus suffer from low reproducibility. Since the SERS/TERS signal falls off dramatically with distance from the plasmonic antenna, it makes signal amplitudes highly sensitive to the orientation and conformation of molecules with respect to the surface. While many of these effects are washed out in an ensemble detection, it has been shown that the SERS/TERS signal strength and reproducibility are severely affected by the packing fraction and large uncontrollable variation in molecular orientation with respect to the plasmonic nano- structure. Thus, single-molecule label-free identification of DNA nucleobases remains an important and critical challenge.[19–21] In this study, we used patterned nanopyramid probes on a multiplexed substrate to reproducibly enhance "optical fingerprints" of DNA nucleotides.[22–28] Identifying the different molecular vibrations, bond stretches, and rocking motions in these reproducible spectra allowed us to differentiate the nucleobases from their respective spectral fingerprints, with improvements seen by combining Raman with Fourier-transform infrared (FTIR) spectroscopy.

Characterization and Observations

We designed a substrate with metal pyramids at 2 µm periodicity (square periodic pattern, 2 µm in both *x* and *y* direction, **Figure 1**a; Figure S1, (Supporting Information) to enhance vibrational signal using the fingerprinting region of the mid-IR region. Figure S1 of the Supporting Information shows confocal spectra signal from designed tips with pixel-limited resolution.

To confirm the resolution of our nanopyramid tips, we collected Raman spectroscopy measurements on a self-assembled monolayer of benzenethiol with and without

nanopyramids (Figure 1b). Previous studies have demonstrated the signal enhancement can be on the order of 10^7–10^{10}.[17,23] Furthermore, we drop- casted homologous adenine oligomers on nanopyramids at low concentrations (10×10^9 to 100×10^9 m) and compared the Raman spectra with a tenfold higher concentration on flat silver (Figure 1c), which also showed significant signal enhancement. While focusing on Raman spectroscopy, we demonstrate that coupled FTIR spectroscopy can help increase nucleobase identification. Each of these vibrational spectroscopy techniques shows distinct peaks from four DNA nucleotides and characterizes different properties. Raman and FTIR spectra characterize the change in bond polarizability and polarization (or dipole moment) with bond vibrations, respectively, are complementary, have different selection rules, differ in intensity even for the same bond vibrations, and are affected by symmetry and orientation of the single molecules probed.[18] As seen in the plasmon peaks for Raman spectroscopy (Figure 1d) and FTIR spectroscopy (mid-IR region, Figure 1e), the designed metal nanostructures lead to broadband enhancement of probed vibrational spectra as optical fingerprints. An important consideration when dealing with biological samples is possible contamination from the abundance of biomolecules in the cellular environment. Most notably, the presence of protein contaminants prevents DNA sequence identification from current sequencing methods. To test the extent at which bio- molecule contaminants disrupt the optical spectra from DNA, we collected Raman spectra on deoxyadenosine triphosphate (dATP) nucleotides mixed with glycine up to equimolar concentrations. As the ratio of glycine to nucleotides increased, the peak intensities (measured by integrated area under the curve) decreased, but were never extinguished. Figure 1f shows the normalized area versus the glycine-dATP molar ratio for a representative adenine peak around 995 cm^{-1}. A direct

comparison of the full Raman spectra for pure dATP and for equimolar glycine and dATP is given in Figure 1g. This provides evidence that the optical vibrational spectroscopic techniques are robust, with signal remaining strong up to significant levels of contamination.

Raman spectra for optical fingerprints were collected from four homologous nucleic acid oligomers: poly(dA)$_{16}$, poly(dG)$_{16}$, poly(dC)$_{16}$, and poly(dT)$_{16}$. The spectra contain several vibra- tional features that are marked as either strong modes (A$_1$, A$_2$, etc.) or weaker modes (a$_1$, a$_2$, etc.).
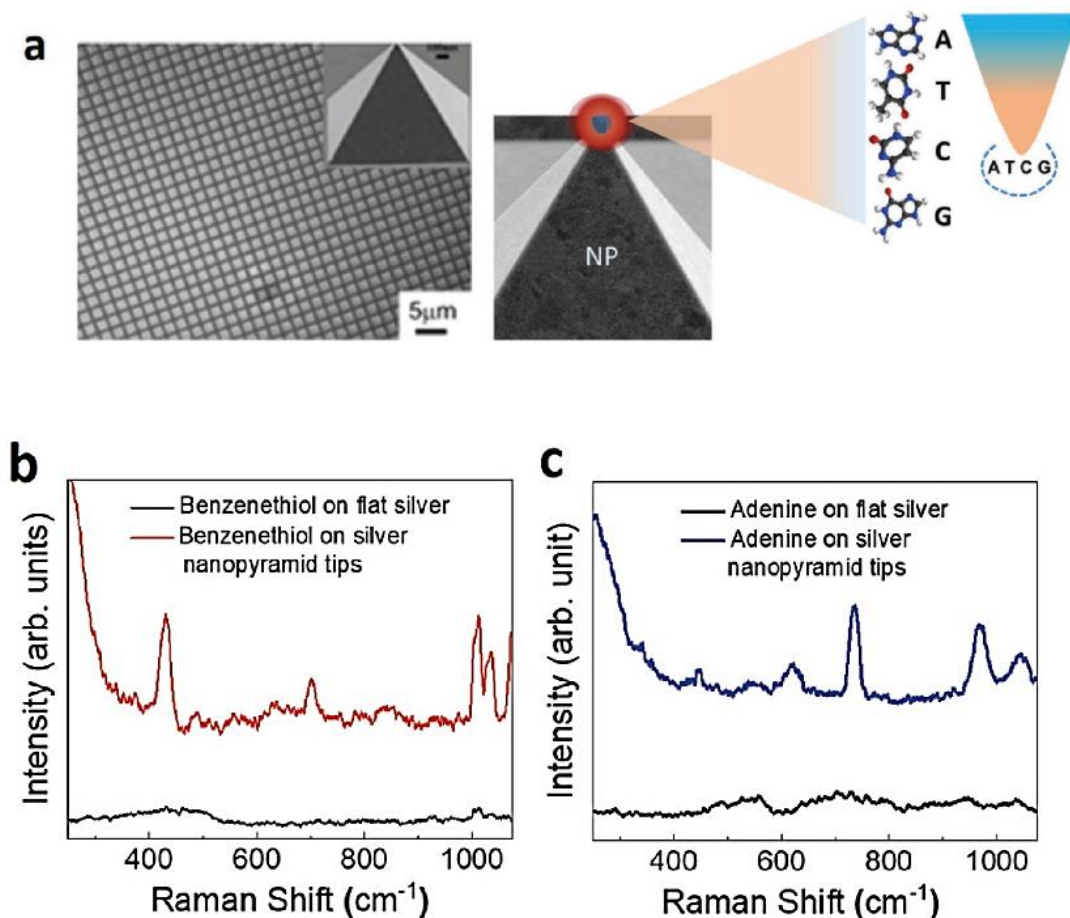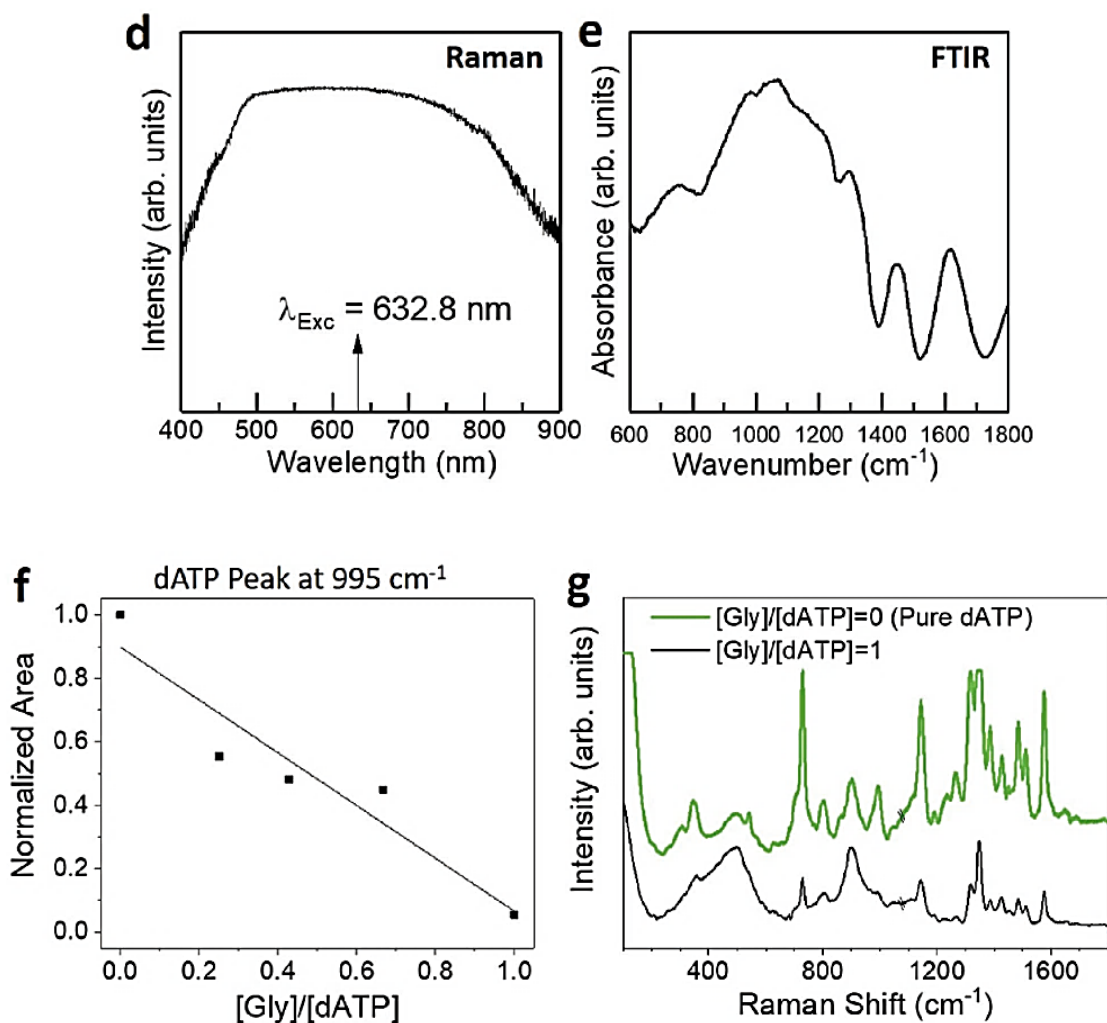
Figure 1. Design of multiplexed nanopyramid probes for robust optical DNA sequencing.a) SEM image of nanopyramids (left) and a schematic of DNA molecules on the nanopyramid tips (center) for block optical sequencing. Additivity of signal from k-mer blocks of nucleotides allows for block optical DNA sequencing. b) Surface-enhanced Raman signal for benzenethiol molecules on silver nanopyramid tips. c) Surface-enhanced Raman signal for adenine k-mers on nanopyramid tips. Raman signal of adenine on nanopyramids is much stronger than a tenfold higher concentration of adenine on a flat silver surface. d,e) IR and visible extinction spectra for surface plasmon resonance of the nanopyramids. The position of the Raman excitation laser is marked at 632.8 nm. Uniform Raman enhancement of all modes was attributed to the broad plasmon enhancement around the Raman excitation laser (for both Stokes and antiStokes scattering), whereas several plasmon peaks in the IR region correspond

well with selective (or plasmon enhancement) of respective IR vibrational peaks. f) Normalized integrated area for a single Raman peak in the spectra for dATP as the molar ratio of a glycine contaminant increases. g) Direct comparison of Raman spectra from pure dATP and equimolar glycine and dATP, indicating that the presence of biomolecule contaminants does not significantly affect Raman signal from DNA nucleotides. Dashes in the spectra indicate where the low- and high-shift regions were spliced together. These spectra were collected on a flat glass substrate, and therefore do not show the same Raman enhanced peaks seen for adenine k-mers on the silver nanopyramid substrate.

As shown in **Figure 2**a, the strong Raman mode marked A_1 occurs due to hydrogen bonding; mode A_2 occurs due to a bending mode for C-C=C; mode A_3 occurs due to a bending mode for N-C-C; mode A_4 occurs due to stretching of C-C and C-N in-phase.[29–32] The Raman spectra also show mode A_5, which occurs due to bending of N-C=N (peak is shifted by 20 to 964 cm^{-1}). The peak shift can be attributed to the presence of residual water (even after samples are dried) and was expected. The peak corresponding to mode A_6 was assigned to the bending mode of C-N-C bonds, but it is shifted by 10 cm^{-1} from regular dried adenine nucleotide spectra. A similar shift of 10 cm^{-1} occurred for mode A_7 due to the bending motion of C2-N1=C6 and the stretching motion of C5-N7=C8 (see details and numbering of the biochemical structure in Figure S2, Supporting Information), which has been attributed to the presence of water molecules. Some small shifts have also been observed in modes A_8 and A_9 (stretching modes of C-N and C=N) and were also attributed to the presence of residual water. Other weaker modes with smaller Raman intensities were observed such as a_1 (skeletal mode, in-plane), a_2 (CH bending, in-plane), and a_3. All of these vibrational modes can be used to easily identify the biochemical structure of the adenine

nucleotide, and they are seen reproducibly in multiple tips across the substrate (Figure S3, Supporting Information). From the thymine spectra shown in Figure 2b, clear differences in purine and pyrimidine biochemical species can be seen. Raman modes T_1, T_2, and T_3 occur due to bending vibrations in OH···O, N-C=C, and N-C-C bonds.[30–33] Stretching modes in thymine include T_4 due to stretching of C5–CH_3, and T_5 due to stretching of C4-C5. Two other bending modes observed in the thymine spectra are T_6 (due to bending of C-N-C) and T_7 (due to bending of N-C-H). Other weaker modes such as τ_1 and τ_2 observed for thymine corresponds to bending of C-C=C (in the presence of water) and bending of C5-C-H, respectively.

Careful analysis of Raman fingerprints for cytosine (Figure 2c) reveals several strong bending modes C_1-C_5 (C_1 due to N3-C2=O and N1-C2=O bending; C_2 due to C2-N1-C6 and N3=C4-C5 bending; C_4 due to C-C=C and N3=C4-N4 bending; and C_5 due to C2-N3=C4 and N1-C2-N3 bending) as well as several strong stretching modes (C_6 due to C=O in- phase stretch; strongest mode C_8 is a breathing mode; C_{10} due to bond C4-C5 stretching).[30–32,34] Furthermore, the spectra reveal some weaker bond bending Raman modes χ_1–χ_4 (c_2 as a result of C5-C4-N4 bending; χ_3 as a result of C4-C5-H in- plane bending; χ_4 as a result of N1-C6-H in-plane bending). Analyzing the complementary pyrimidine, guanine (Figure 2d), we identified bending modes (G_1 due to C=O bending; G_2 due to N9-C4=C5 and N7-C=C4 bending; γ_1 due to N3-C4=C5 bending; G_3 due to C=C=C bending; G_5; γ_3 due to N9-H out- of-plane bending; G_7 due to N-C=N and N-C-N bending; G_8; G_9; G_{10}), a breathing mode (G_4), and stretching modes (G_6 due to C-C stretching; G_{11} due to C2-

8

NH$_2$ stretching).[30–32,35] Table S1 of the Supporting Information summarizes all Raman spectroscopy peaks.

To establish the reproducibility of optical fingerprints from Raman spectroscopy, we characterized the peaks obtained from several tips in the million-plexed device (over $4 * 10^6$ tips were fabricated on each substrate using optical lithography), by changing the field of view and looking at several tips individually. In Figure S3 of the Supporting Information, we present Raman spectroscopy data for all four DNA nucleotides as arising from randomly selected nanopyramids. For a given spectrum, the autocorrelation ratios of the various peaks are fairly constant and exhibit very small variations in signal (relative peak heights) from tip to tip (Figure S1, Supporting Information). It is important to establish the amount of signal amplitude variation between the tips and further establish that the ratios of the Raman vibrational features remain constant from peak to peak. It is also important to point out that for high-throughput sequencing applications, neither collecting spectra with extremely low signal-to-noise nor scanning the entire fingerprinting window is necessary. High accuracy can be achieved with simple measurements, as we demonstrate later.

We also collected FTIR spectra for each nucleobase from the four homologous nucleic acid oligomers (Figure 2) and identified several important peaks. While some peaks were common between Raman and FTIR spectra (e.g., comparing adenine optical fingerprints in Figure 2a, α_2 and A$_4$ modes both show bending motion of C-C and C-N bonds in-phase, α_5 and A$_5$ modes show the bending motion of the N-C=N bond, and α_7 and A$_7$ modes show bending motion of C2-N1=C6 and the stretching motion

of C5-N7=C8), several new complementary modes (e.g., adenine FTIR fingerprints α_1, α_3, α_4, α_6, α_8, α_9, α_{10}, α_{11}, α_{12}, and α_{13}) are seen in the FTIR spectra.[29,36] For example, modes α_{10} and α_{13}, which are not seen in Raman spectra; α_{10} occurs due to the stretching mode of the imidazole ring, and α_{13} shows the bending mode of NH_2. Similarly, the modes α_3 (C-C stretching), α_4 (N9-H out-of-plane bending), α_9 (C2-H and C8-H out-of-plane bending, and N=C-H bending), α_{11} (C-N9-H bending), α_{12} (C=N and C=C stretching) are too weak and unlikely to be observed in Raman spectra, but are strongly seen in corresponding FTIR spectra. Therefore, when combined together, Raman and FTIR spectra can provide unique and complementary biochemical optical fingerprints for DNA sequencing.

Cytosine, guanine, and thymine also show peaks in the FTIR spectra (Figure 2b–d) that are not seen in Raman spectra due to small peak intensities. In cytosine, peak χ_1 arises due to N-H out-of-plane bending and is not seen in Raman optical spectra.[34,36] Peaks χ_3 (NH_2 rocking), χ_4 (C4-N4 stretching), χ_5 (C=C-H bending), χ_6 (C4-N3 and C2-N3 stretching), χ_7 (C4=N3 and C4-N4 stretching), χ_8 (C5=C6 stretching), and χ_9 (NH_2 bending) are not observed prominently in Raman spectra likely due to small intensities. In thymine, peak τ_2 occurs due to out-of- plane N-H bending, whereas peak τ_{12} occurs due to stretching of C4=O and C2=O.[33,36] Both of these peaks are Raman inactive. Furthermore, peaks τ_7 (C-N stretching), τ_9 and τ_{10} (broad N1-H and N3-H bending) have much stronger peaks in FTIR than in Raman spectra. Similar analysis of guanine shows peaks γ_1 and γ_3 (N1-H bending) are Raman inactive, whereas peaks γ_2 (ring bending), γ_4 (C-C stretching), γ_6 (NH_2 rocking), γ_{10} (N7=C8 and C8-C9 stretching), γ_{12} (C=O stretching), and γ_{13} (C=O stretching and NH_2

bending) have stronger intensities in the FTIR spectrum.[35,36] Table S2 of the Supporting Information summarizes all FTIR spectroscopy peaks.

To be useful as a sequencing platform, our proposed BOS method must be able to decipher mixed DNA sequences (those containing a mix of all bases A, G, C, and T, as opposed to merely the homologous sequences used for developing fingerprints as described above). Differences in respective Raman cross-sections between the various DNA nucleotides, as well as conformational entropy, pose important challenges for facile sequencing of mixed DNA sequences using optical fingerprints. In the Raman spectra for a repeating 4-mer DNA oligomer poly $(dATGC)_4$ in Figure 2e, peaks can be seen from adenine (A_0, A_1, A_2, A_3, A_4, A_5, and A_6), guanine (G_1, G_2, G_3, G_4, G_5, G_6, G_8 and G_9), cytosine (C_1, C_2, C_4, C_5, C_7, C_8 and C_9), and thymine (T_0, T_3, T_4, T_5 and T_6). While the linearity of peaks with varying amounts of respective nucleotide content has been shown in ensemble studies,[11−15] where the different conformation and orientation effects cancel out, it can pose a challenge for single-molecule spectra for BOS. Also, since the resulting plasmonic interaction can vary strongly depending on strength of plasmon enhancement (between nanoparticles and different plasmonic structures), the reproducibility in design of tips is extremely important for the development of reproducible and robust sequencing. We have already shown that between different substrates made from the same mold, there is reproducible plasmon enhancement and vibrational spectroscopic features (Figures S1 and S3, Supporting Information), which was also seen in prior studies using template stripped structures. Therefore, we use this reproducibility to identify the nucleobase content in mixed DNA k-mers, which includes nucleobases present and their relative fraction.
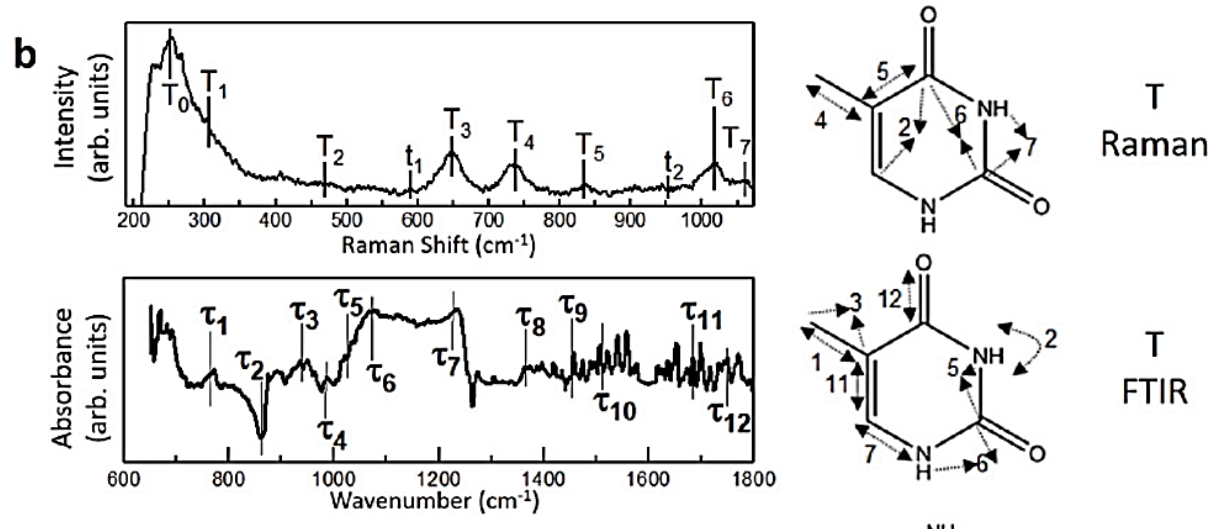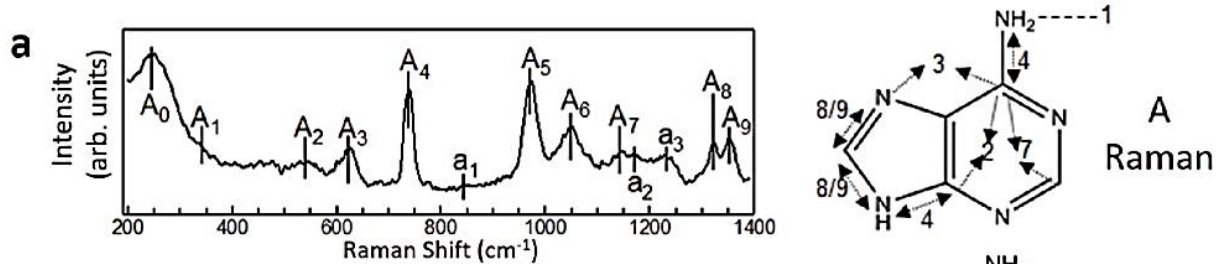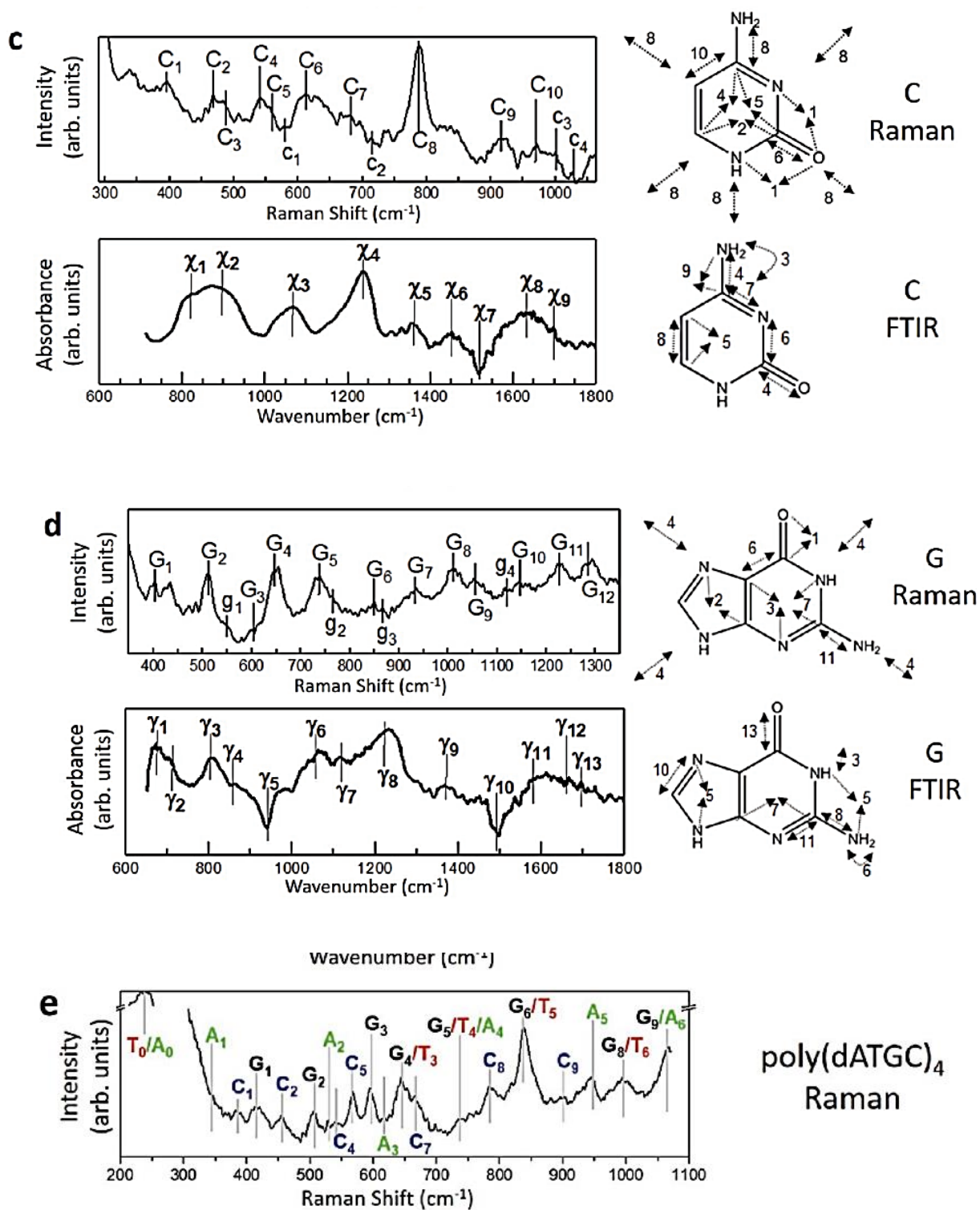
Figure 2. Identification of Raman and FTIR peaks as optical fingerprints for DNA nucleobases: a) adenine, b) thymine, c) cytosine, and d) guanine. The strong modes are marked in uppercase letters, while the weak modes are in lowercase letters. The corresponding chemical structures

show the specific vibrations (bond bending shown using arrows, bond stretching and ring breathing shown using double arrows) associated with numbered peaks for respective nucleobases. e) Raman spectra for a DNA oligomer of repeating ATGC, poly(dATGC)4. Peaks from all nucleobases can be seen contributing to the overall signal.

To analyze our ability to identify nucleobases from their characteristic spectra (base calling), we developed algorithms described in the Experimental Section and **Figure 3**a–c. To establish fingerprints, Gaussian curves were fit to block k-mer spectra (Raman and FTIR) from homologous sequences, allowing the center location and corresponding full width at half maximum (FWHM) to be determined for each characteristic peak in the spectra (i.e., adenine in Figure 3a). For homologous k-mer block identification, only a subset of spectra peaks for each nucleobase are considered (also noted in Figure 3a), and base calls are then made for whichever nucleobases show the largest intensity (largest integrated area) in the unknown spectra. To identify the nucleobases, present in mixed k-mer blocks, we used specific Raman peaks that consistently appear when each of the nucleobases is in a given k-mer (A_3, A_4, A_5; G_4, G_6; C_8; T_3, T_4). Following identification of which nucleobases are present, relative fractions can be determined from known correlations of calculated Raman peak intensity (integrated area under the curve for all major peaks) with actual mix fraction (Figure 3b,c). Note that only three correlations (A, C, T) are needed as the fourth (G) is determined from the remainder.

To test the algorithms and support our proposed optical DNA sequencing method, we input known sequence block k-mer spectra into the algorithms as though they were unknown and observed if correct base calls were made. For homologous sequences, 99 measured spectra for each A, T, G, and C (396 total spectra from single

pixels) were used for testing the BOS algorithmic method. When only relying on Raman spectroscopy, we correctly base called 100% of A and C k-mer spectra, 88.9% of G k-mer spectra, and 96.0% of T k-mer spectra. When Raman spectroscopy and FTIR spectroscopy were combined, we achieved 100% base calling accuracy for all A, T, G, and C k-mers. Base calling for a subset of 28 spectra is shown in Figure 3d,e, and for all 396 total spectra in Figures S4 and S5 of the Supporting Information. The advantage of using the two complementary vibrational spectroscopy techniques can also be seen when analyzing the base calling performance using confusion matrices (Figure 3f). This method characterizes not only the accuracy of correct base calls but also false-positive and false-negative calls. When com- paring the confusion matrix analysis of Raman and combined Raman–FTIR spectroscopy, we observed clear improvement in base calling accuracies using the combined spectra, especially for guanine and thymine nucleobases. To further quantify the precision of DNA base calling from optical spectroscopy measurements, we used confidence in base calling as another important metric in addition to call accuracy.

The confidence in calling a particular base can be calculated using the probability values from the base calling algorithm: $C_i = (P_i - P_j)/P_i$. Here, C_i is the confidence for calling base i, P_i is the probability value associated with the called base, and P_j is the second highest probability(for the second most probable base). This confidence also characterizes the signal-to-noise level. As highlighted in Figure 3d,e, combining Raman and FTIR data not only improves accuracy, but increases confidence for base calling all nucleobases (A: 0.948 (0.02) to 0.980 (0.01), G: 0.196 (0.12) to 0.539 (0.08), C: 0.798 (0.12) to 0.937 (0.04), T: 0.478 (0.14) to 0.758 (0.13)). For mixed sequences, a variety of DNA oligomers were analyzed: poly(dAC)$_8$, poly(dGC)$_8$, poly(dCT)$_8$, poly(dAGC)$_5$, and poly(dATGC)$_4$.

Figure 3g shows our ability to identify which nucleobases are present in a mixed k-mer at an average of 79% accuracy from single pixels. This mixed sequence recognition analysis provides additional evidence for block optical DNA sequencing. Applicability could be further expanded to include epigenetic analyses, since previous studies have shown the ability of Raman spectroscopy to detect modified nucleobases. [14,37]

a

Raman Spectra Fitting

— Adenine spectra
— Gaussian fit

Intensity (arb. units) vs Raman shift (cm^{-1})

Raman Peaks Used

Peaks	A	G	C	T
1			X	
2		X		
3	X			
4			X	
5	X			X
6	X			X
7		X		
8		X	X	
9			X	
10				
11				
12				

FTIR Peaks Used

Peaks	A	G	C	T
1			X	X
2				X
3		X		X
4				
5	X	X	X	
6				
7				
8			X	
9	X	X		X
10		X		
11	X			
12				
13				

b

Fraction of Mixed k-mer vs Normalized Integrated Area

T_3, T_4, T_5, T_6

All T Peaks
— Linear Fit
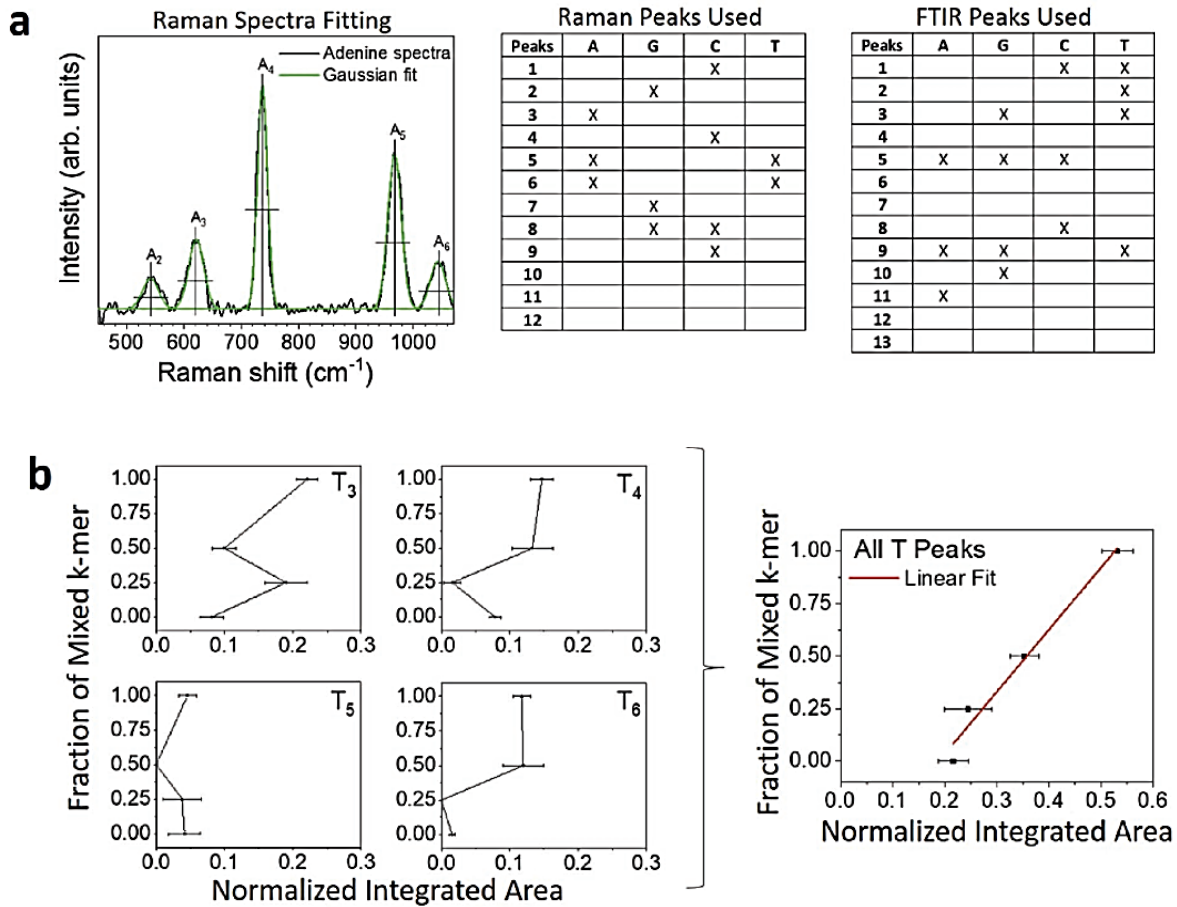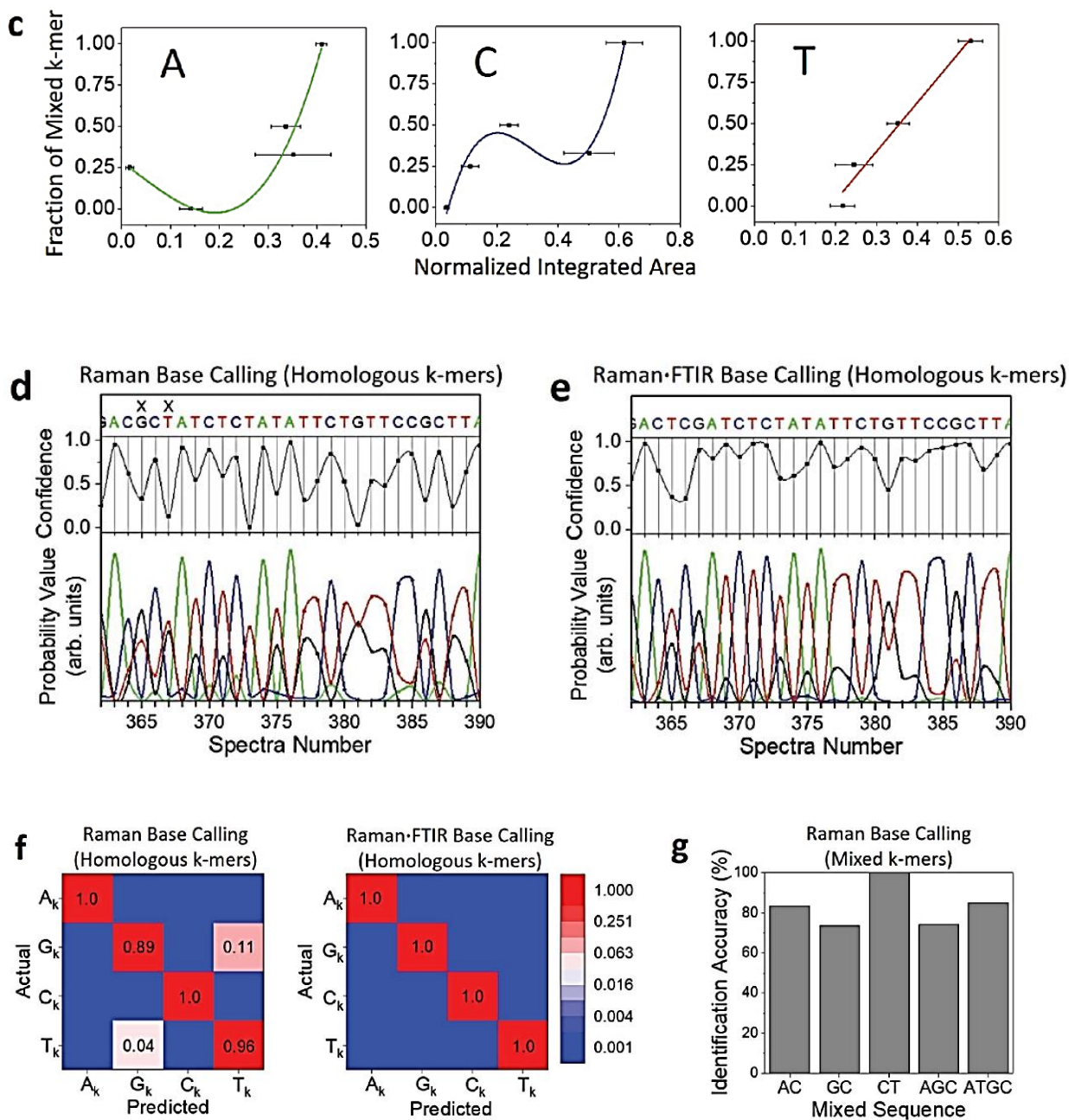
Figure 3. Base calling DNA k-mer blocks. a) Fitting and characterizing homologous block k-mer spectra peaks for use as fingerprints for base calling. Using adenine Raman spectra as an example (shown on the left), we ft Gaussians to all characteristic peaks, allowing us to determine the center location and corresponding FWHM for each. Only the most unique peaks (shown with an *x* in the tables on the right for both Raman and FTIR) were used in the base calling analysis as fingerprints for homologous sequences. To identify unknown spectra

obtained from Raman and FTIR measurements, the spectra are compared with the fingerprints in terms of the area under the respective fingerprinting peaks. For Raman data, this represents the total number of scattered photons by the specific mode. b) All major spectra peaks are used for base calling mixed k-mer blocks. As shown for thymine, single peaks do not show consistent trends (left); however, when combined the trends become favorable for fractional identification (right). c) Calibration curves used to deduce the relative fraction of each nucleobase in a mixed sequence k-mer. Only three (A, C, and T) calibration curves are needed, as the fourth (G) can be found from the remainder. d) Probability values (obtained from the base calling algorithm), the confidence of base calling, and accuracy (*X* indicates incorrect calls) using only Raman spectra to identify homologous k-mer blocks of each nucleobase. e) Improved confidence and accuracy in base calling homologous k-mer blocks can be seen by combining Raman and FTIR spectra. f) Summary of base calling accuracy for 396 measured homologous k-mer block spectra (99 each for A, T, G, and C) using combined Raman and FTIR spectroscopy. g) High accuracy for identifying nucleobases in various mixed sequence k-mer blocks

As previously noted, the nanometer-scale mode volumes demonstrated for SERS and TERS permit the collection of spectra from single DNA molecules; however, the angstrom scale nucleotides prevent single letter resolution for DNA sequencing. We have therefore demonstrated that a robust optical vibrational spectroscopic method (namely, Raman spectroscopy, and also coupled Raman and FTIR spectroscopy) can be used to acquire fingerprints of DNA nucleobases, and be applied to achieve accurate identification of mixed sequence DNA k-mers. This paves the way for a BOS method (Figure 1a), where k-mer blocks are read instead of single letters. Although single letters are not directly determined, a sequence can still be deduced from a raster scanning approach. Furthermore BOS can be applied for high-throughput identification of specific genes and biomarkers, where an exact sequence is not necessary. For example, a 5–8 nm resolution [38] for a single stranded DNA sample (≈4–6 Å

inter nucleotide separation) will lead to the identification of 8- to 12-mers, or blocks of 8–12 DNA nucleotides. For a DNA sequence of length N, the expected number of random matches to a particular k-mer is given by the expression $(N - k + 1)/4^k$. To find a unique k-mer (i.e., a k-mer that is expected to occur only a single time or less) in a sequence of length N, the expression can be made into an inequality $(N - k + 1)/4^k \leq 1$ and solved for k. For a human genome ($N = 3 \times 10^9$ base pairs), $k \approx 16$ meaning that a particular 16-mer is expected to occur only once within the genome. Since BOS gives A, T, G, and C content and not a sequence, for signal detection from 10-mers the least number of continuous BOS reads giving a unique block in a genome would be two if the 10-mers were all the same letter (e.g., AAAAAAAAAA, or ten T's, G's, or C's in any order). When the 10-mers are of a single nucleobase, there are no other possible permutations and the expectation of seeing the 10-mer is $\frac{1}{4} \times \frac{1}{4} \times \frac{1}{4} \times \frac{1}{4} \times \frac{1}{4} \times \frac{1}{4} \times \frac{1}{4} \times \frac{1}{4} \times \frac{1}{4} \times \frac{1}{4} = 1/4^{10}$. Therefore, two continuous 10-mers need to be detected. $(3 \times 10^9 \text{-}10 + 1)/(4^{10})^2 \approx 3 \times 10^9/(1.1 \times 10^{12}) < 1$. For cases with one different nucleobase within the 10-mer, there is a probability of other permutations giving rise to the same BOS signal. For other combinations of 10-mers, expectation is even higher. For instance, seven A's, one C, one T, and one G (in any order) yields the same spectra and leads to an expectation of $(10! / 7!1!1!1!)/4^{10} = 720/4^{10}$ due to the 720 possible 10-mer permutations. The highest number of possible permutations for a 10-mer (leading to the most continuous BOS reads necessary to achieve a unique sequence) occurs with three nucleotides each for two of the letters (e.g., A and T) and two nucleotides each for the other two letters (e.g., G and C), where the expectation is $(10! / 3!3!2!2!) = 25200/4^{10}$. Even in this worst case, only three or four continuous 10-mers will need to be read for a unique sequence identification within a genome, and hence positive identification of a specific gene. Therefore, merely finding A, T, G, and C content information for individual DNA

k-mers leads to loss of exact single-letter positions (lossy data compression), but the DNA sequence can still be uniquely identified and converted to useful information.

As an example, a partial (first 100 nucleotide) sequence of the TEM-1 β-lactamase gene from *Escherichia coli* (*E. coli*) is broken down into 10-mer blocks in **Table 1**. The table shows the nucleotide content of each 10-mer and the cumulative expected number of random matches in the *E. coli* genome of 4.6×106 base pairs. For BOS analysis reading sequential k-mer blocks, a unique sequence is reached at the fourth k-mer, meaning that this gene could be identified in four measurements. We further demonstrate that non-sequential, randomized block k-mer identifications can still lead to high-throughput gene identification.

Table 1. 10-mer sequential blocks for a partial sequence of TEM-1 *β*-lactamase gene in *E. coli*.

k-mer number	Sequence	A/T/G/C content	Cumulative number of random matches
1	ATGAGTATTC	3/4/2/1	5.5×10^4
2	AACATTTCCG	3/3/1/3	8.9×10^2
3	TGTCGCCCTT	0/4/2/4	2.7×10^0
4	ATTCCCTTTT	1/6/0/3	2.1×10^{-3}
5	TTGCGGCATT	1/4/3/2	2.6×10^{-5}
6	TTGCCTTCCT	0/5/1/4	3.1×10^{-8}
7	GTTTTTGCTC	0/6/2/2	3.7×10^{-11}
8	ACCCAGAAAC	5/0/1/4	4.4×10^{-14}
9	GCTGGTGAAA	3/2/4/1	5.3×10^{-16}
10	GTAAAAGATG	5/2/3/0	1.3×10^{-18}

Table 2 shows the same partial sequence of the TEM-1 β-lactamase gene, this time with randomized order of the 10-mer blocks. As calculated in the table, a unique sequence is reached again after merely four measurements (with other randomized orders, the maximum number of

necessary reads is five). Therefore, BOS is a different method of sequence and gene identification that offers simultaneous lossy data compression. This high throughput optical detection and data compression can help increase the throughput and speed of DNA sequencing and be a valuable assay for quickly extracting useful genomic information.

Table 2. 10-mer randomized blocks for a partial sequence of TEM-1 β-lactamase gene in *E. coli*.

k-mer number	Sequence	A/T/G/C content	Cumulative number of random matches
2	AACATTTCCG	3/3/1/3	7.4×10^4
10	GTAAAAGATG	5/2/3/0	8.0×10^3
6	TTGCCTTCCT	0/5/1/4	2.6×10^1
8	ACCCAGAAAC	5/0/1/4	5.4×10^{-2}
9	GCTGGTGAAA	3/2/4/1	7.7×10^{-4}
1	ATGAGTATTC	3/4/2/1	7.8×10^{-6}
5	TTGCGGCATT	1/4/3/2	5.3×10^{-8}
3	TGTCGCCCTT	0/4/2/4	6.0×10^{-11}
4	ATTCCCTTTT	1/6/0/3	1.1×10^{-14}
7	GTTTTTGCTC	0/6/2/2	1.3×10^{-18}

We present a new and unconventional approach for high throughput, BOS of DNA in a process that is enzyme- and label-free. BOS uses multiplexed nanoscale pyramid patterns as a probe and incorporates simultaneous lossy data compression by measuring the A, T, G, and C content in DNA k-mer blocks, instead of traditional single-letter sequences. We acquired surface-enhanced Raman spectroscopy (with coupled FTIR spectroscopy) vibrational fingerprints for DNA nucleobases. The reproducible optical fingerprints and signal enhancement from each nanopyramid tip demonstrates the robustness of this method in circumventing the problem of signal uncertainties in other single-molecule DNA sequencing

approaches. Using fingerprints generated from homologous DNA oligomers, we obtained high accuracy and confidence in identifying the content of mixed DNA k-mer sequences, with our algorithmic approach to base calling. Furthermore, we demonstrated that using information of A, T, G, and C content of sequential DNA blocks can serve as an alternative to single-letter sequencing, while randomized block content can be useful for rapid identification of genes and other biomarkers in a high-throughput manner (≈4–5 reads required). This method can be a promising tool in developing more rigorous quantitative technologies that achieve single-nucleotide sensitivity in optical DNA sequence-based assays. While most biomarker discovery techniques today rely on amplification and other biochemical treatments, our results pave the way for high-throughput optical tools for single molecule studies with important biotechnology applications. BOS gene identification methods could be directly applied to rapid genotyping in molecular and evolutionary biology, metagenomics, medical diagnostics, and DNA profiling.

Experimental Section

Preparation of Multiplexed Optical Reader: Plasmonic nanopyramid arrays were fabricated as multiplexed optical probes using optical lithography, self-limited anisotropic chemical etching with potassium hydroxide, and metal deposition followed by template stripping. [22–24].Briefly, circular patterns with 2 μm periodicity were designed using optical lithography and were patterned on a silicon (100) substrate using a metal mask. With self-limiting anisotropic KOH etching, inverted sharp nanopyramids were etched in silicon and

used as a template. Using thermal metal evaporation, a 200 nm thick layer of silver was evaporated onto cleaned templates and peeled off using an epoxy backing layer.

Sample Preparation: Single-stranded DNA oligomers (e.g., poly(dA)$_{16}$, poly(dC)$_{16}$, poly(dG)$_{16}$, poly(dT)$_{16}$, poly(dATGC)$_4$, poly(dAC)$_8$, poly(dGC)$_8$, poly(dCT)$_8$, and poly(dAGC)$_5$) were purchased from Invitrogen, USA, suspended in ultrapure deionized (DI) water obtained from a Barnstead Thermolyne NANOpure Diamond purification system equipped with a UV lamp–water resistivity >18 MΩ cm (10×10^{-9} to 100×10^{-9} m, measured using a nanodrop spectrophotometer), and drop casted onto the multiplexed readers. For contamination studies, dATP and glycine were mixed at varying molar ratios (0×10^{-3} to 5×10^{-3} m) in DI water and drop-casted onto a flat glass substrate. Samples were left to dry in air prior to analysis. See Figure S6 of the Supporting Information for DNA surface density discussion. [39]

Multiplexed Imaging and Optical Vibrational Spectroscopy (Raman and FTIR): The Raman spectra of DNA, benzenethiol, and nucleotide glycine mixtures were acquired using a home-built confocal setup. The samples were imaged using an inverted Zeiss microscope with a 100× objective (NA of 0.85), and the light was focused on the entrance port of a triple grating Princeton Instrument imaging spectrophotometer (Acton SpectraPro SP-2500 equipped with a PIX100B-SF camera). An He-Ne laser was used as the excitation source at λ_{Exc} = 632.8 nm, and the Rayleigh scattering was filtered using a notch Raman filter. For samples on multiplexed nanopyramid substrates, individual pyramids containing molecules were focused and the image was formed in the Princeton imaging spectrophotometer. Using the tip image with the respective spectra, the Raman spectra from

each tip were mapped. The FTIR spectra were acquired using a Nicolet 6700 IR spectrometer with a spectral resolution of 1 cm^{-1}. The spectrometer was modified to incorporate imaging of the nanopyramids using an IR aspherical lens with antireflection coating for 8–12 µm (C028TME-F – f = 5.95 mm, NA = 0.56, Thorlabs).

Base Calling Algorithms for Optical Sequencing: Identifying unknown k-mer blocks from Raman (and coupled FTIR) spectra requires comparing measurements on unknown k-mers to established fingerprints for known nucleobases. For the optical vibrational spectroscopic methods here, identifications are made via comparing characteristic fingerprint peaks, by calculating the area under the spectral curves. To establish fingerprints, OriginPro 2016 was used for fitting Gaussian curves to block k-mer spectra from homologous sequences (via the Fit Peaks functionality within the Peak Analyzer toolkit). From the Gaussians, the center location and corresponding FWHM were determined for each characteristic peak in the spectra. Gaussian fitting was performed on five Raman spectra and one FTIR spectrum from homologous oligomers of each nucleobase (A, T, G, and C). The average peak center locations and FWHM from these spectra provided the fingerprints used for base calling. The base calling analysis was implemented in MATLAB. The algorithm which is derived for characterizing unknown spectra operates by quantifying area under the curve within the FWHM region of known peak locations, or the fingerprints, for nucleobases A, T, G, and C. For identifying which nucleobases are present in a specific k-mer, a subset of spectra peaks for each nucleobase were considered (the peaks most unique for each nucleobase or those most often appearing together, as seen in Figure 3a). Base calls are made for whichever nucleobases show the largest intensity (largest integrated area) in the unknown spectra. For homologous sequences, this can be quantified into a probability value for nucleobase i: $P_{i} = (\sum_{j=1}^{n} A_{i,j} / F_{i,j})/n$. In this expression, n

is the number of peaks used as fingerprints for identification, $A_{i,j}$ is the area under the curve within the FWHM region of peak j for nucleobase i, and $F_{i,j}$ is the FWHM of peak j for nucleobase i. Pi values are normalized to the sum of probabilities for each nucleobase ($P_A + P_T + P_G + P_C$), and a single nucleobase can be called. For mixed sequences, this probability value is not used. Nucleobases are called if significant intensity is seen for characteristic fingerprint peaks, and their relative fraction is determined from correlations comparing measured intensity to known fractions (as seen in Figure 3b,c).

Supplementary Figures and Tables
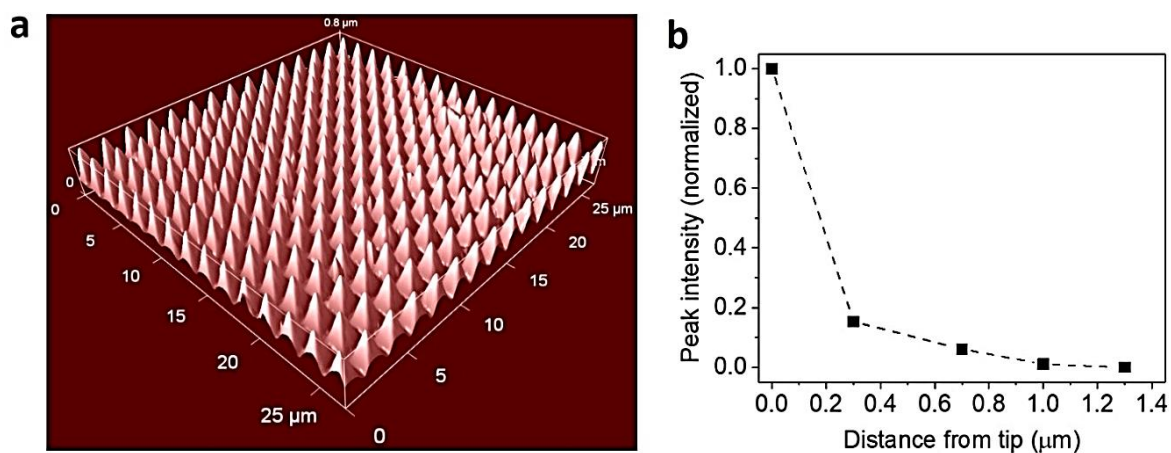
Figure S1. Multiplexed nanopyramid optical substrate and signal enhancement. (a) AFM (atomic force microscopy) image of the multiplexed optical reader with the designed nanopyramid substrate. (b) Multiphoton confocal cross-sectional variation of amplitude of the Raman spectra for nanopyramids (signal from adenine) vs. distance from the apex of the tip. More than one million tips were present in each multiplexed optical reader used in the study
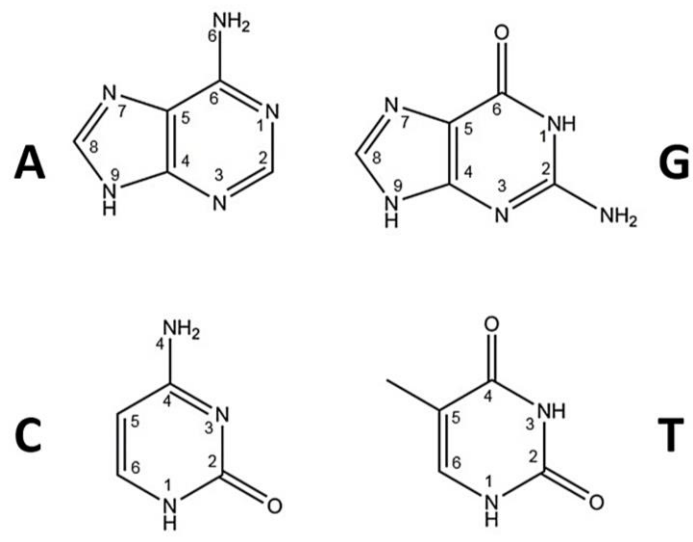
Figure S2. Biochemical structure of DNA nucleobases A, T, G, and C (including the numbering scheme for molecular bonds). [1–5]

Table S1. Raman spectroscopy peaks[1–4,6]

Peak	Shift (cm^{-1})	Assignment
A_1	340	Hydrogen bonding
A_2	537	C-C=C bend
A_3	622	N-C-C bend
A_4	737	C-C and C-N in-phase stretch
A_5	971	N-C=N bend
A_6	1045	C-N-C bend
A_7	1140	C2-N1=C6 bend C5-N7=C8 stretch
A_8	1320	C-N stretch
A_9	1350	C=N stretch
a_1	841	skeletal mode, in-plane
a_2	1167	CH bend, in-plane
T_1	304	OH···O bend
T_2	467	N-C=C bend
T_3	647	N-C-C bend
T_4	737	C5-CH$_3$ stretch
T_5	832	C4-C5 stretch
T_6	1017	C-N-C bend
T_7	1059	N-C-H bend
t_1	589	C-C=C bend
t_2	953	C5-C-H bend
C_1	395	N3-C2=O and N1-C2=O bend
C_2	468	C2-N1-C6 and N3=C4-C5 bend
C_4	538	C-C=C and N3=C4-N4 bend
C_5	558	C2-N3=C4 and N1-C2-N3 bend
C_6	611	C=O in-phase stretch
C_8	788	Breathing mode
C_{10}	973	C4-C5 stretch

c_2	715	C5-C4-N4 bend
c_3	1000	C4-C5-H in-plane bend
c_4	1028	N1-C6-H in-plane bend
G_1	402	C=O bend
G_2	511	N9-C4=C5 and N7-C=C4 bend
G_3	604	C=C=C bend
G_4	648	Breathing mode
G_6	847	C-C stretch
G_7	931	N-C=N and N-C-N bend
G_{11}	1226	C_2-NH_2 stretch
g_1	548	N3-C4=C5 bend
g_3	866	N9-H out-of-plane bend

Table S2. FTIR spectroscopy peaks[1–5]

Peak	Wavenumber (cm^{-1})	Assignment
α_2	727	C-C and C-N in-phase bend
α_3	807	C-C stretch
α_4	869	N9-H out-of-plane bend
α_5	952	N-C=N bend
α_7	1129	C2-N1=C6 bend C5-N7=C8 stretch
α_9	1371	C2-H and C8-H out-of-plane bend N=C-H bend
α_{10}	1460	Imidazole ring stretch
α_{11}	1507	C-N9-H bend
α_{12}	1620	C=N and C=C stretch
α_{13}	1650	NH$_2$ bend
τ_2	861	N-H out-of-plane bend
τ_7	1227	C-N stretch
τ_9	1511	N1-H and N3-H bend
τ_{12}	1750	C4=O and C2=O stretch
χ_1	813	N-H out-of-plane bend
χ_3	1077	NH$_2$ rocking
χ_4	1235	C4-N4 stretch
χ_5	1361	C=C-H bend
χ_6	1458	C4-N3 and C2-N3 stretch
χ_7	1519	C4=N3 and C4-N4 stretch
χ_8	1626	C5=C6 stretch
χ_9	1708	NH$_2$ bend
γ_2	712	Ring bend
γ_3	804	N1-H bend
γ_4	860	C-C stretch
γ_6	1056	NH$_2$ rocking

γ_{10}	1493	N7=C8 and C8-C9 stretch
γ_{12}	1660	C=O stretch
γ_{13}	1698	C=O stretch NH$_2$ bend
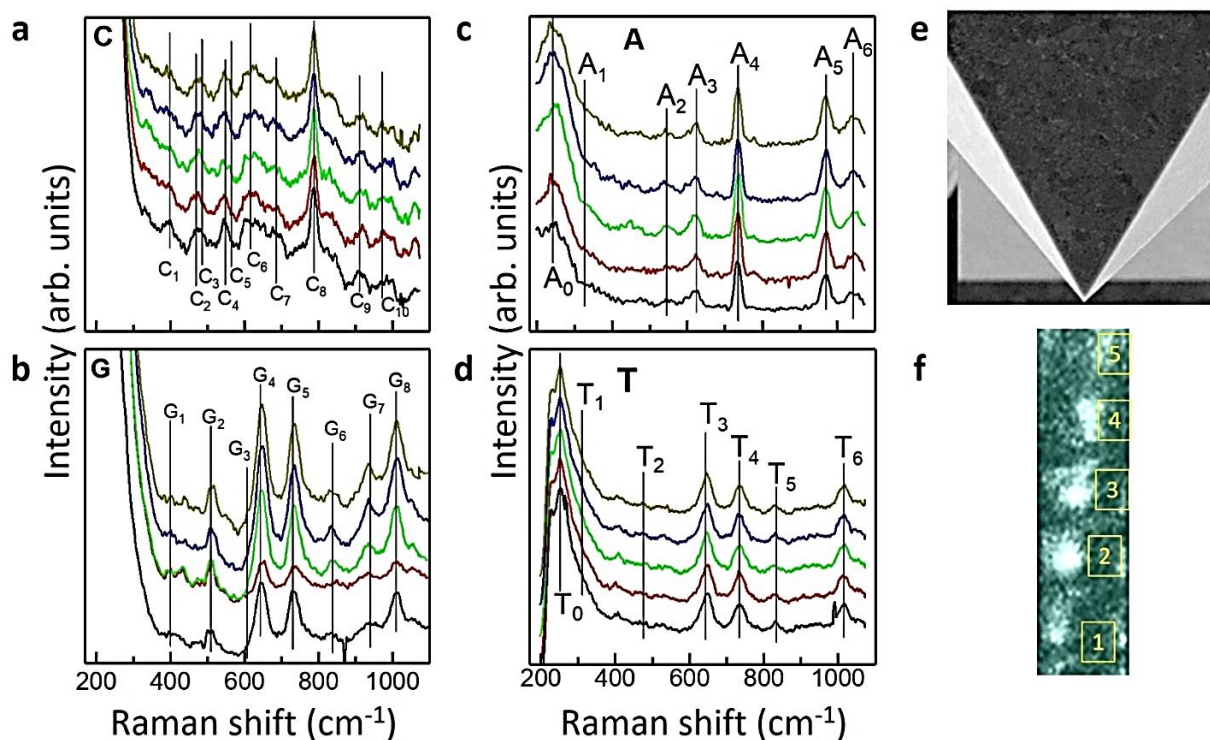
Figure S3. Reproducibility of optical fingerprints for DNA k-mers. Raman spectra of homologous DNA oligomers of (a) cytosine, (b) guanine, (c) adenine, and (d) thymine showing the reproducibility of the spectra for five randomly selected nanopyramid tips. (e) Scanning electron micrograph of a nanopyramid tip. (f) Top view of nanopyramid tips as seen in the Raman imaging spectrometer, the individual tips are marked.
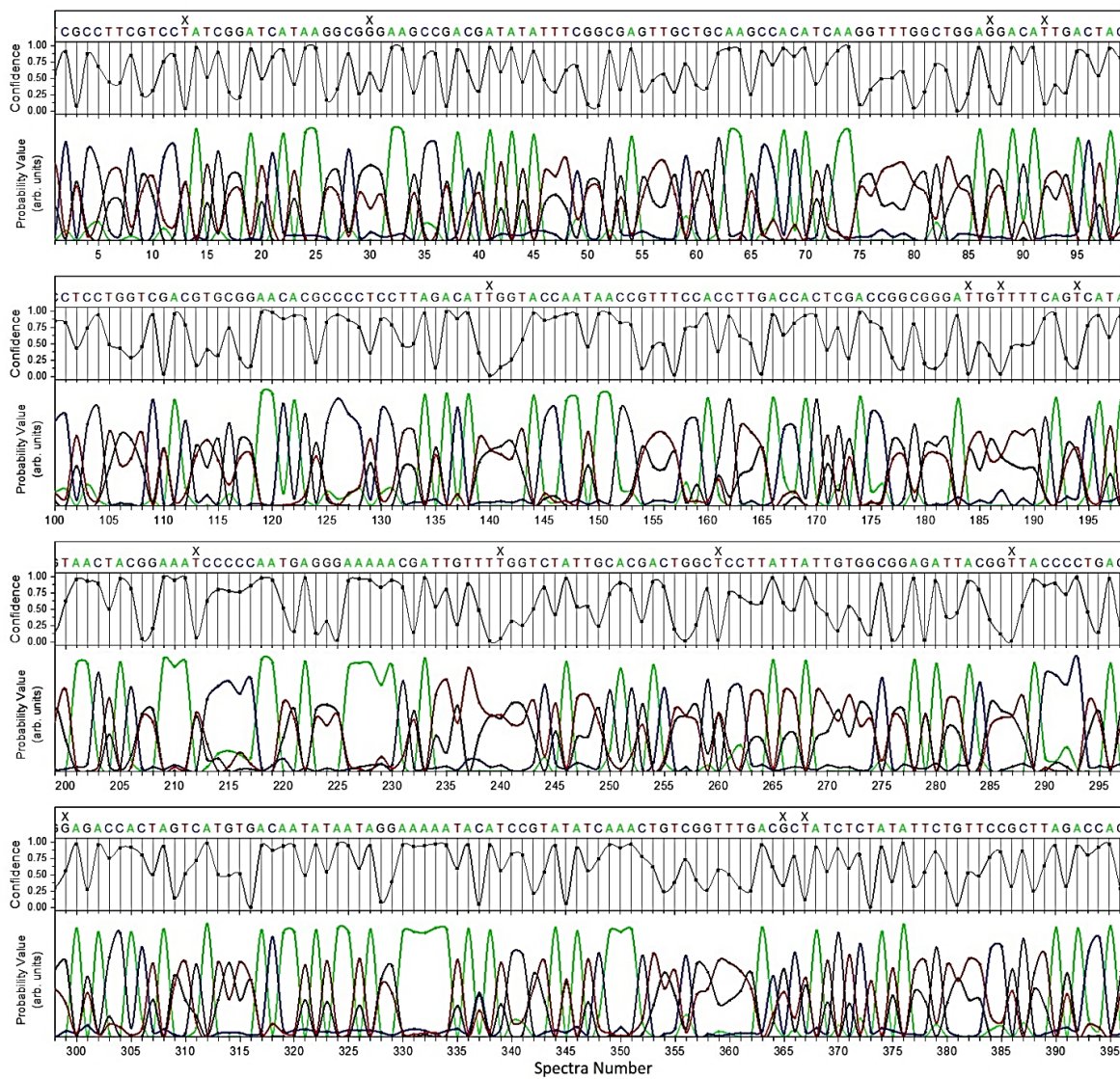
Figure S4. Probability values and confidence for base calling homologous k-mer blocks with Raman spectroscopy. Numbers correlate with those in Fig. S5
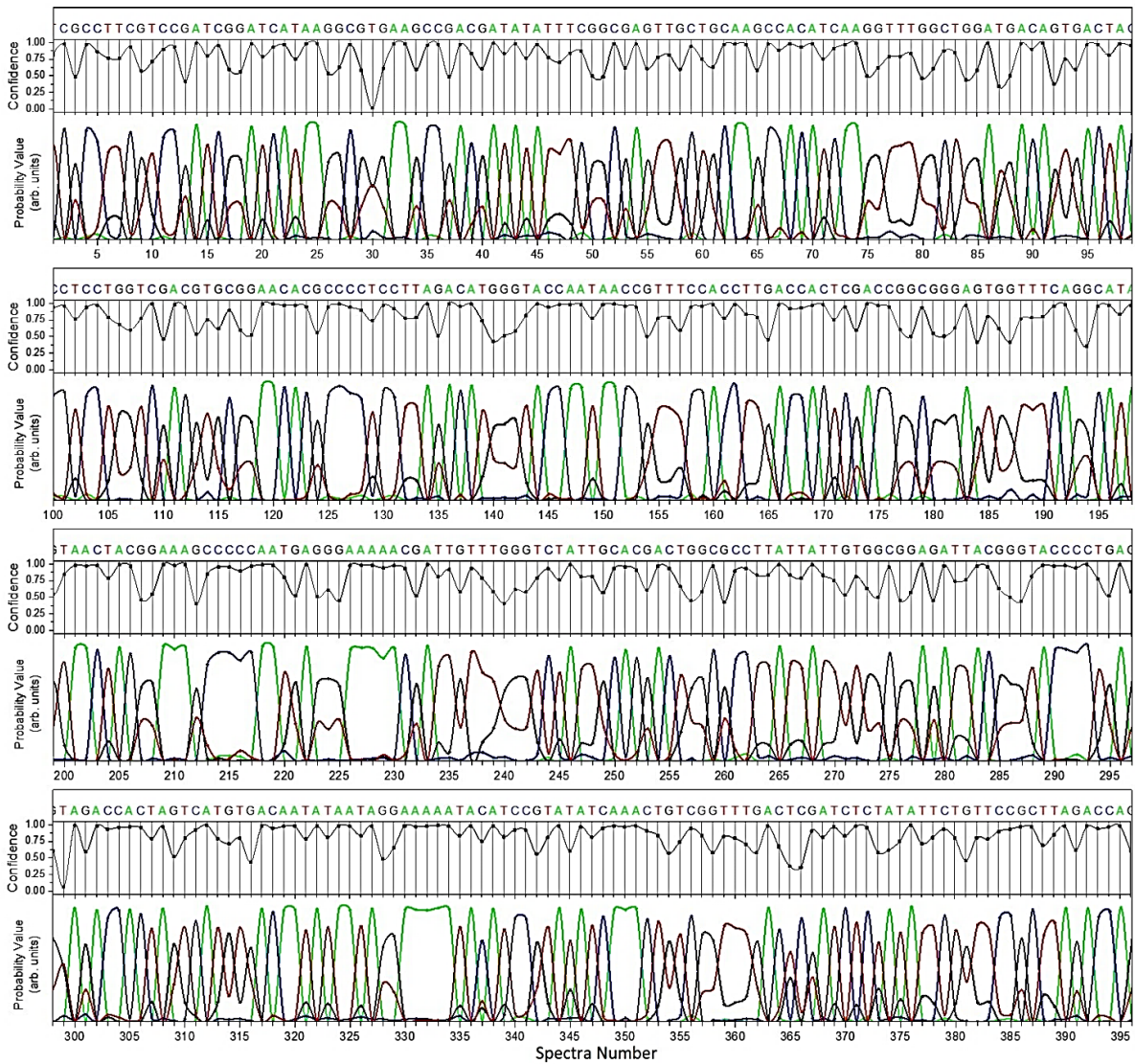
Figure S5. Probability values and confidence for base calling homologous k-mer blocks with combined Raman and FTIR. Numbers correlate with those in Fig. S4.
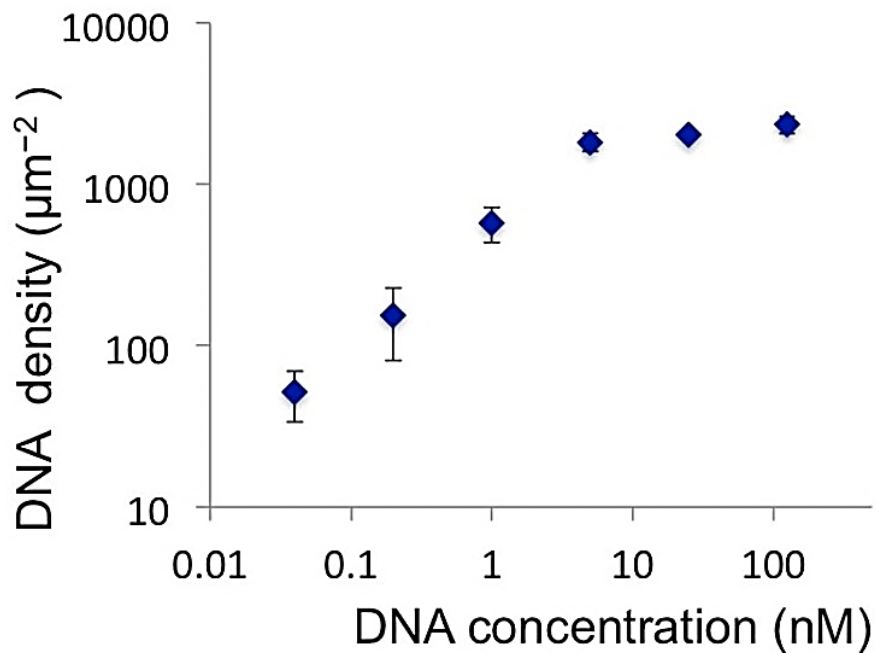
Figure S6. DNA surface density vs. concentration. Concentration series of apparent DNA surface density as a function of DNA concentration for a fixed time of t=5 min onto a cysteamine surface substrate. Each point represents the mean surface density determined by averaging the number of molecules per area in several images corresponding to different areas of the surface (AFM imaging and semi-automated image analysis with Gwyddion). The error bars represent +/- the standard deviation between different areas of the surface in the same experiment

References: -

1. D. Branton, D. W. Deamer, A. Marziali, H. Bayley, S. A. Benner, T. Butler, M. Di Ventra, S. Garaj, A. Hibbs, X. Huang, S. B. Jovanovich, P. S. Krstic, S. Lindsay, X. S. Ling, C. H. Mastrangelo, A. Meller, J. S. Oliver, Y. V Pershin, J. M. Ramsey, R. Riehn, G. V Soni, V. Tabard-Cossa, M. Wanunu, M. Wiggin, J. A. Schloss, *Nat. Biotechnol.* **2008**, *26*, 1146.

2. E. A. Pozzi, M. D. Sonntag, N. Jiang, J. M. Klingsporn,M. C. Hersam, R. P. Van Duyne, *ACSNano***2013**,*7*,885.

3. E. L. Van Dijk, H. Auger, Y. Jaszczyszyn, C. Thermes, *Trends Genet.* **2014**, *30*, 418.

4. S. Goodwin, J. D. McPherson, W. R. McCombie, *Nat. Rev. Genet.* **2016**, *17*, 333.

5. R. A. Copeland, M. P. Moyer, V. M. Richon, *Oncogene* **2013**, *32*, 939.

6. P. Jares, D. Colomer, E. Campo, *Nat. Rev. Cancer* **2007**, *7*, 750.

7. S. K. Gire, A. Goba, K. G. Andersen, R. S. G. Sealfon, D. J. Park, L. Kanneh, S. Jalloh, M. Momoh, M. Fullah, G. Dudas, S. Wohl, L. M. Moses, N. L. Yozwiak, S. Winnicki, C. B. Matranga, C. M. Malboeuf, J. Qu, A. D. Gladden, S. F. Schaffner, X. Yang, P.-P. Jiang, M. Nekoui, A. Colubri, M. R. Coomber, M. Fonnie,A. Moigboi, M. Gbakie, F. K. Kamara, V. Tucker, E. Konuwa, S. Saffa, J. Sellu, A. A. Jalloh, A. Kovoma, J. Koninga, I. Mustapha, K. Kargbo, M. Foday, M. Yillah, F. Kanneh, W. Robert, J. L. B. Massally, S. B. Chapman, J. Bochicchio, C. Murphy, C. Nusbaum, S. Young, B. W. Birren, D. S. Grant, J. S. Scheiffelin, E. S. Lander, C. Happi, S. M. Gevao, A. Gnirke, A. Rambaut, R. F. Garry, S. H. Khan, P. C. Sabeti, *Science* **2014**, *345*,1369.

8. P. W. Laird, *Nat. Rev. Cancer* **2003**, *3*, 253.

9. J. Deng, R. Shoemaker, B. Xie, A. Gore, E. M. LeProust, J. Antosiewicz-Bourget, D. Egli, N. Maherali, I.-H. Park, J. Yu, G. Q. Daley, K. Eggan, K. Hochedlinger, J. Thomson, W.Wang,Y.Gao,K.Zhang,*Nat.Biotechnol.***2009**,*27*,353.

10. E.Bailo,V.Deckert, *Angew. Chem., Int. Ed.* **2008**, *47*, 1658.

11. Barhoumi, D. Zhang, F. Tam, N. J. Halas, *J. Am.* **2008**, *130*, 5523.

12. L. Guerrini, Ž. Krpetić, D. Van Lierop, R. A. Alvarez-Puebla, D. Graham, *Angew. Chem., Int.Ed.***2015**,*127*,1160.

13. L. Xu, Z. Lei, J. Li, C. Zong, C. J. Yang, B. Ren, *J. Am. Chem. Soc.* **2015**, *137*, 5149.

14. J. Morla-Folch, H. N. Xie, P. Gisbert-Quilis, S. G. De Pedro, N. Pazos-Perez, R. A. Alvarez Puebla, L. Guerrini, *Angew. Chem., Int. Ed.* **2015**, *127*, 13854.

15. S. Lal, N. K. Grady, J. Kundu, C. S. Levin, J. B. Lassiter, N. J. Halas, *Chem. Soc. Rev.* **2008**,*37*,898.

16. K. Kneipp, Y. Wang, H. Kneipp, L. T. Perelman, I. Itzkan, R. R. Dasari, M. S. Feld, *Phys. Rev.Lett.***1997**,*78*,1667.

17. E. J. Blackie, E. C. Le Ru, P. G. Etchegoin, *J. Am. Chem. Soc.* **2009**, *131*, 14466.

18. K. Nakamoto, *Handbook of Vibrational Spectroscopy*, John Wiley & Sons, Inc., Hoboken, NewJersey**2006**.

19. D. Zhang, K. F. Domke, B. Pettinger, *ChemPhysChem* **2010**, *11*, 1662.

20. R. Treffer, R. Böhme, T. Deckert-Gaudig, K. Lau, S. Tiede, X. Lin, V. Deckert, *Biochem. Soc.Trans.***2012**,*40*,609.

21. S. Najjar, D. Talaga, L. Schue, Y. Coffnier, S. Szunerits, R. Boukherroub, L. Servant, V. Rodriguez,S.Bonhommeau,*J.Phys.Chem.C***2014**,*118*,1174.

22. N. C. Lindquist, P. Nagpal, A. Lesuffleur, D. J. Norris, S. H. Oh, *Nano Lett.* **2010**, *10*, 1369.

23. P. Nagpal, N. C. Lindquist, S.-H. Oh, D. J. Norris, *Science* **2009**, *325*, 594.

24. N. C. Lindquist, P. Nagpal, K. M. McPeak, D. J. Norris, S.-H. Oh, *Rep. Prog. Phys.* **2012**, *75*,36501.

25. C. Ropers, C. C. Neacsu, T. Elsaesser, M. Albrecht, M. B. Raschke,C. Lienau, *Nano Lett.* **2007**,*7*,2784.

26. Bouhelier, M. Beversluis, A. Hartschuh, L. Novotny, *Phys. Rev. Lett.* **2003**, *90*, 13903.

27. Q. C. Sun, H. Mundoor, J. C. Ribot, V. Singh, I. I. Smalyukh, P. Nagpal, *Nano Lett.* **2013**, *14*,101.

28. N. A. Janunts, K. S. Baghdasaryan, K. V. Nerkararyan, B. Hecht, *Opt. Commun.* **2005**, *253*,118.

29. M. Mathlouthi, A.-M. Seuvre, J. L. Koenig, *Carbohydr. Res.* **1984**, *131*, 1.

30. C. Otto, T. van den Tweel, F. de Mul, J. Greve, *J. Raman Spectrosc.* **1986**, *17*, 289.

31. J. De Gelder, K. De Gussem, P. Vandenabeele, L. Moens, *J. Raman Spectrosc.* **2007**, *38*, 1133.

32. R. Treffer, X. Lin, E. Bailo, T. Deckert-Gaudig, V. Deckert, *Beilstein J. Nanotechnol.* **2011**,*2*,628.

33. M. Mathlouthi, A.-M. Seuvre, J. L. Koenig, *Carbohydr. Res.* **1984**, *134*, 23.

34. M. Mathlouthi, A.-M. Seuvre, J. L. Koenig, *Carbohydr. Res.* **1986**, *146*, 1.

35. M. Mathlouthi, A.-M. Seuvre, J. L. Koenig, *Carbohydr. Res.* **1984**, *146*, 15.

36. A.-M. Seuvre, M. Mathlouthi, *Carbohydr. Res.* **1987**, *169*, 83.

37. Barhoumi, N. J. Halas, *J. Phys. Chem. Lett.* **2011**, *2*, 3118.

38. F. Pashaee, M. Tabatabaei, F. A. Caetano, S. S. G. Ferguson, F. Lagugné-Labarthet, *Analyst***2016**,*141*,3251.

39. S. Afsari, L. E. Korshoj, G. R. Abel Jr., S. Khan, A. Chatterjee, P. Nagpal, *ACS Nano* **2017**, *11*, 11169.

Chapter 2

Determination of efficiencies of various reactive oxygen species as a therapeutic agent against multidrug resistant bacteria

Reproduced with permission from Max Levy, Colleen M. Courtney, Partha P. Chowdhury, Yuchen Ding, Emerson L. Grey, Samuel M. Goodman, Anushree Chatterjee and Prashant Nagpal. Assessing Different Reactive Oxygen Species as Potential Antibiotics: Selectivity of Intracellular Superoxide Generation Using Quantum Dots. *ACS Appl. Bio Mater*. 2018, 1, 529-537. Copyright 2018, American Chemical Soceity

Introduction

Reactive oxygen species (ROS) and reactive nitrogen species (RNS) are a broad class of oxygen- and nitrogen-centered species widely responsible for physiology and pathology in living organisms. [1,2] Due to their omnipresence and relative ease of formation in the cellular environment, researchers have investigated their potential for therapeutic applications. While some species are regulatory and believed to be used for molecular signaling and as activators for stress response,[3-7] others can cause indiscriminate oxidative damage and dysfunction.[8-13] Further, several chemical reactions like Fenton chemistry,[14] disproportionation,[15] and enzymatic conversion can result in the formation of other radicals, such as the conversion of superoxide into hydrogen peroxide, hydroxyl radicals, and peroxynitrite ions.[14,16,17] Therefore, mechanistic insights into desired biological targets and precise control over intracellular generation of specific ROS and RNS can play a key role in

the specificity of a designed therapeutic as well as its mechanism of action. Several approaches have been used to develop effective nanoscale therapeutics. The use of light-activated gold and silver nanoparticles enables spatial and temporal control over cell death, along with stability and ease of delivery, but lacks specificity due to the photothermal mechanism of action.[18,19] Photodynamic therapy (PDT) utilizes the concept of light activation with small photosensitizing molecules to address the issue of specific drug release.[20,21] However, PDT lacks tunability or precise control over the ROS generated, such as singlet oxygen.[22,23] As an oxidant, singlet oxygen is very reactive and leads to nonspecific oxidative stress in the surrounding environment.[24] Only with the conjugation of biomolecules or localized illumination can singlet oxygen spare healthy tissue.[25] This limits its appeal as a precision medicine approach to treat a variety of diseases.[26,27] Recently, quantum dots (QDs), or semiconductor nanocrystals, have been proposed as a size-, shape-, and composition-tunable material for these biological applications.[28] Precise control over their photogenerated electron and hole states provides desired electronic properties and photochemistry in the cellular environment. Further research into tuning surface charges has demonstrated the ease of intracellular delivery, transport, and subsequent clearance from the body. [29] Conjugating QDs with a range of biomolecules like DNA and peptides can also provide a strong affinity toward specific biological targets in vivo. [30,31]

Toward the rational design of an effective antimicrobial against MDR pathogens, we first assessed different ROS and their effects on a model E. coli strain (MG1655). Using electron paramagnetic resonance (EPR) spectroscopy and spin trapping, [32,33] we identified the oxidative species present. In this scheme, any short-lived radical species generated would be trapped as a more stable radical adduct for detection. We used this technique to identify and

quantify radical species and examine the effect of specific radical scavengers to further investigate the mechanism of action. Based on the identified ROS with a therapeutic effect, we designed QDs to specifically generate the desired species intracellularly using an external stimulus (light here), to determine the efficacy of such therapeutic in a cellular environment. Then we screened these QDs as a potential therapeutic in a wide range of MDR clinical isolates, to further validate the robustness of the proposed therapy.

Results and Discussions

Assessment of Different Reactive Oxygen Species. To assess the potential for different ROS as effective antimicrobials, we first generated exogenous ROS and evaluated their respective effects on *E. coli*. We used the direct treatment with hydrogen peroxide to evaluate the role of peroxide; the reaction of hydrogen peroxide and sodium hypochlorite to form singlet oxygen; the reaction of hydrogen peroxide and iron sulfate to form hydroxyl radicals; and light activated 3 nm cadmium telluride QDs with a 2.4 eV band gap (CdTe-2.4) to generate superoxide. The superoxide generation was done intracellularly due to the lack of superoxide transport through a cellular membrane. Using the spin trap 5,5-dimethyl-1-pyrroline N-oxide (DMPO), [34] we measured the EPR (electron paramagnetic resonance) spectra for the mixture of hydrogen peroxide and iron sulfate and confirmed the generation of hydroxyl radicals (Figure 1a). A quartet of peaks associated with the hydroxyl radical adduct of DMPO (DMPO-OH) matched with the appropriate hyperfine coupling constants ($a_N = 14.90$ G, $a_H^\beta = 14.93$ G). Similarly, we confirmed singlet oxygen generation using a singlet oxygen trap: 2,2,6,6-tetramethylpiperidine (TMP; $a_N = 15.04$ G; Figure 1c). For spectroscopic verification of superoxide radical generation, we used a suspension of CdTe-2.4. Initially, the

quantum dot suspension was completely sequestered from light to obtain a baseline EPR

spectrum (see the Experimental Section for sample handling instructions). As expected, this

dark spectrum showed no characteristic peaks aside from the E′ defect associated with the

quartz capillaries used (Figure S1). The same sample was then illuminated with visible light for

45 s and returned to the EPR cavity for measurement. The resulting spectra showed a strong set

of peaks, including those characteristics of the superoxide adduct (DMPO-OOH), indicating

direct superoxide generation (Figure 1e). These observed peaks fit well with the theoretical

hyperfine coupling constants (a^N = 14.2 G, a_H^β = 11.4 G, $aHϒ1$ = 1.2 G). Following

spectroscopic verification, we evaluated the effect of respective ROS with varying

concentrations on *E. coli* MG1655 (Figure 1b,d,f,g).
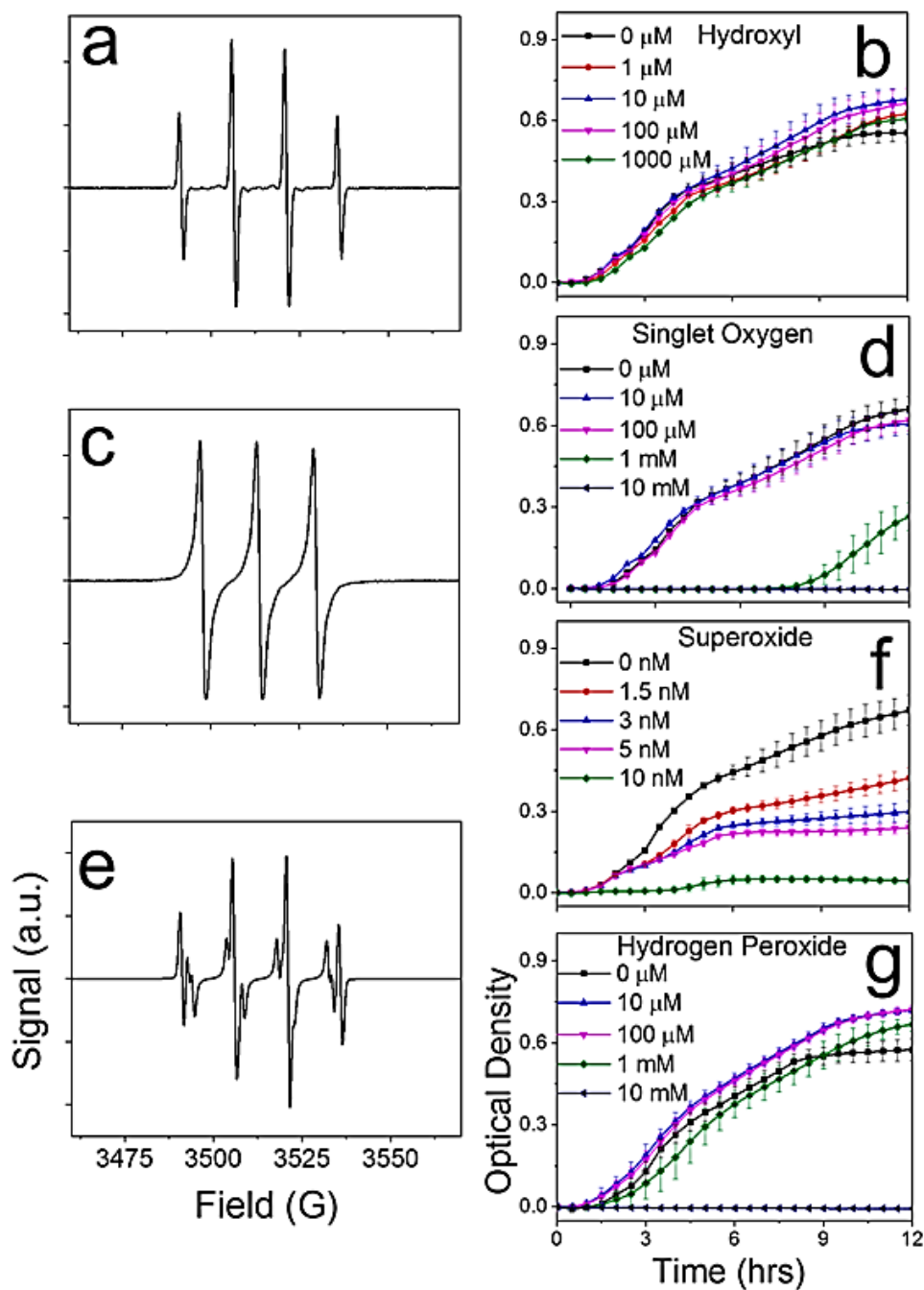
Figure 1. Therapeutic assessment of different types of ROS. (a) EPR spectra of the hydroxyl radical source (H$_2$O$_2$ and FeSO$_4$). (b) Growth curves for treatment with different doses of the hydroxyl radical source. No toxicity is seen through 1 mM. (c) EPR spectra of the singlet oxygen source (H$_2$O$_2$ and NaOCl + TMP). (d) Growth curves for treatment with different doses of a singlet oxygen source. No toxicity is apparent below 10 mM singlet oxygen. (e) EPR

spectra of superoxide radical (from illuminated CdTe-2.4). (f) Growth curves for treatment with different doses of superoxide. Toxicity apparent at nanomolar doses. (g) Growth curves for treatment with different doses of hydrogen peroxide. No toxicity is apparent before 10 mM hydrogen peroxide. All growth curves represent *E. coli* MG1655 growth.

We observed that the superoxide anion caused significant growth inhibition of E. coli at very low steady-state concentrations (1.5 nM, Figure 1f) and that inhibition increased gradually with an increasing superoxide concentration. In contrast, the other ROS caused no attenuation in the growth of E. coli until reaching high threshold concentrations (singlet oxygen, 1 mM; peroxide, 10 mM; hydroxyl radical, >10 mM), consistent with other reports from the field. [35] Similarly, evaluation of nitric oxide as a potential RNS treatment also yielded minimal therapeutic effect (Figure S2). At this dose, these ROS have been shown to be toxic even for host mammalian cells. [36-38] Between the different ROS and RNS studied here, only superoxide shows an antimicrobial effect at concentrations below the nominal threshold of potential host cell toxicity.

Specific Generation of Superoxide. Using light activated CdTe-2.4 QDs, superoxide detection was found to intensify with an increasing QD concentration [39] and illumination time (Figure 2a). The experiment was repeated using TMP as a spin trap for singlet oxygen. The resulting EPR spectra yielded a negligible signal, indicating no detectable formation of a singlet oxygen (Figure S3). This showed that light activation of CdTe-2.4 leads to the specific generation of superoxide and possibly hydroxyl radicals. Given the band gap of CdTe-2.4 and the position of its conduction band (Figure 2b), detection of superoxide upon visible light illumination was expected. However, as time passed after illumination, successive scans revealed that the DMPO-OOH signal decreased while that of DMPO-OH increased

(Figure 2c) until all that remained was the quartet of DMPO-OH peaks. Direct conversion of DMPO-OOH to DMPO-OH was considered highly unlikely.[40] While the mechanism for intracellular conversion of O2•- to OH• is well documented,[16] we probed other potential sources of OH•, including direct formation by hole injection from the QDs, by using cyclic voltammetry techniques in phosphate buffered saline solution (PBS).[15,41] We observed the formation of superoxide in the cathodic trace (peak around -0.33 V vs NHE (normal hydrogen electrode)) due to direct electron injection to the dissolved oxygen and also a small peak in the anodic trace (around +0.5 V vs NHE) for hydroxyl radicals (Figure 2d).
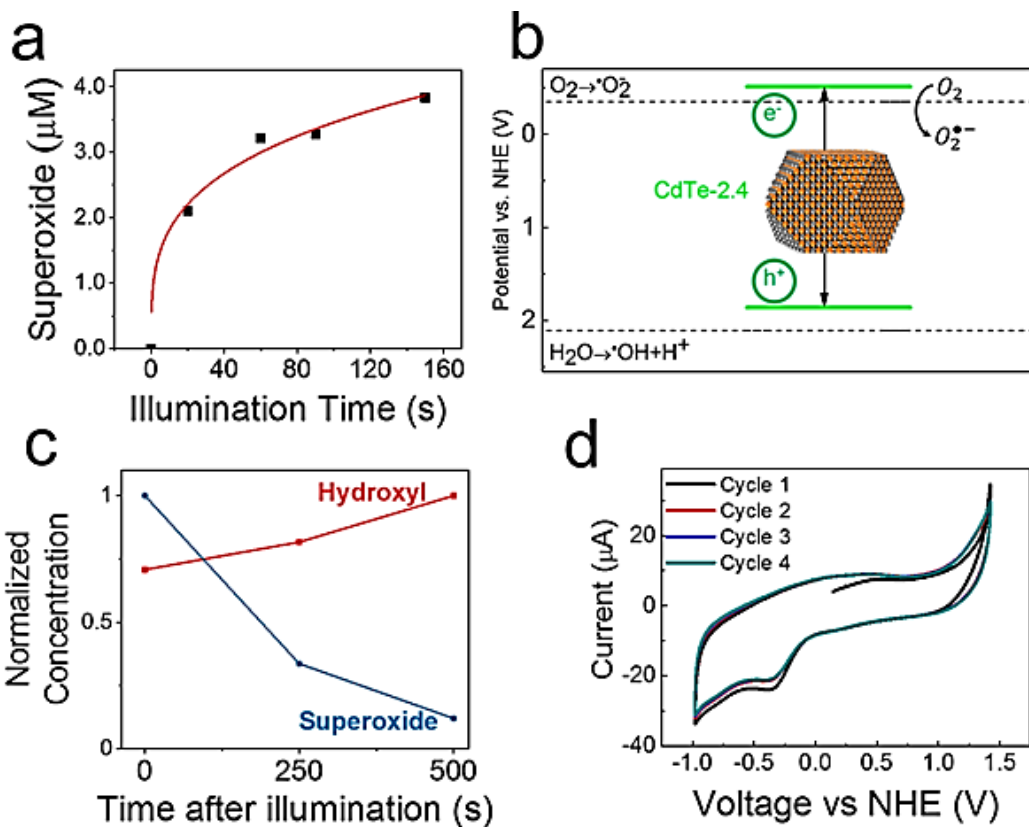
Figure 2. Specific photogenerated superoxide from CdTe-2.4 quantum dots. (a) Observed signal (fitted using Bruker SpinFit) intensification with illumination time. (b) Conduction-valence band positions (vs NHE) of CdTe quantum dots with a 2.4 eV band gap compared to redox potentials for water oxidation/reduction reactions (dashed lines). Only superoxide

generation should be energetically favorable. (c) Concentrations of hydroxyl and superoxide radicals detected by EPR over time after illumination. Hydroxyl radicals are detected following the superoxide adduct decomposition. (d) Cyclic voltammograms in PBS exhibiting decreased superoxide signal (-0.33 V) with successive scans, due to consumption of dissolved oxygen.

We also performed the same electrochemical characterization in oxygen-free buffer (see the Experimental Section). No dissolved oxygen was available in the water, preventing direct superoxide generation, whereas abundant water was available for oxidation to hydroxyl, and yet, hydroxyl radical peaks were not observed. The lack of both superoxide and hydroxyl peaks (Figure S4) shows that hydroxyl generation depends on oxygen availability (via superoxide generation). This further indicates that the radical is formed indirectly as a product of superoxide's Fenton chemistry. The most likely source of OH• detected by EPR was, therefore, the decomposition of DMPO-OOH ($\tau_{1/2} \approx 66$ s) [42] yielding a free hydroxyl capable of rapid trapping by other DMPO molecules. As further evidence that CdTe-2.4 only generates superoxide, we conducted EPR measurements in the presence of superoxide dismutase (SOD), a known superoxide scavenger ($k = 1 \times 10^9$ M^{-1} s^{-1}). [43] EPR signals in the presence of SOD for both DMPO-OOH and DMPO-OH were significantly attenuated (Figure 3a). This indicates that rapidly quenching the superoxide radical eliminates any likelihood of hydroxyl radical formation, pointing specifically to superoxide formation via direct electron transfer from CdTe-2.4 QDs to dissolved oxygen. The hydroxyl radical is only formed indirectly, and not through the direct oxidation of water through the photogenerated hole from CdTe-2.4. These experimental results support our previous observations that the light-activated CdTe-2.4 therapeutic effect is significantly reduced in anaerobic conditions. [28]

Therapeutic Relevance of Exogenous Superoxide. With concrete evidence for the direct and specific generation of superoxide radicals, additional investigation was needed to elucidate the role of superoxide in cell death observed at a nanomolar QD dosage. Superoxide is suspected to inhibit cell growth through multiple pathways, including reaction with iron-sulfur clusters. [35,44] The high reactivity of OH• and $^1O_2$ translates to more indiscriminately lethal effects than O2•-; [8] superoxide's reaction specificity leads to more consequential targeted cell damage. Based on our therapeutic assessment of different ROS, we suspected that superoxide played the most consequential role in the observed cell death. However, because superoxide can disproportionate to hydroxyl, it was not explicitly clear whether direct hydroxyl generation would have the same effect. To resolve this, we used specific scavengers of $O^{2 \cdot-}$ and OH• to isolate the effect of superoxide in the cell culture.

Ascorbic acid (Asc) has been reported to scavenge superoxide with a second-order rate constant of 3.4×10^5 $M^{-1}s^{-1}$.[45] As a comparison, aside from the SOD enzyme, typical rates for other biomolecules present are much lower, and high selectivity has been asserted when rate constants exceed 10^3 M^{-1} s^{-1}.[46,47] With such a high selectivity, we expected most of the photogenerated superoxide to be scavenged before forming any adducts with DMPO. Like the EPR spectra in the presence of SOD, the resulting spectra from photoexcited CdTe-2.4 suspensions showed negligible adduct formation in the presence of ascorbic acid (Figure 3b). Effective scavenging upon light illumination was observed even at a low ascorbic acid concentration of 10 μM versus 90 mM DMPO in a 2.5 μM QD suspension. To test the role of superoxide in the cell culture, we added varying amounts of superoxide-scavenging ascorbic acid and monitored the therapeutic effect of CdTe-2.4 (25 nM) against E. coli MG1655 in M9

minimal media. We observed a reduction in therapeutic action with doses of 1.1 mM and 5.7 mM ascorbic acid (Figure 3c).

Figure 3. Effect of superoxide scavengers on EPR measurements and bacterial cultures. (a, b) EPR spectra for photoexcitation of CdTe-2.4 alone and in the presence of (a) Superoxide

dismutase (SOD; fitted spectra using SpinFit) and (b) ascorbic acid (Asc). Efficient superoxide-scavenging results in negligible radical detection, confirming that hydroxyl radicals are only formed indirectly. (c) Growth curves for *E. coli* MG1655 in M9 minimal media with 25 nM CdTe- 2.4 and ascorbic acid. Bacteria grown with quantum dots alone display growth inhibition. By cotreating with a superoxide scavenger, the inhibitory effect of CdTe-2.4 (superoxide) is quenched.

In both cases, the decrease in antimicrobial effect of CdTe-2.4 QDs was statistically significant ($p < 0.05$). As the dose of scavenger increased, the effect of CdTe-2.4's photogenerated superoxide was further attenuated. At 5.7 mM ascorbic acid, we observed complete elimination of cell killing from quantum dots, indicating that the therapeutic action may be attributed to superoxide radicals. To verify this hypothesis, we created two E. coli mutant constructs, one with sodB overexpression and one with sodB gene deletion and compared the therapeutic effect to the respective control (Figure S6).[39] Again, we observed a decrease in the therapeutic effect of CdTe-2.4 with increased superoxide-scavenging. These results further correlate superoxide concentration with therapeutic action, suggesting superoxide as the radical responsible for the selective action. To probe the potential therapeutic effect of nonspecific oxidative stress, we assessed the role of hydroxyl radicals and found more evidence to demonstrate the importance of superoxide in selective nano therapy. The amino acid histidine (His) has been shown to react slightly faster with hydroxyl (1.3×10^{10} $M^{-1}s^{-1}$) than does ascorbic acid and is not known to scavenge superoxide. [48] The diffusivity of both could be assumed to be equal as they have similar molecular weights (155 versus 176 g/mol). After adding histidine to a CdTe-2.4 QD suspension and illuminating with visible light, EPR results showed attenuation of the hydroxyl adduct signal by more than 50% (Figure 4a, b).

Importantly, a relatively high concentration of histidine (160 mM) was used to conclusively demonstrate hydroxyl scavenging because DMPO traps OH• approximately 10^8 times faster than O2•-. A high dose of scavenger is needed to compete with the concentration of spin trap DMPO used (90 mM). Since histidine did not appear to limit superoxide trapping in these conditions, this further confirmed the negligible reaction of histidine with superoxide. This experiment was also repeated with amino acids glycine and serine that show lower OH• reactivity, 1.7×10^7 and 3.2×10^8 $M^{-1}s^{-1}$, respectively. [48] Even at concentrations above 200 mM, no significant effect on the hydroxyl concentration was observed for these amino acids (Figure S7). We conducted a cell culture (E. coli MG1655; M9 minimal media; 25 nM CdTe-2.4) to observe whether the hydroxyl scavenging of histidine would protect the bacteria against therapeutic action from photoexcited quantum dots. We observed that, even at a concentration of 5.7 mM, the hydroxyl scavenger offered no significant protection to E. coli from the therapeutic effect of quantum dots (Figure 4c).
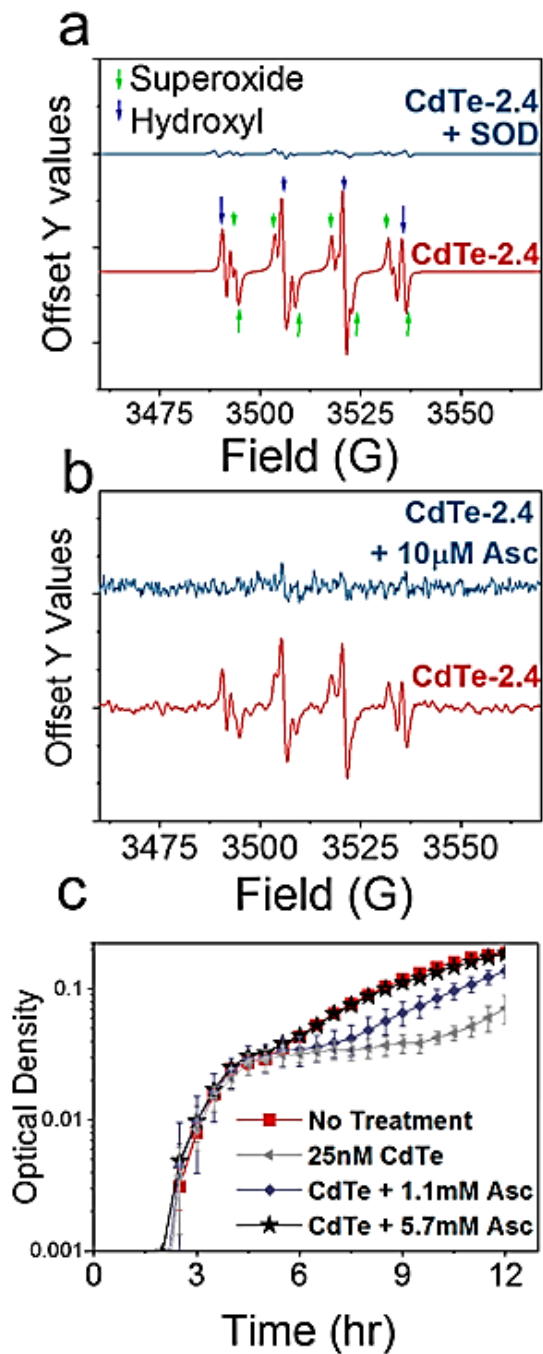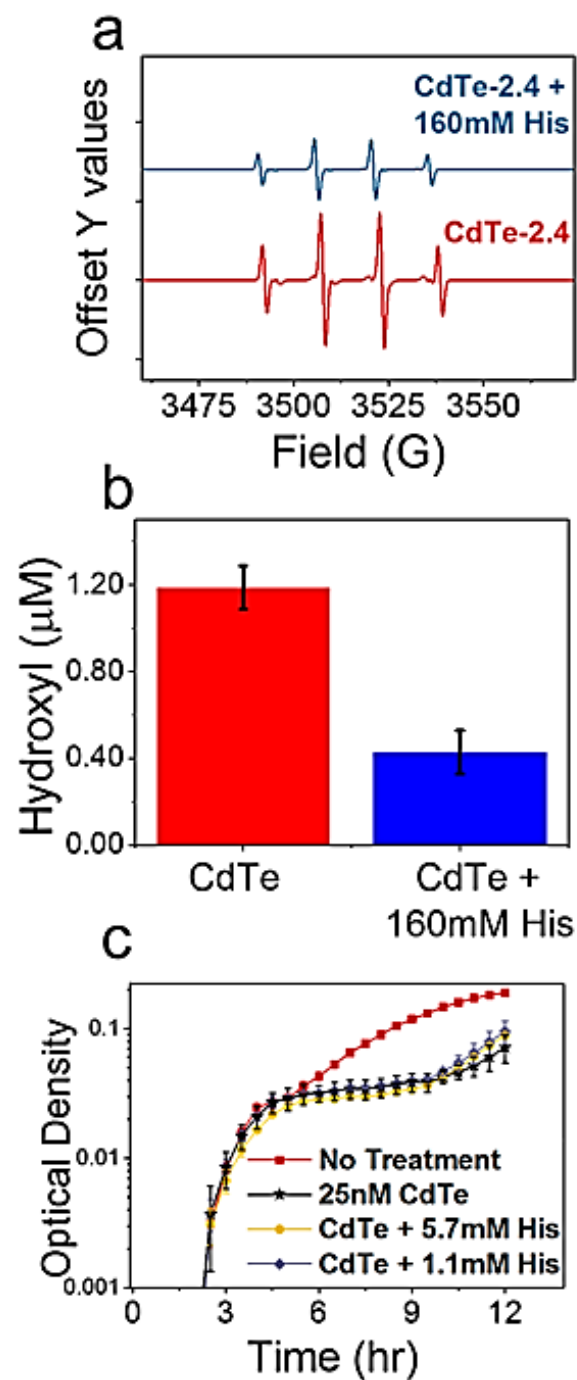
Figure 4. Effect of hydroxyl scavenger on EPR measurements and bacterial cultures. (a) EPR fitted spectra for photoexcitation of CdTe- 2.4 alone and in the presence of hydroxyl scavenger, histidine (His). Radical signal clearly attenuated, as shown by (b) quantification of hydroxyl concentration. (c) Growth curves for *E. coli* MG1655 in M9 minimal media with 25 nM CdTe-

2.4 and histidine. Bacteria grown with quantum dots display growth inhibition, even in wells supplemented with hydroxyl-scavenging histidine.

Taken together, these cell culture results confirm that the ascorbic acid's protective effect is attributable to its scavenging of superoxide rather than hydroxyl. By consequence, these results also provide further evidence that the intracellular generation of superoxide is responsible for the selective therapeutic action.

Superoxide Mechanism of Action. While superoxide has a high thermodynamic capacity to be a strong oxidant, it is not as directly reactive with common cell components such as peptides, carbohydrates, nucleic acids, or lipids.[49-51] Instead, superoxide is known to target enzymatic iron-sulfur clusters through electrostatic interactions not seen with other ROS.[44] Using E. *coli* strains engineered to express no SOD enzymes, Carlioz et al. showed that this renders the bacteria incapable of synthesizing adequate amounts of branched-chain, aromatic, and sulfur-containing amino acids, resulting in cell death.[52] Iron plays an important role in bacterial pathogenesis and host-pathogen interaction. Prior work has shown that some pathogenic bacteria will extract iron from iron-containing proteins in humans, such as transferrin. [53,54] Iron sequestration facilitates bacterial survival in hosts, but it could also render bacteria into regions of higher iron content relative to nearby cells. Given the $O_2^{\bullet-}$ affinity for iron, this may make pathogens particularly susceptible to a superoxide-driven mechanism like the one presented here, imparting more selectivity in targeting bacterial pathogens. Just as important, superoxide's relatively long lifetime allows it to target these consequential reactions more specifically. Considering a wide range of intracellular SOD concentrations from 1 to 20 μM,[55,56] we can estimate superoxide's intracellular diffusion

length to range from 220 nm to 1 μm (see Methods). In contrast, other ROS do not have the same combination of consequential reactivity and long lifetime. Hydroxyl radicals can readily oxidize proteins, lipids, and nucleic acids as well as abundant endogenous scavengers such as glutathione (GSH). [9,57] However, this indiscriminate reactivity translates to a short diffusion length for OH• within the cell. Reports in literature cite lengths of 3 nm.[55] Assuming a GSH concentration of 2 mM [57] (k = 1×10^{10} M^{-1}s^{-1}),[48] we can calculate an approximate diffusion length of 7 nm, three orders of magnitude shorter than that of superoxide.[58] This method likely overestimates the diffusion length of OH• because it does not take into account the presence of any other biomolecules. Despite singlet oxygen's diffusion length being on the same order as that of superoxide, [59] $^1O_2$ can be deactivated by reacting with water. [60] As a result, high doses of $^1O_2$ are needed to exhibit toxicity, evidenced by our assessment of different ROS. This was shown in an experiment by Ragas et´ al. where extending the $^1O_2$ diffusion length (using deuterated water) resulted in higher toxicity. [60] Therefore, the toxicity of photogenerated superoxide in such low doses likely hinges on the combination of the radical's diffusion length and specific intracellular targets (Figure 5)
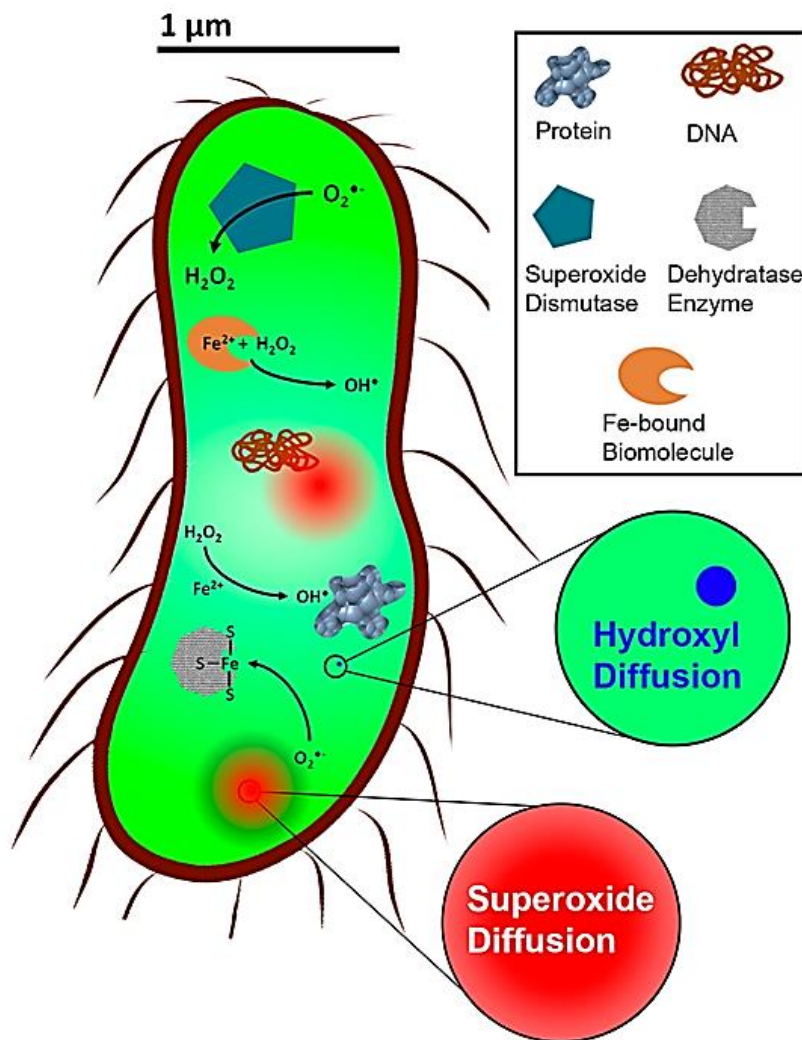
Figure 5. Importance of specific superoxide generation for nanotherapeutic efficacy. Schematic contrasting nanotherapeutic treatment of E. coli by superoxide and hydroxyl. Relative diffusion lengths depicted in red (superoxide, 220 nm) and blue (hydroxyl, 7 nm); relevant biomolecules (not to scale) depicted according to legend. Note that an *E. coli* cell should contain approximately 96 quantum dots. Potential extracellular effects not shown.

Next, we tried to quantify the internal radical concentration required for killing bacterial cells. To estimate this dose, we approximated the endogenous radical concentrations required to perturb the cellular homeostasis in bacterial pathogens. Bactericidal effect from

superoxide is possible if steady-state intracellular concentrations exceed approximately 0.1 nM.[35,61] For comparison, normal intracellular hydrogen peroxide concentrations for E. coli have been estimated at 20 nM,[35] and concentrations of approximately 1 mM are typically needed for toxicity via hydroxyl radicals.[36] Juxtaposing these intracellular thresholds with the estimated concentration of QD-photogenerated $O_2 \cdot -$ (Figure 6a), we see that at low light intensity (1-3 mW/cm^2, Figure S8), 50 nM CdTe-2.4 critically perturbs cellular redox homeostasis and leads to bacterial killing. An equivalent hydroxyl radical production. would be far below the critical threshold required for bacterial killing with OH• as the photogenerated ROS. Therefore, by increasing the superoxide scavenging using ascorbic acid, the toxicity of photoexcited quantum dots can be eliminated entirely (Figures 2 and 6a). Using a similar scavenging of hydroxyl radical fails to offer any observable reduction in the therapeutic action of CdTe-2.4 (Figure 6b).
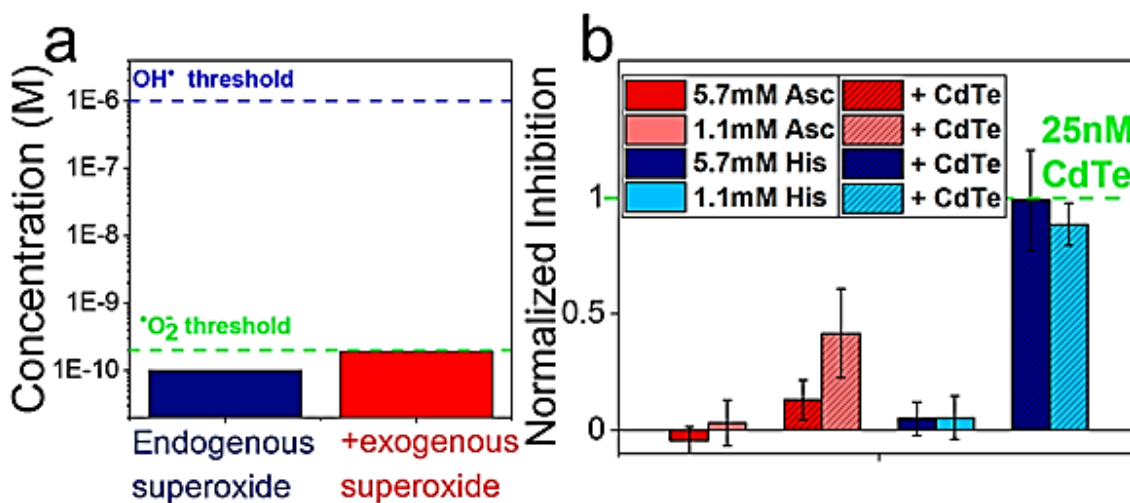
Figure 6. Superoxide toxicity and mechanism of action. (a) Estimated intracellular steady-state superoxide concentration with and without 50 nM CdTe-2.4 (see the Experimental Section). Comparison to thresholds for cellular damage (dashed lines) agrees with observations of QD-superoxide phototoxicity at nanomolar concentrations. (b) Normalized growth inhibition at 12

hrs (see the Experimental Section) for E. coli MG1655 treated with CdTe-2.4 (dashed line/boxes) in the presence of hydroxyl-scavenging histidine (His, blue) or superoxide-scavenging ascorbic acid (Asc, red). Statistically significant ($p < 0.05$) protection was only seen for cultures supplemented with a superoxide scavenger

Efficacy of Intracellular Superoxide Generation in treating Bacterial Infections.

In previous reports, we showed that photoexcited CdTe-2.4 killed multidrug-resistant bacteria, apparently, due to low bacterial tolerance for intracellular superoxide. To test the applicability of this mechanism of action, we evaluated the therapeutic effect of CdTe-2.4 on a screen of Gram-negative MDR pathogens. We obtained 45 drug-resistant strains of bacteria from three different species: *Klebsiella pneumoniae*, *E. coli*, and *Salmonella enteria*. Enterobacteriaceae such as these are severely antibiotic resistant, and some clinical isolates have 50% growth inhibition concentrations up to 1000 times higher than the breakpoints recommended by the Clinical and Laboratory Standards Institute.[39] We tested the sensitivity and resistance of each isolate to four different classes of antibiotics: an aminoglycoside (streptomycin), a carbapenem β-lactam (Meropenem), an amphenicol (chloramphenicol), and a second-generation fluoroquinolone (ciprofloxacin) to confirm their MDR phenotype. In most cases, the isolates were resistant to classes of antibiotic, including the carbapenem. Treatment with 50 and 100 nM of CdTe-2.4 resulted in growth inhibition of every isolate (Figure 7).
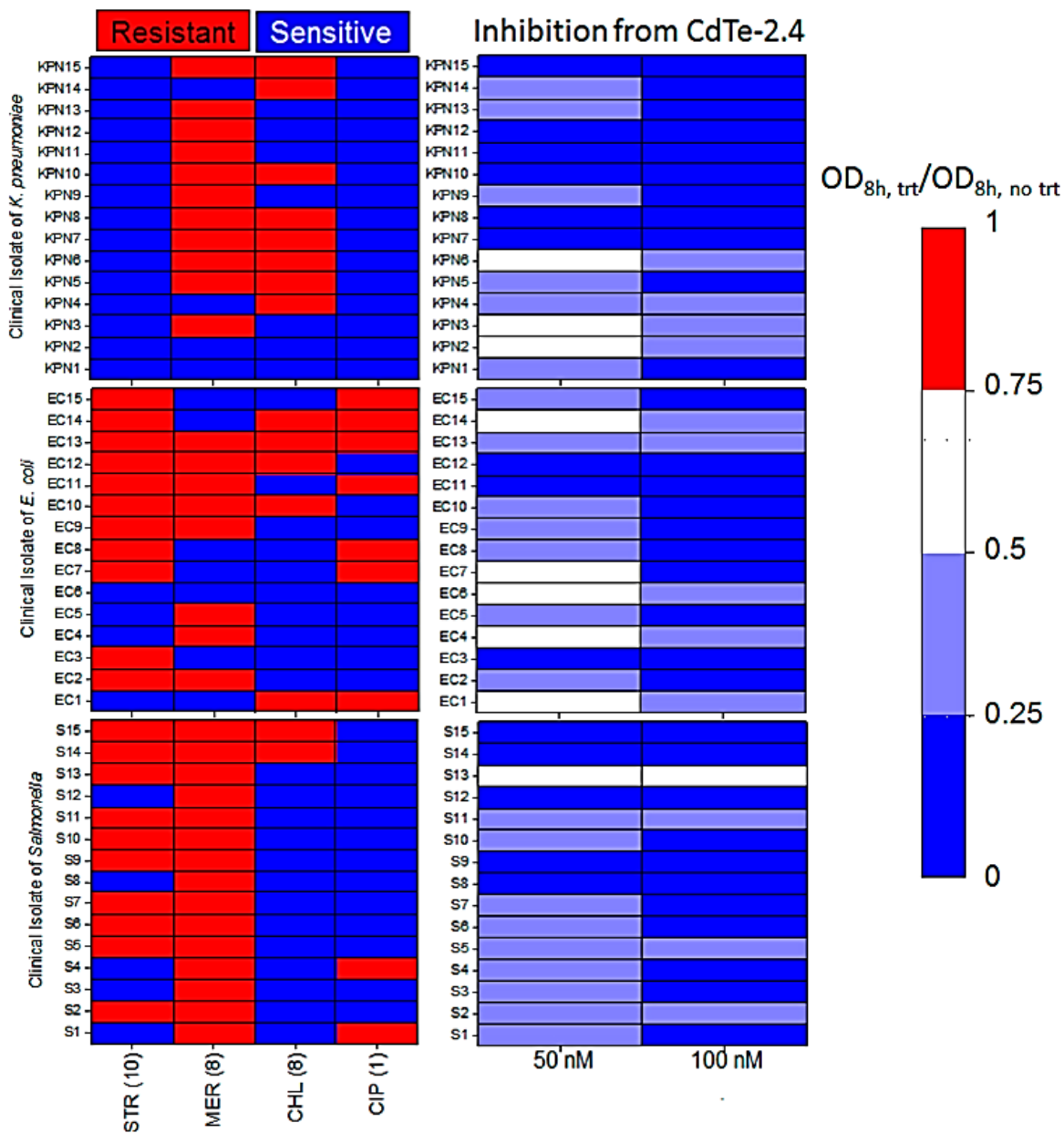
Figure 7. Therapeutic effect of CdTe-2.4 versus 45 multidrug-resistant clinical isolates. A total of 15 clinical isolates each from *Klebsiella pneumoniae* (KPN1-15), *E. coli* (EC1-15), and *Salmonella sp.* (S1-15) is shown here. Table (left) shows whether the clinical isolates are resistant (red) or sensitive (blue) to antibiotics based on CLSI breakpoints. Antibiotics tested were streptomycin (STR), meropenem (MER), chloramphenicol (CHL), and ciprofloxacin (CIP) at concentrations given in parentheses (μg/mL). Significant growth inhibition was observed when these multidrug-resistant strains were treated with monotherapy of CdTe-2.4

and visible light (center). Dose-dependent growth inhibition is observed after 8 h of exposure, relative to the untreated control. Relative inhibition is shown according to the color scale shown in the legend (right).

Inhibition was dose-dependent and was even observed in the isolate that showed resistance to all four classes of antibiotics (EC-13). This result demonstrates that the quantum dot's mechanism of action is broad in its applicability and is effective against bacteria with a range of MDR phenotypes. The antibiotics used normally treat infection by inhibiting protein synthesis (STR, CHL), inhibiting cell wall synthesis (MER), and preventing DNA duplication (CIP). Nevertheless, bacterial strains genetically equipped to defend against these attacks were unable to defend against the onslaught of intracellular superoxide generated by CdTe-2.4.

Rational Design of Quantum States for Specific Superoxide Generation.

Based on the investigation of different ROS, we recognized that rational design of nanotherapeutics should revolve around the ability to specifically generate intracellular superoxide. The ability of a photoexcited quantum dot to generate ROS is tightly controlled by the position of a material's band positions relative to specific redox half reactions, such as superoxide generation from oxygen. More specifically, in the case of CdTe-2.4, the ability to generate superoxide is entirely determined by the energetic position of its conduction band. These band positions can be changed by tuning the size or composition of QDs. Simply changing the size of the QDs from 2.7 to 3.3 nm (Figure S9) leads to a significant change in band gap (2.4-2.2 eV). With CdTe-2.2, a smaller overpotential for electron injection results in reduced superoxide generation and subsequent therapeutic effectiveness (Figure S10). By changing the QD material from CdTe to CdSe while holding constant the nominal band gap,

we were able to further illustrate the effect of band alignment with redox half reactions. The valence band position, dictated by either Te or Se, is higher in CdTe versus CdSe. As a result, in CdSe-2.4, the conduction band is not suitably positioned for superoxide generation, as shown in the supplemental Figure S11b. Consequently, EPR and cell culture results show a negligible radical generation and therapeutic effect, respectively (Figure S11). Such investigations reinforce two key notions: first, superoxide generation is critical for this selective mechanism; second, QD materials can be rationally engineered to generate superoxide using visible light.

Conclusion

In conclusion, we have assessed different ROS and found that only superoxide is suitable for application as a selective therapeutic or antimicrobial. Since the superoxide anion is charged and cannot transport across the cellular membrane, we utilized small rationally designed QDs that diffuse through the cell and use light as an external trigger to generate intracellular superoxide for therapeutic effect. We identified that, upon activation with visible light, intracellular superoxide can disrupt iron-sulfur clusters and is much more selective in its action than another ROS that cause nonselective cell damage. This selectivity of therapeutic effect from superoxide stems from three key elements: its specific deactivation of key enzymes required for pathogen survival, rather than indiscriminate oxidative damage of cellular components like DNA, lipids, and proteins; selective killing of pathogens in a window of dosage where mammalian cells are not harmed by low QD concentrations; and targeted intracellular generation by using precisely tuned redox states of QDs. Further, because $O_2\bullet-$ can diffuse over greater distances and is only present in sub nanomolar concentrations, rationally designed CdTe-2.4 QD's ability to directly form intracellular exogenous superoxide offers

specific toxicity in bacterial pathogens that would not be possible with another ROS. We have also demonstrated design rules for coordinating QD material and size to the relevant redox chemistry. These rules can be used to design new QD nanotherapeutics for further applications in selective therapeutics as precision medicine for a range of diseases from infections caused by multidrug-resistant pathogens to cancer cells.

Experimental Section

Quantum Dot Synthesis. CdTe and CdSe QDs were synthesized in aqueous media as described in our previous report. [28]

Quantum Dot Characterization. Absorbance spectra were measured on a VWR UV 1600PC UV/vis spectrophotometer. Emission spectra were obtained on a calibrated PTI fluorimeter with QYs calculated relative to a fluorescein isothiocyanate standard (Sigma). A Philips CM 100 microscope was used to obtain TEM (transmission electron microscopy) images of the nanoparticles, the size distributions of which were analyzed using ImageJ.

Cell Culture Conditions. Individual colonies of E. coli MG1655 were selected from solid LB media (2% LB, 1.5% agar) and incubated overnight (16 hrs) at 37 °C with shaking at 225 rpm in liquid LB (2% LB). Overnight cultures were subsequently diluted (1:100) into fresh M9 minimal medium for experiments in 96-well culture plates. For superoxide treatment, CdTe-2.4 quantum dots were suspended in cell culture media and added to corresponding wells. Potential ROS scavengers, ascorbic acid, histidine, glycine, and serine (Sigma), were dissolved in M9 minimal medium prior to use. For assessment of other ROS types, known concentrations of hydrogen peroxide were added directly to cell culture media in

a 96-well plate. Next, corresponding concentrations of FeSO$_4$ (hydroxyl) and NaOCl (singlet oxygen) were prepared and added to appropriate wells containing hydrogen peroxide, cell media, and cell dilutions. ROS concentrations ranged from 1 μM to 10 mM. ROS generating reactions were assumed to proceed to a full extent. Further details are provided in the Supporting Information. The optical density of individual wells was measured at 590 nm using a Tecan GENios microplate reader. For quantum dot experiments, the light source for cell culture was affixed to the ceiling of the microplate reader to provide constant light exposure for the duration of the experiments. We used a thin sheet of visible-LEDs with a known spectrum (Figure S8) affixed to the roof of the microplate reader. Optical density measurements were taken every 30 min. Data represents the average of three biological replicates and error bars span two standard deviations from the average.

Multidrug-Resistant Clinical Isolate Screen. Clinical isolates were

obtained from the University of Colorado Anschutz Campus in Denver, CO. Isolates were streaked out on to solid cation adjusted Mueller Hinton broth (1.5% agar) (CAMHB; VWR), and individual colonies were selected and grown overnight (16 hrs) with 225 rpm shaking in liquid CAMHB prior to testing. Cultures were diluted (1:100) (approximately a 0.5 McFarland standard) and added into wells in CAMHB with various CdTe-2.4 concentrations. Optical density was measured as described above with illumination. Antibiotic susceptibility screening was performed with overnight cultures diluted to a 0.5 McFarland standard. Antibiotic concentrations were as follows: 10 μg/mL of streptomycin, 8 μg/mL of meropenem, 8 μg/ mL of chloramphenicol, and 1 μg/mL of ciprofloxacin.

Cyclic Voltammetry. CV was performed with a three-electrode configuration in PBS, with a glassy carbon plate, platinum wire, and Ag/AgCl as working, counter, and reference electrodes, respectively. Electrochemical measurements with visible light irradiation were performed using the same setup with a halogen lamp as a light source. For measurements in oxygen-free buffer, the solvent was bubbled with argon and an argon-rich headspace was maintained.

Electron Paramagnetic Resonance (EPR). Quantum dot samples were prepared for EPR by washing with pH 11 water to remove excess precursor and metal ions, followed by resuspension in PBS. ROS scavengers were dissolved in PBS prior to use. For experiments, quantum dots suspensions were mixed with a selective ROS scavenger. One μL of spin trapping agent DMPO (Dojindo) was used for every 100 μL of sample. After DMPO addition, exposure to light was minimized by wrapping the mixture in foil. Three quartz capillaries were loaded with the samples and measured in a Bruker Elexsys E 500 spectrometer (SHQE resonator) using a microwave attenuation of 16 dB, power of 5 W, and operated in a dark room. After tuning the machine, baseline measurements were taken in the dark to serve as a baseline for measurements after illumination. QD samples were then exposed to 45s of white light (9 mW/cm2) and immediately returned to the EPR cavity for spectrum collection. This scheme mitigated any potential effects from incidental exposure to ambient light and the background signal from the quartz capillaries (E′ defect). Both dark and light measurements consisted of 10 consecutive scans (20.48 s each) over a range of 200 G (0.05 G resolution) centered on 3515 G. The presence of DMPO adducts was confirmed using Bruker's SpinFit software, which was also used to fit measured spectra. Assessment of other ROS types did not require a light source. Chemical mixtures of peroxide and FeSO4 (to yield hydroxyl) or NaOCl

(to yield singlet oxygen) were mixed in the presence of spin trapping agents DMPO and TMP, respectively. Concentrations of the hydroxyl and superoxide present were determined using SpinFit (Bruker). Spectra were fitted to the appropriate parameters and double integrated, yielding a count of spins detected from DMPO-ROS adducts. Radical concentrations were then calculated using the known active volume consistent across all samples.

Redox Staining. Cultures of E. coli were exposed to CdTe- 2.4 for 2 hrs in light and dark conditions and then incubated with 2′,7′-dichlorofluorescein diacetate for 5 min. When exposed to oxidizing species like hydroxyl radicals, the dye becomes a green fluorophore (Figure S13).

Normalized Inhibition. Normalized inhibition was calculated according to the following equations. The Δ in optical density is with respect to the growth of bacteria without quantum dot treatment. Resulting values are normalized to the Δ of between the quantum dot control (no scavenger supplement) and no treatment. Note that the figure (Figure 6b) shown represents growth at t = 12 hrs.

$$\Delta OD_{treatment} = OD_{treatment, t=12h} - OD_{notreatment, t=12h} \qquad (1)$$

$$inhibition = \frac{\Delta OD_{treatment}}{\Delta OD_{CdTecontrol}} \qquad (2)$$

Diffusion Calculations. Approximate diffusion lengths were calculated from pseudo-first-order rate constants. Pseudo-first-order rate constants were calculated based on data from the literature on intracellular concentration of ROS scavengers and their respective

second-order rate constants (k). Diffusion coefficients (D) were assumed to be $1 \times 10^{-5} \text{cm}^2/\text{s}$ (small molecules). Diffusion lengths (l) could then be estimated using the following equation:

$$l = \sqrt{\frac{D}{k_1}}$$

$$(3)$$

Quantification of Photogenerated ROS. To estimate the amount of photogenerated ROS, we wanted to consider the conditions used in cell culture. As such, we used the light power corresponding to thin LED sheet for our calculations. The superoxide production rate was estimated using measured values of light flux (1.6 mW/cm^2) and absorbance spectra for light above 520 nm. We assumed a known quantum dot concentration (50 nM) and a 20% quantum yield for direct charge injection into molecular oxygen. Together, this allows us to calculate the amount of superoxide generated per unit of light and unit of time. We then estimated the amount of superoxide produced per quantum dot. This value was combined with the lifetime of superoxide radicals (assuming a 1 μm diffusion length) to determine superoxide dosage. Intracellular steady state concentrations of superoxide were calculated based on data for SOD activity, and endogenous superoxide concentration in *E. coli*, using previous methods. [56]

Supplementary Methods

Determining ROS/RNS Concentration. Individual concentrations were calculated based on known chemistry for each specific reaction. For cell culture experiments, concentrations were varied from 1 µM to 10 mM.

Hydrogen peroxide: Originally in dilute form (30%), equating to 9.8 M. Target concentrations were obtained via serial dilution in sterile water and ultimate dilution in cell media, assuming 10% of the final volume will be added as dilute cell suspension. For example, dilution to 10 mM calculated as follows:

$$Starting\ Concentration = 9.8\ M$$

$$Target\ Final\ Concentration = 10\ mM$$

$$\frac{Target\ Concentration}{Starting\ Concentration} \div 0.9 = {0.0011\ \mu l\ stock}\Big/{\mu l\ final\ volume}$$

Lower concentrations are administered via further serial dilution to maintain relative ratios

Hydroxyl Radicals: Hydroxyl radicals are generated upon reaction of hydrogen peroxide and $FeSO_4$. We assumed that this favorable reaction proceeds to completion. Hydrogen peroxide concentration was calculated as described above. FeSO4 in powder form was measured to give an equimolar ratio with hydrogen peroxide (Molecular weight = 151.908 g/mol).

Singlet Oxygen: Singlet oxygen dosage was calculatedly similarly to that of hydroxyl radicals. Hydrogen peroxide reacts favorably with NaOCl, and we assume complete

reaction. The stock used contained 5.25% NaOCl diluted in water. A diluted version of the stock was combined with hydrogen peroxide in an equimolar fashion, corresponding to each dose.

Nitric Oxide: Nitric oxide was generated using nitric oxide generating DPTA-NONOate (Cayman Chemical). DPTA-NONOate spontaneously disassociates over a steady period (half- life of three hours) at 37 °C to form 2 molecules of NO per molecule of compound. Sample was initially diluted in sterile water, and further diluted in cell media prior to treatment. Dosage was calculated based on a molecular weight of 191.2 g/mol.

Superoxide: Superoxide concentration was determined based on the concentration of CdTe-2.4 and measured values of light flux.

Supplementary Figures
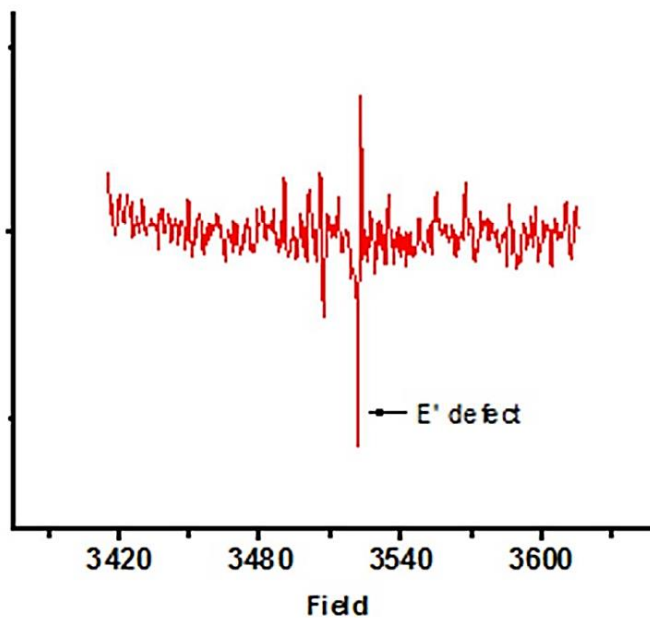
Figure S1. E' Defect on dark spectra. Characteristic EPR signal for the E' defect associated with the quartz capillary tubes used in the EPR cavity.
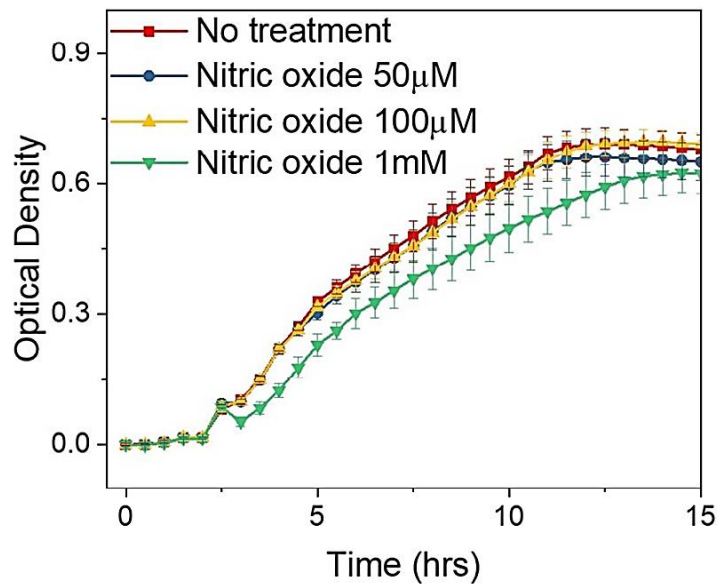
Figure S2. Therapeutic assessment of RNS. Growth curves for *E. coli* MG1655 treated with different doses of nitric oxide (NO) using slow release through DPTA-NONOate. Minimal toxicity is seen till 1 mM NO concentration.
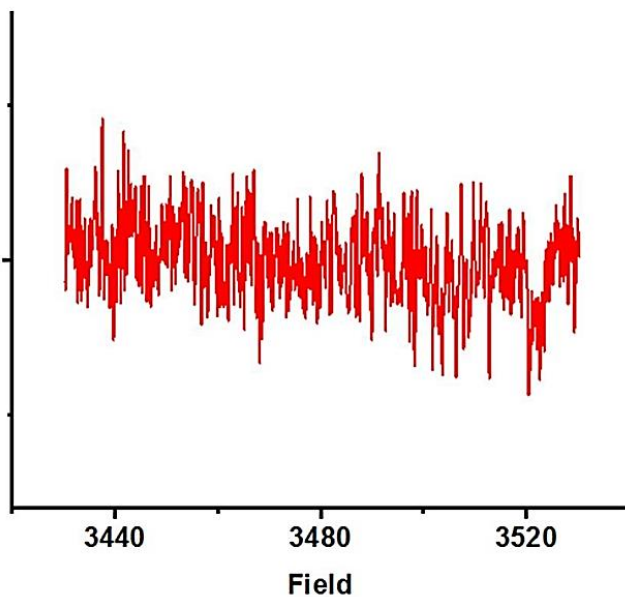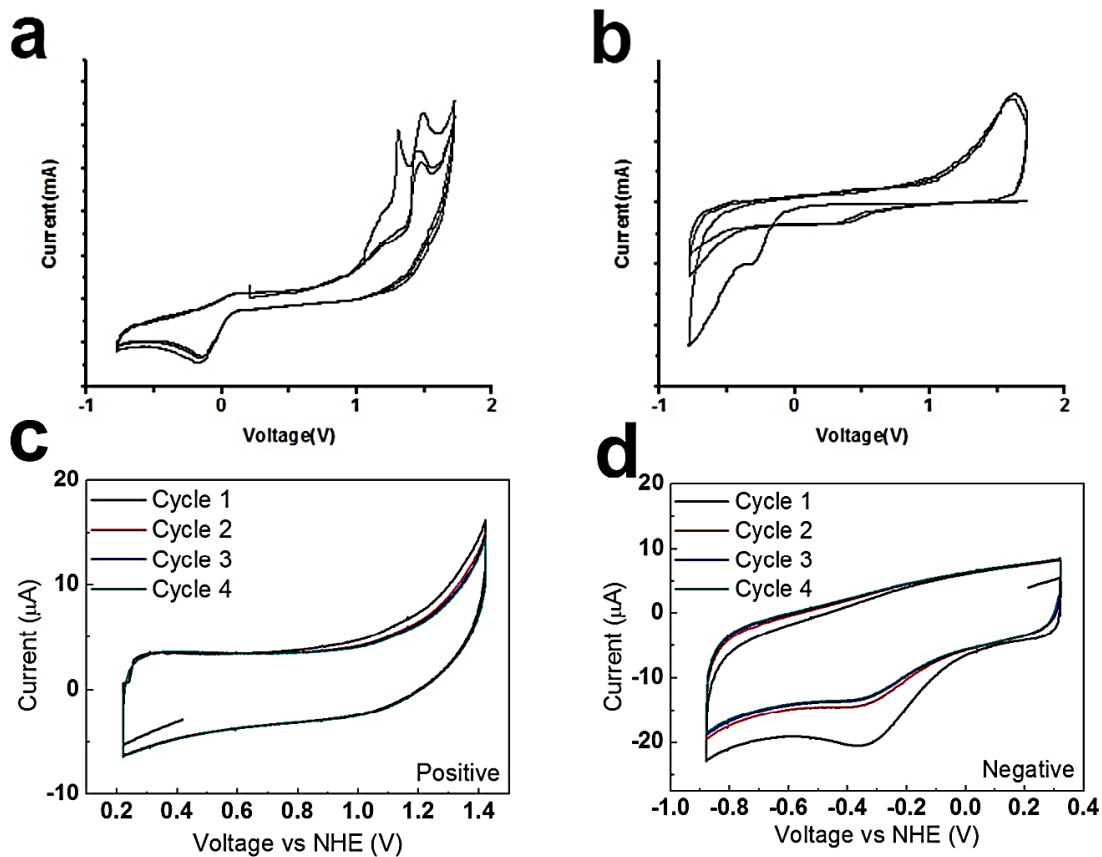
Figure S4. Cyclic voltammograms. a) Cyclic voltammetry measurements of CdTe-2.4 in PBS. **b)** CV measurement after bubbling the solution with argon to remove dissolved oxygen. [39] Half cycle CV runs for **c)** positive, and **d)** negative potentials, for CdTe-2.4 in PBS. Removal of dissolved oxygen eliminates the peaks associated with superoxide and hydroxyl radicals. Because only the formation superoxide depends on the presence of oxygen, these results indicate that hydroxyl formation is a consequence of superoxide generation. Half-cycle (with scans limited to either the positive or negative potentials) experiments in air saturated buffer

show no hydroxyl generation, further disproving the direct hole injection from photo-excited CdTe-2.4. This indicates that superoxide is the primary radical formed by direct electron injection from CdTe-2.4.
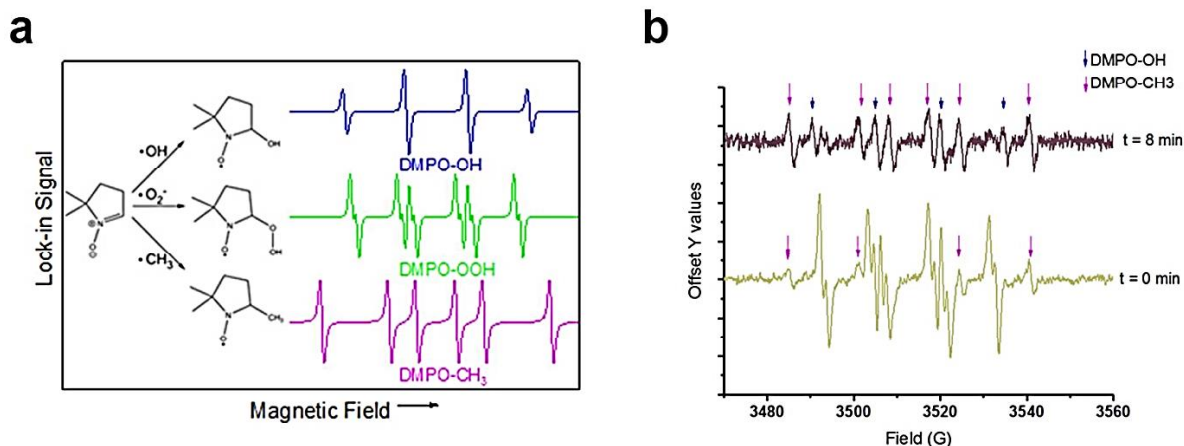
Figure S5. EPR Spectra showing the indirect generation of hydroxyl radicals. a) Typical EPR spectra for radical adducts of DMPO with hydroxyl (blue), superoxide (green), and methyl (pink) radicals. **b)** EPR spectra for CdTe-2.4 in the presence of DMSO at 0 minutes (bottom) and 8 minutes (top) after illumination. Initial spectra show clear DMPO-OOH peaks indicating direct superoxide generation. Some signal for DMPO-CH3 begins to show. As time passes, DMSO reacts with the free hydroxyl radicals formed indirectly, forming more methyl radicals and the DMPO-CH3 signal grows. This growth occurs at the expense of DMPO-OH and DMPO-OOH, confirming that, under normal conditions, the hydroxyl radical forms indirectly from superoxide generation. To confirm that OH● detected by EPR was a result of the decomposition of DMPO-OOH, we repeated the EPR experiment in the presence of dimethyl sulfoxide (DMSO). Any free hydroxyl radicals can attack the sulfur of DMSO and release methyl radicals into solution, which can then form detectable adducts with DMPO (Fig. S5). Immediately after light stimulation of CdTe-2.4 in 10% DMSO, we observed characteristic features of DMPO-CH3. In later time points, DMPOCH3 became a dominant species in the spectra at the expense of DMPO-OH and DMPO-OOH. This confirmed that hydroxyl radicals were formed freely in solution, likely through decomposition of the DMPO-OOH adduct, rather than by direct conversion between adducts. Conveniently, this mechanism is analogous to the biochemical route involving superoxide dismutase (SOD) enzyme and Fenton-active iron. [14,16]
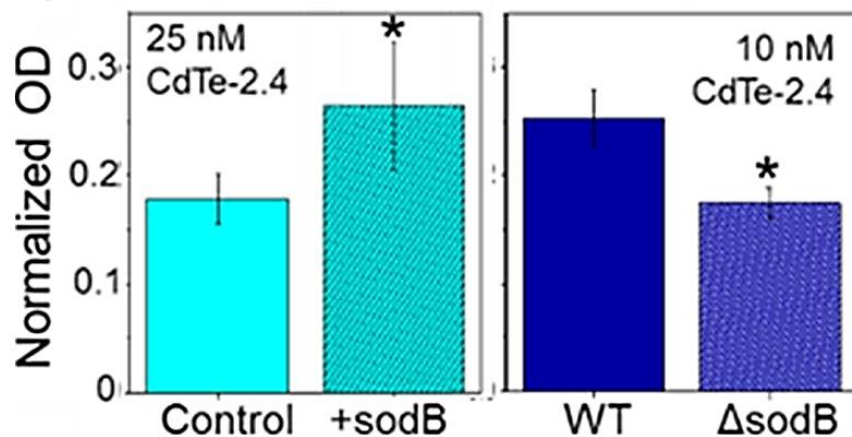
Figure S6. Therapeutic effect of CdTe-2.4 on mutant *E. coli* with over expression and deletion of SOD B enzyme (Reprinted by permission of the American Association for the Advancement of Science). Overexpression (left) shows reduced inhibition versus control; sodB deletion strain (right) shows increased inhibition versus wild type (WT). [37]
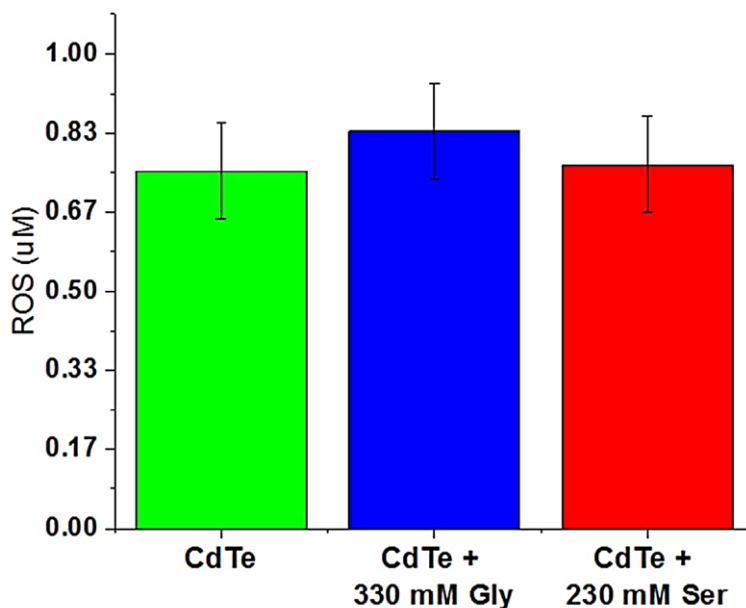
Figure S7. Lack of hydroxyl scavenging in EPR by other amino acids. Measurement of the hydroxyl radical concentration (via EPR) 250 seconds after illumination of CdTe-2.4 suspension alone (red) and in the presence of glycine and serine amino acids. Although they

are present in higher concentrations than histidine, they do not comparable scavenging of the hydroxyl radical.
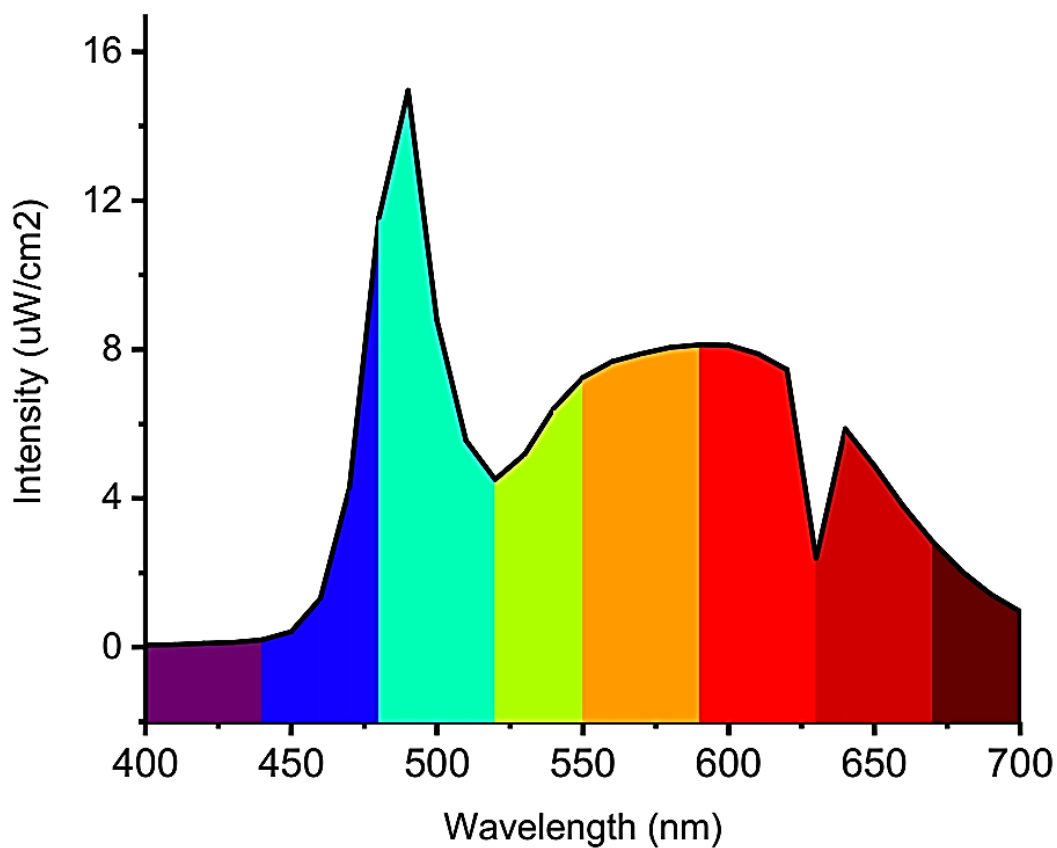
Figure S8. Emission spectra for LED sheet used to photo-excited CdTe-2.4 *in vitro*.
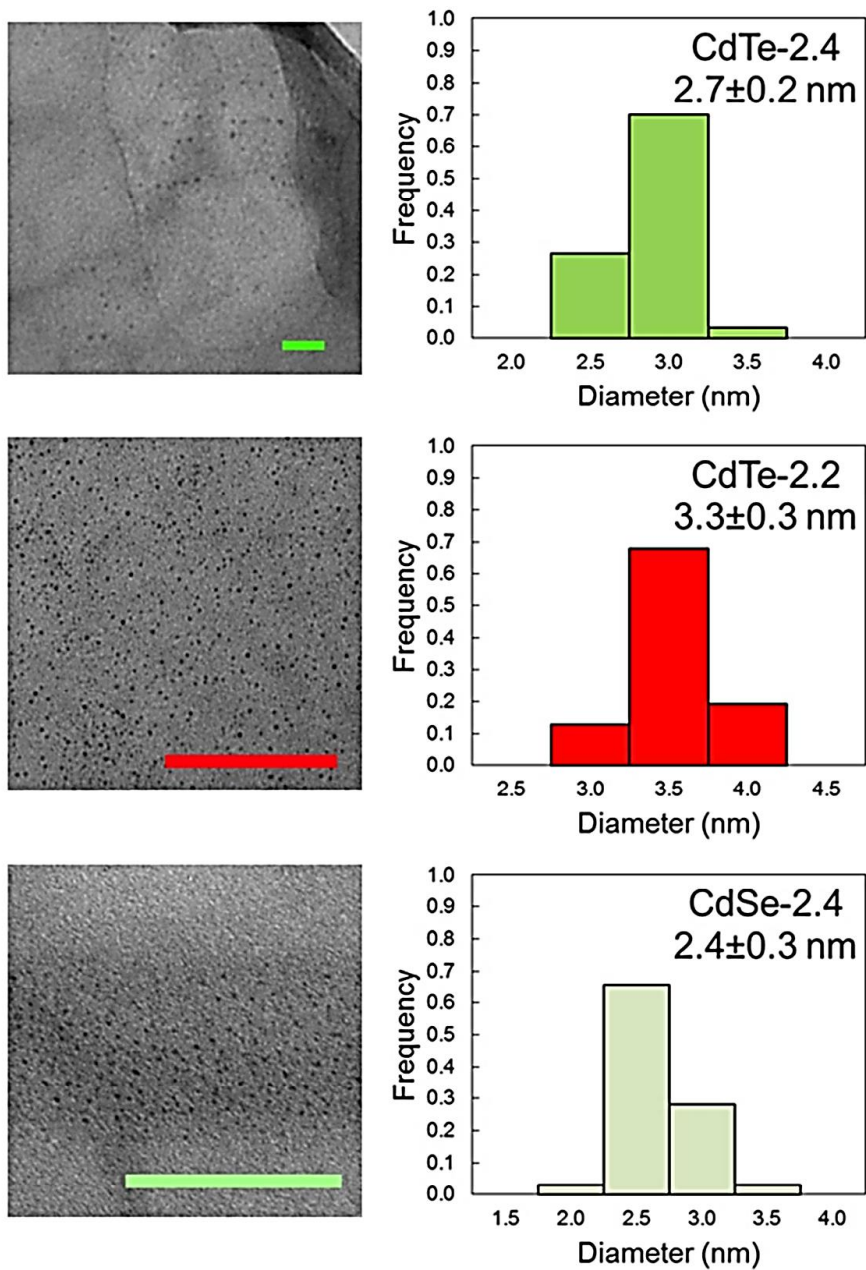
Figure S9. TEM images and size distribution histograms for the nanoparticles used in cell culture. Scale bars are 100 nm for CdSe-2.4 and CdTe-2.2, and 20 nm for CdTe-2.4.
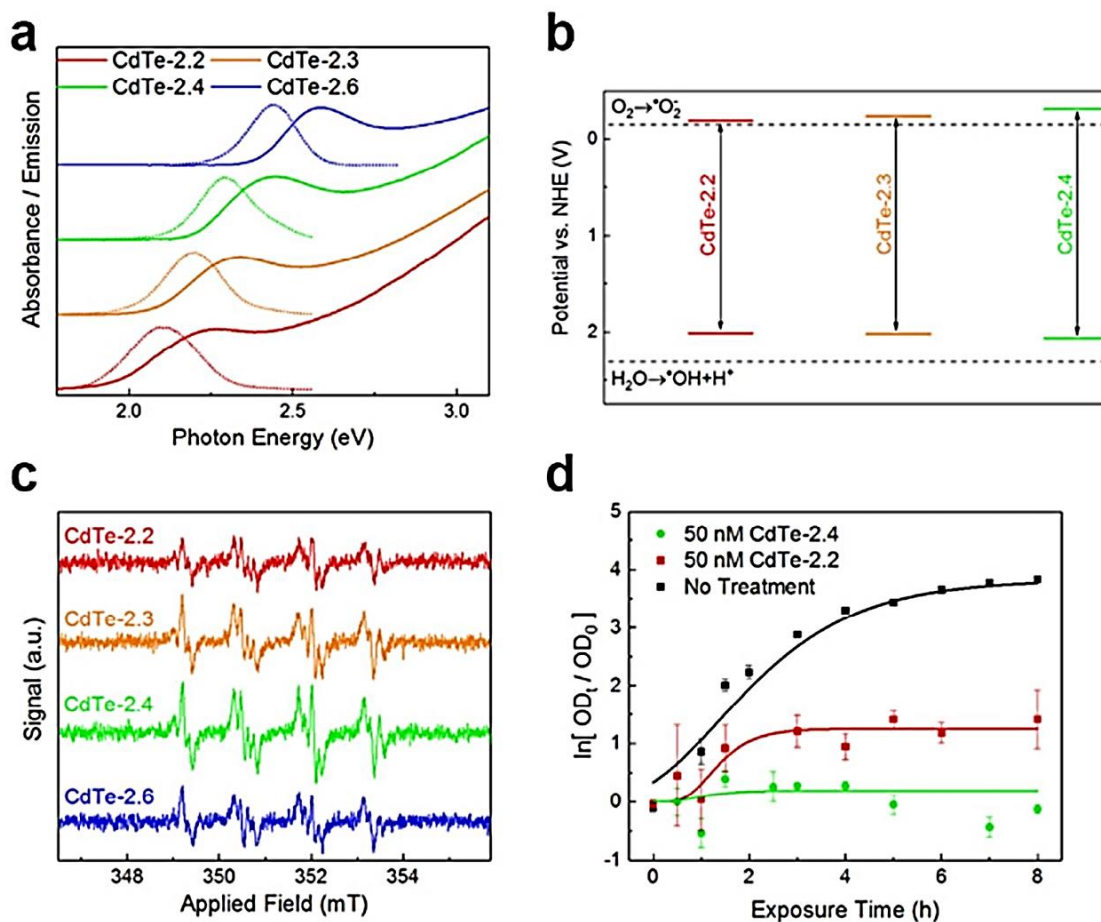
Figure S10. Effect of different sized QDs on energy states and radical generation. a) Absorbance and emission spectra of different sized CdTe QDs. **b)** Conduction-valence band positions for different sized QDs. Larger quantum dots (smaller bandgaps) show lower conduction bands and less overpotential for water reduction. **c)** Unnormalized EPR spectra for different sized CdTe quantum dots. **d)** Normalized growth curves of E. coli exposed to different QD sizes at the same concentration versus untreated controls.
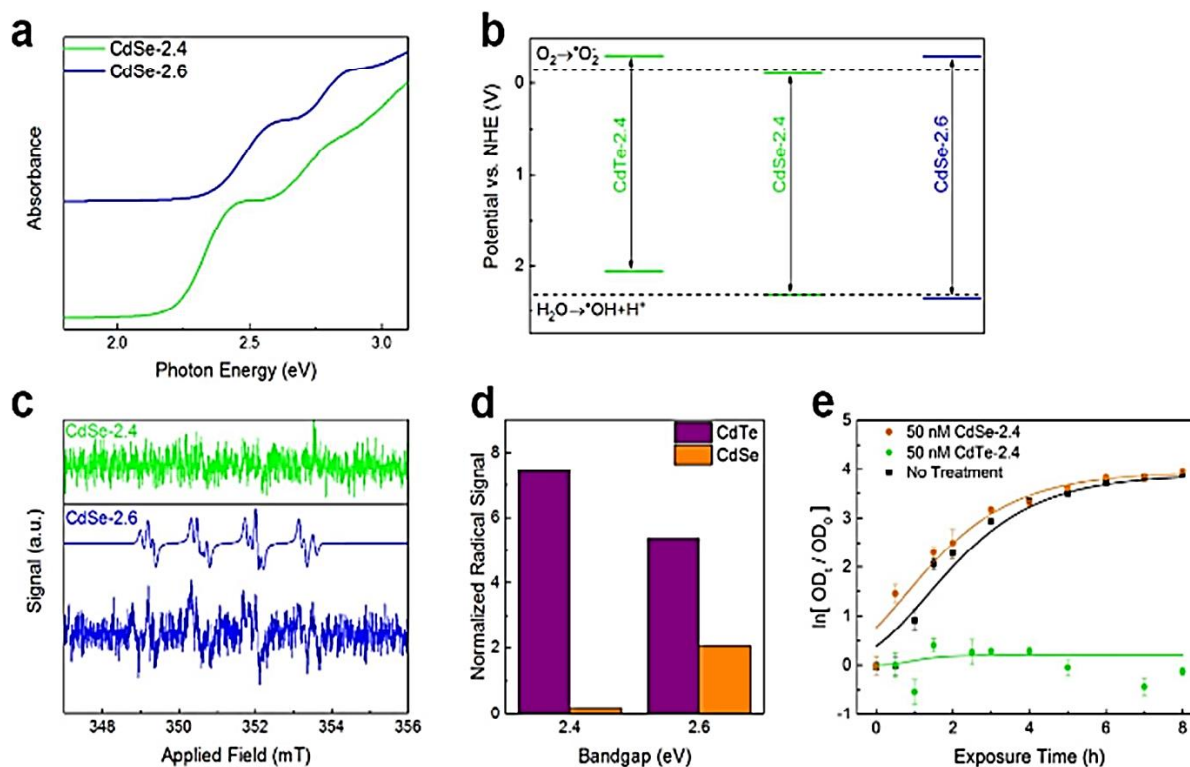
Figure S11. Effect of QD material on energy states and radical generation. a) Absorbance and emission spectra of CdTe and CdSe QDs. **b)** Conduction-valence band positions for different sized CdSe QDs versus CdTe-2.4. Although CdSe-2.4 has the same bandgap, it is unable to directly form superoxide as shown in the **c)** Unnormalized EPR spectra for different sized CdSe quantum dots. **d)** Integrated EPR signal as a function of QD bandgap comparing CdSe to CdTe. **e)** Normalized growth curves of E. coli exposed to CdSe-2.4 and CdTe-2.4 at the same concentration and untreated controls.
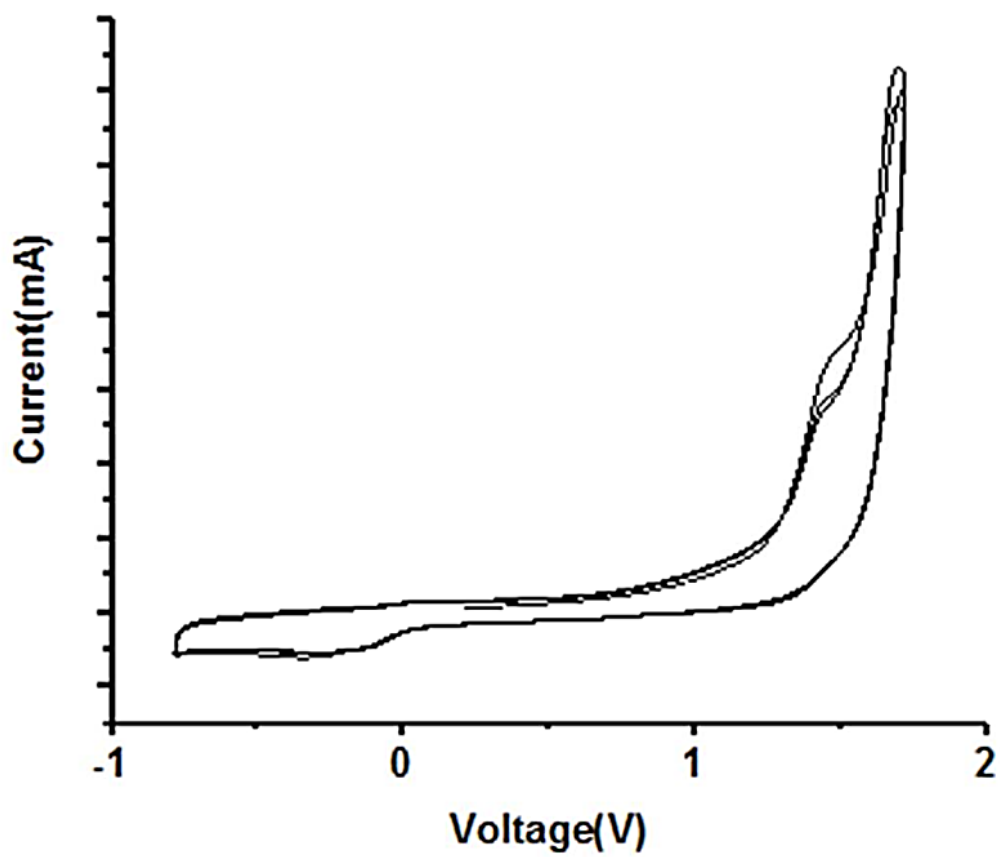
Figure S12. Cyclic voltammograms of CdTe-2.2. Peaks corresponding to superoxide and hydroxyl formation are not visible due to the altered conduction valence band positions of the larger quantum dots.
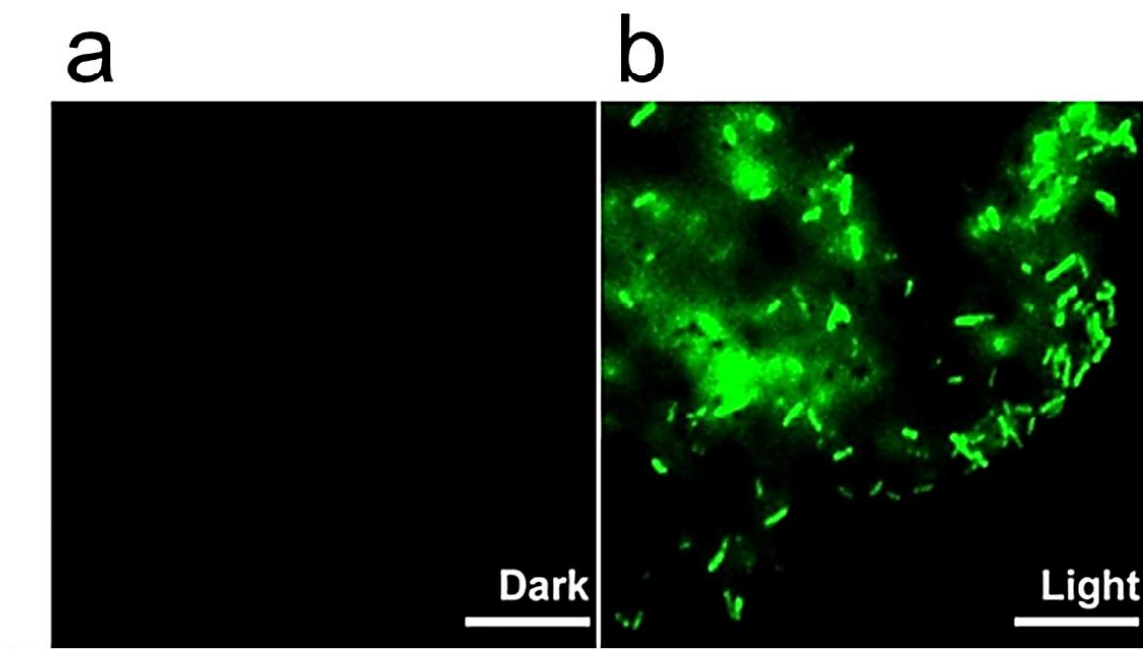
Figure S13. Redox activity of photoexcited CdTe-2.4. a) No redox activity detected before CdTe-2.4 exposed to light. **b)** Detection of intracellular ROS via 2',7'-dichlorodihydrofluorescein diacetate or DCF-DA (See methods). Free diffusion of small QDs (~3 nm) though bacterial pores (~20nm) followed by light activation leads to intracellular generation of superoxide. DCF-DA dye used here, converts to green fluorescent 2',7'-dichlorofluorescein in presence of ROS species like superoxide.

References

1. Di Meo, S.; Reed, T. T.; Venditti, P.; Victor, V. M. Role of ROS and RNS Sources in Physiological and Pathological Conditions. Oxid.Med.Cell.Longevity 2016, 1245049, 1-44.

2. D'Autreaux, B.; Toledano, M. B. ROS as Signalling Molecules: ́ Mechanisms That Generate Specificity in ROS Homeostasis. Nat. Rev. Mol. Cell Biol. 2007, 8 (10), 813-824.

3. Crack, J. C.; Green, J.; Cheesman, M. R.; Le Brun, N. E.; Thomson, A. J. Superoxide-Mediated Amplification of the Oxygen Induced Switch from [4Fe-4S] to [2Fe-2S] Clusters in the Transcriptional Regulator FNR. Proc. Natl. Acad. Sci. U. S. A. 2007, 104 (7), 2092-2097.

4. Zheng, M.; Aslund, F.; Storz, G. Activation of the OxyR Transcription Factor by Reversible Disulfide Bond Formation. Science 1998, 279 (March), 1718-1722.

5. Lee, J. W.; Helmann, J. D. The PerR Transcription Factor Senses H_2O_2 by Metal CatalysedHistidineOxidation.Nature2006,440(7082),363-367.

6. Fuangthong, M.; Atichartpongkul, S.; Mongkolsuk, S.; Helmann, J. D. OhrR Is a Repressor of ohrA, a Key Organic Hydroperoxide Resistance Determinant in Bacillus Subtilis. J. Bacteriol.2001,183(14),4134-4141.

7. Bogdan, C. Nitric Oxide and the Immune Response. Nat. Immunol. 2001, 2 (10), 907-916.

8. Vatansever, F.; de Melo, W. C. M. A.; Avci, P.; Vecchio, D.; Sadasivam, M.; Gupta, A.; Chandran, R.; Karimi, M.; Parizotto, N. A.; Yin, R.; Tegos, G. P.; Hamblin, M. R. Antimicrobial Strategies Centered around Reactive Oxygen Species - Bactericidal Antibiotics,
Photodynamic Therapy, and beyond. FEMS Microbiol. Rev. 2013, 37 (6),955-989.

9. Davies, M. J. The Oxidative Environment and Protein Damage. Biochim. Biophys. Acta, ProteinsProteomics2005,1703(2),93-109.

10. Davies, M. J. Singlet Oxygen-Mediated Damage to Proteins and Its Consequences.Biochem. Biophys. Res. Commun. 2003, 305 (3), 761-770.

11. Finkel, T.; Holbrook, N. J. Oxidants, Oxidative Stress and the Biology of Ageing. Nature 2000,408(6809),239-247.

12. Radi, R. Peroxynitrite, a Stealthy Biological Oxidant. J. Biol. Chem. 2013, 288 (37), 26464-26472.

13. Pacher, P.; Beckman, J. S.; Liaudet, L. Nitric Oxide and Peroxynitrite in Health and Disease.Physiol.Rev.2007,87(1),315-424.

14. Candeias, L. P.; Wardman, P. Introduction to Fenton Chemistry. Radiat. Res. 1996, 145 (5),523-531.

15. Bielski, B. H. J.; Allen, A. O.; Schwarz, H. A. Mechanism of the Disproportionation of Superoxide Radicals. J. Am. Chem. Soc. 1981, 103 (12), 3516-3518.

16. McCord, J. M., Fridovich, I. Superoxide Dismutase. Methods Enzymol. 1969, 349.

17. Pryor, W. A.; Squadrito, G. L. The Chemistry of Peroxynitrite: A Product from the Reaction of Nitric Oxide with Superoxide. Am. J. Physiol. 1995, 268, L699-722.

18. Hirsch, L. R.; Stafford, R. J.; Bankson, J. A.; Sershen, S. R.; Rivera, B.; Price, R. E.; Hazle, J. D.; Halas, N. J.; West, J. L. NanoshellMediated near-Infrared Thermal Therapy of Tumors under Magnetic Resonance Guidance. Proc. Natl. Acad. Sci. U. S. A. 2003, 100 (23),13549-13554.

19. Huang, X.; El-Sayed, I.; Qian, W.; El-sayed, M. A. Cancer Cell Imaging and Photothermal Therapy in the Near-Infrared Region by Using Gold Nanorods. J. Am. Chem. Soc. 2006, 128 (3), 2115-2120

20. Hamblin, M. R.; Hasan, T. Photodymamic Therapy: A New Antimicrobial Approach to Infectious Disease? Photochem. Photobiol. Sci. 2004, 3 (5), 436-450.

21. Dai, T.; Huang, Y.-Y.; Hamblin, M. R. Photodynamic Therapy for Localized Infections - State of the Art. Photodiagn. Photodyn. Ther. 2009, 6, 170-188.

22. Lu, K.; He, C.; Lin, W. J. Am. Chem. Soc. 2014, 136, 2-5.

23. Lu, K.; He, C.; Lin, W. A Chlorin-Based Nanoscale MetalOrganic Framework for Photodynamic Therapy of Colon Cancers. J. Am. Chem. Soc. 2015, 137 (24), 7600-7603.

24. Toufektsian, M.; Boucher, F.; Tanguy, S.; Morel, S.; Leiris, J. Cardiac Toxicity of Singlet Oxygen: Implication in Reperfusion Injury. Antioxid. Redox Signaling 2001, 3 (1), 63-69.

25. DeRosa, M. C.; Crutchley, R. J. Photosensitized Singlet Oxygen and Its Applications. Coord.Chem.Rev.2002,233-234,351-371.

26. Jarvi, M. T.; Niedre, M. J.; Patterson, M. S.; Wilson, B. C. Singlet Oxygen Luminescence Dosimetry (SOLD) for Photodynamic Therapy: Current Status, Challenges and Future Prospects.Photochem.Photobiol.2006,82,1198-1210.

27. Bonnett, R. Photosensitizers of the Porphyrin and Phthalocyanine Series for PhotodynamicTherapy.Chem.Soc.Rev.1995,24(1),19-33.

28. Courtney, C. M.; Goodman, S. M.; McDaniel, J. A.; Madinger, N. E.; Chatterjee, A.; Nagpal, P. Photoexcited Quantum Dots for Killing Multidrug-Resistant Bacteria. Nat. Mater.2016,15(5),529-534.

29. Choi, H. S.; Liu, W.; Misra, P.; Tanaka, E.; Zimmer, J. P.; Ipe, B. I.; Bawendi, M. G.; Frangioni, J. V. Renal Clearance of Quantum Dots. Nat. Biotechnol. 2007, 25 (10), 1165-1170.

30. Chan, W. C. W.; Nie, S. Quantum Dot Bioconjugates for Ultrasensitive Nonisotopic Detection.Science1998,281,2016-2018.

31. Farokhzad, O. C.; Karp, J. M.; Langer, R. Nanoparticle- aptamer Bioconjugates for Cancer Targeting. Expert Opin. Drug Delivery 2006, 3 (3), 311-324.

32. Ipe, B. I.; Lehnig, M.; Niemeyer, C. M. On the Generation of Free Radical Species from QuantumDots.Small2005,1(7),706-709.

33. Harbour, J. R.; Hair, M. L. Superoxide Generation in the Photolysis of Aqueous Cadmium Sulfide Dispersions. Detection by Spin Trapping. J. Phys. Chem. 1977, 81 (18), 1791-1793.

34. Buettner, G. R.; Mason, R. P. Spin-Trapping Methods for Detecting Superoxide and Hydroxyl Free Radicals in Vitro and in Vivo. Methods Enzymol. 1990, 186 (4), 127-133.

35. Imlay, J. A. Pathways of Oxidative Damage. Annu. Rev. Microbiol. 2003, 57 (1), 395-418.

36. Imlay, J. A.; Linn, S.; Imlay, J. A.; Linn, S. Science 2016, 240 (4857), 1302-1309.

37. Nakamura, J.; Purvis, E. R.; Swenberg, J. A. Micromolar Concentrations of Hydrogen Peroxide Induce Oxidative DNA Lesions More Efficiently than Millimolar Concentrations in Mammalian Cells. Nucleic Acids Res. 2003, 31 (6), 1790-1795.

38. Li, C.-Q.; Pang, B.; Kiziltepe, T.; Trudel, L. J.; Engelward, B. P.; Dedon, P. C.; Wogan, G. N. Threshold Effects of Nitric OxideInduced Toxicity and Cellular Responses in Wild-Type and p53-Null Human Lymphoblastoid Cells. Chem. Res. Toxicol. 2006, 19 (3), 399-406.

39. Courtney, C. M.; Goodman, S.; Nagy, T.; Levy, M.; Bhusal, P.; Madinger, N. E.; Detweiler, C.; Nagpal, P.; Chatterjee, A. Potentiating Clinical Drug Resistant Bacteria via Stimuli-Activated Superoxide Generation. Sci. Adv. 2017, 3 (10), e1701776.

40. Finkelstein, E. L. I. D.; Surgery, R. G.; Rosen, O. D. M.; Durham, R.; Carolina, N. Production of hydroxyl radical by decomposition of superoxide spin-trapped adducts. Mol.Pharmacol.1982,262-265.

41. Goodman, S. M.; Levy, M.; Li, F.-F.; Ding, Y.; Courtney, C. M.; Chowdhury, P. P.; Erbse, A.; Chatterjee, A.; Nagpal, P. Designing Superoxide-Generating Quantum Dots for Selective Light-Activated Nanotherapy. Front. Chem. 2018, 6 (46), 1-12.

42. Yamazaki, I.; Piette, L.; Grover, T. A. Kinetic Studies on Spin Trapping of Superoxide and Hydroxyl Radicals Generated Reductase Paraquat Systems. J. Biol. Chem. 1990, 265 (2), 652-659.

43. Imlay, J. A. The Molecular Mechanisms and Physiological Consequences of Oxidative Stress: Lessons from a Model Bacterium. Nat. Rev. Microbiol. 2013, 11 (7), 443-454.

44. Imlay, J. A. Iron-Sulphur Clusters and the Problem with Oxygen. Mol. Microbiol. 2006, 59(4),1073-1082.

45. Cabelli, D.; Bielski, B. H. J. Kinetics and Mechanism for the Oxidation of Ascorbic Acid/Ascorbate by HO2/O2- Radicals. J. Phys. Chem. 1983, 87, 1809-1812.

46. Mizuno, M.; Nishitani, Y. Scavenging Rate Constants of Hydrophilic Antioxidants against Multiple Reactive Oxygen Species. J. Clin. Biochem. Nutr. 2013, 52 (May), 202-207.

47. Sato, Y.; Itagaki, S.; Kurokawa, T.; Ogura, J.; Kobayashi, M.; Hirano, T.; Sugawara, M.; Iseki, K. In Vitro and in Vivo Antioxidant Properties of Chlorogenic Acid and Caffeic Acid.Int.J.Pharm.2011,403(1-2),136-138.

48. Buxton, G. V.; Greenstock, C. L.; Helman, W. P.; Ross, A. B. Critical Review of Rate Constants for Reactions of Hydrated Electrons, Hydrogen Atoms and Hydroxyl Radicals (·OH/·O- In Aqueous Solution. J. Phys. Chem. Ref. Data 1988, 17 (2), 513-886.

49. Sawyer, D. T.; Valentine, J. S. How Super Is Superoxide? Acc. Chem. Res. 1981, 14 (12), 393-400.

50. Sawyer, D. T.; Valentine, J. S. How Innocuous Is Superoxide? Comments. Acc. Chem. Res.1982,15(7),200.

51. Fridovich, I. How Innocuous Is Superoxide? Comments. Acc. Chem. Res. 1982, 15 (7), 200.

52. Carlioz, A; Touati, D. Isolation of Superoxide Dismutase Mutants in Escherichia Coli: Is Superoxide Dismutase Necessary for Aerobic Life? EMBO J. 1986, 5 (3), 623-630.

53. Iglewski, B.; Clark, V. Molecular Basis of Bacterial Pathogenesis; 1990.

54. Pan, X.; Yang, Y.; Zhang, J.-R. Molecular Basis of Host Specificity in Human Pathogenic Bacteria. Emerging Microbes Infect. 2014, 3 (3), e23.

55. Lancaster, J. R. Nitric Oxide: Principles and Actions; 1996.

56. Imlay, J. A.; Fridovich, I. Assay of Metabolic Superoxide Production in Escherichia Coli. J. Biol. Chem. 1991, 266 (11), 6957- 6965.

57. Winterbourn, C. C. Reconciling the Chemistry and Biology of Reactive Oxygen Species. Nat.Chem.Biol.2008,4(5),278-286.

58. Krumova, K.; Cosa, G. Chapter I: Overview of Reactive Oxygen Species. Singlet Oxyg. Appl.Biosci.Nanosci.2016,1(1),1-21.

59. Skovsen, E.; Snyder, J. W.; Lambert, J. D. C.; Ogilby, P. R. J. Phys. Chem. B 2005, 109, 8570-8573.

60. Ragas, X.; Agut, M.; Nonell, S. Singlet Oxygen in Escherichia` Coli: New Insights for Antimicrobial Photodynamic Therapy. Free Radical Biol. Med. 2010, 49 (5), 770-776.

61. Gort, A. S.; Imlay, J. A. Balance between Endogenous Superoxide Stress and Antioxidant Defenses. J. Bacteriol. 1998, 180 (6), 1402-1410.

Chapter 3

Improving the stability and efficacy of Quantum Dots for Selective Light-Activated Nano therapy

Reproduced with permission from Samuel M. Goodman, Max Levy, Fei-Fei Li ,Yuchen Ding , Colleen M. Courtney , <u>Partha P. Chowdhury</u> , Annette Erbse , Anushree Chatterjee 1 and Prashant Nagpal, Designing Superoxide-Generating Quantum Dots for Selective Light-Activated Nanotherapy *Front. Chem.* **2018**, *6* (46), 1– 12. Copyright 2018 Frontiers Media SA

Introduction

Antibiotics have been a cornerstone of modern medicine, where molecules like β-lactams are an important and frequently used class. However, the rapid emergence of bacteria that release β-lactamases, and more recently metallo-β-lactamases such as NDM-1, have further proliferated the rise of drug resistance in Enterobacteriaceae, amounting to a major public health concern (Pitout and Laupland, 2008). The increased necessity to address the rise of multi-drug resistance (MDR) in these gram-negative pathogens was highlighted by the first-ever classification of carbapenem-resistant Enterobacteriaceae as a critical classI pathogen by the World Health Organization (2018). There is an urgent need for the development of novel antibiotics to specifically target the significant increase in MDR bacterial outbreaks, and nanotherapeutics offer an alternative due to their stability, ease of delivery, and facile transport through cell walls. Three different classes of light-activated nanoscale therapeutics have been proposed: metal-nanoparticle induced photothermal therapy (Hirsch et al., 2003; Connor et al., 2005; Huang et al., 2006), small photosensitizing molecules induced photodynamic therapy

(Dai et al., 2010; Hamblin and Hasan, 2014), and quantum dot (QD)-based selective-redox (Courtney et al., 2016, 2017; Reynolds et al., 2017), therapies. While non-selective heating of surrounding medium and indiscriminate cell killing by metal nanoparticles reduces their suitability as an antibiotic, lack of tunability or control over the specific reactive oxygen species (ROS) generated by photodynamic therapies, such as nonselective singlet oxygen (Bonnett, 1995; Jarvi et al., 2006; Ma et al., 2008; Gomes et al., 2011; Hamblin and Hasan, 2014), reduces its appeal as a precision therapeutic approach. QDs are colloidal semiconducting nanoparticles with easily tunable optical and electronic properties and have been extensively studied for applications in bio-imaging (Gao et al., 2004; Medintz et al., 2005; Michalet et al., 2005; Gomes et al., 2011). By tuning shape- and size-dependent energies of photoexcited charge carriers in QDs via modulation of their conduction band (CB) and valence band (VB) positions, selective perturbation of redox homeostasis in a cellular environment outlines their selectivity as light-activated therapeutics (Courtney et al., 2016, 2017; Reynolds et al., 2017). More specifically, superoxide-generating QDs have recently been shown as a two-pronged strategy for combating superbugs: first, as therapeutics to selectively eliminate MDR bacteria (Courtney et al., 2016), and second, by potentiating existing pipeline of antibiotics which are nominally ineffective against these potent pathogens (Courtney et al., 2017). Specific generation of superoxide radical ($O_2^{\bullet-}$), one of the species characterized as ROS, requires an electron to be donated to an adsorbed oxygen molecules. While several other ROS species such as singlet oxygen and hydroxyl radicals are indiscriminate in their action and reactivity, the impact of superoxide mainly affects critical intracellular targets such as iron-sulfur clusters. Because of limited reactivity of superoxide with cellular targets, superoxide dismutase generated by cells tightly regulates the intracellular redox environment during the normal cellular function. This provides

an important opportunity for a precision therapeutic that can selectively generate superoxide at nanomolar doses intracellularly, perhaps controlled by an external stimulus like light, and such exogenous superoxide generation can lead to growth inhibition and cell death (Yu, 1994; Thannickal and Fanburg, 2000; Apel and Hirt, 2004; Valko et al., 2007; Imlay, 2013)

Results and Discussions

QD material and size

QDs offer unique advantages for developing this class of redox selective nanotherapeutics, by offering specific control over redox species generation. Nanoscale material and morphology can be modified to tailor the position of the quantum-confined oxidation and reduction potentials. Furthermore, such a strategy can be effective in developing a tunable class of therapeutics for a wide variety of diseases (Trachootham et al., 2009; Wondrak, 2009). For the specific class of superoxide-generating therapeutic against MDR superbugs, we developed cadmium telluride (CdTe) nanoparticles with a band gap of 2.4 eV (CdTe- 2.4)—corresponding to a diameter of 2.7–3.0 nm (**Figure 1A**). CdTe-2.4 QDs have a CB position at -0.5V on the NHE scale, allowing direct charge injection of photogenerated electrons to adsorbed oxygen on the surface–yielding superoxide radicals (inset, **Figure 1A**). This was verified by electrochemical cyclic voltammetry studies in the presence and absence of dissolved oxygen (**Figure 1B**). Furthermore, this 2.4eV bandgap allows the QDs to be strongly activated for therapy by visible light with modest penetration through the human skin (Courtney et al., 2017). We tested photoactivated CdTe-2.4, at concentrations well below the toxic threshold for mammalian cells (Courtney et al., 2016) by tracking the time-dependent optical density (OD) as a measure of bacterial growth. We observed that once exposed to light

with energy greater than the nanoparticle bandgap, there is a strong attenuation in the bacterial growth (**Figure 1C**). This was a clear consequence of light activation since cultures exposed to the same low concentrations of QDs without exposure to light were able to grow well (**Figure 1C**). To quantify the extent of bacterial growth inhibition with this light-activated treatment, we compared the OD of the treated bacterial culture at a time-point relative to the OD at time $t = 0$ ($\Delta OD_{x, T}$), with those receiving no treatment ($\Delta OD_{x,NT}$).

$$I_{P} = 1 - (\Delta OD_{L,T} / \Delta OD_{L,NT})$$

This photo-inhibition (*IP*) increases with higher QD concentrations (**Figure 1D**) while maintaining the same light intensity, due to stronger light absorption and a larger number of photogenerated intracellular superoxide species. Since the two-fold and four-fold increase in nominal QD dosage increases the intracellular QD concentration and hence superoxide concentration, a similar increase in therapeutic effect can be obtained by improving the uptake of CdTe-2.4 QDs inside cells while keeping the same dosage of QDs, we tuned the surface charge of ligands to modulate cellular uptake.
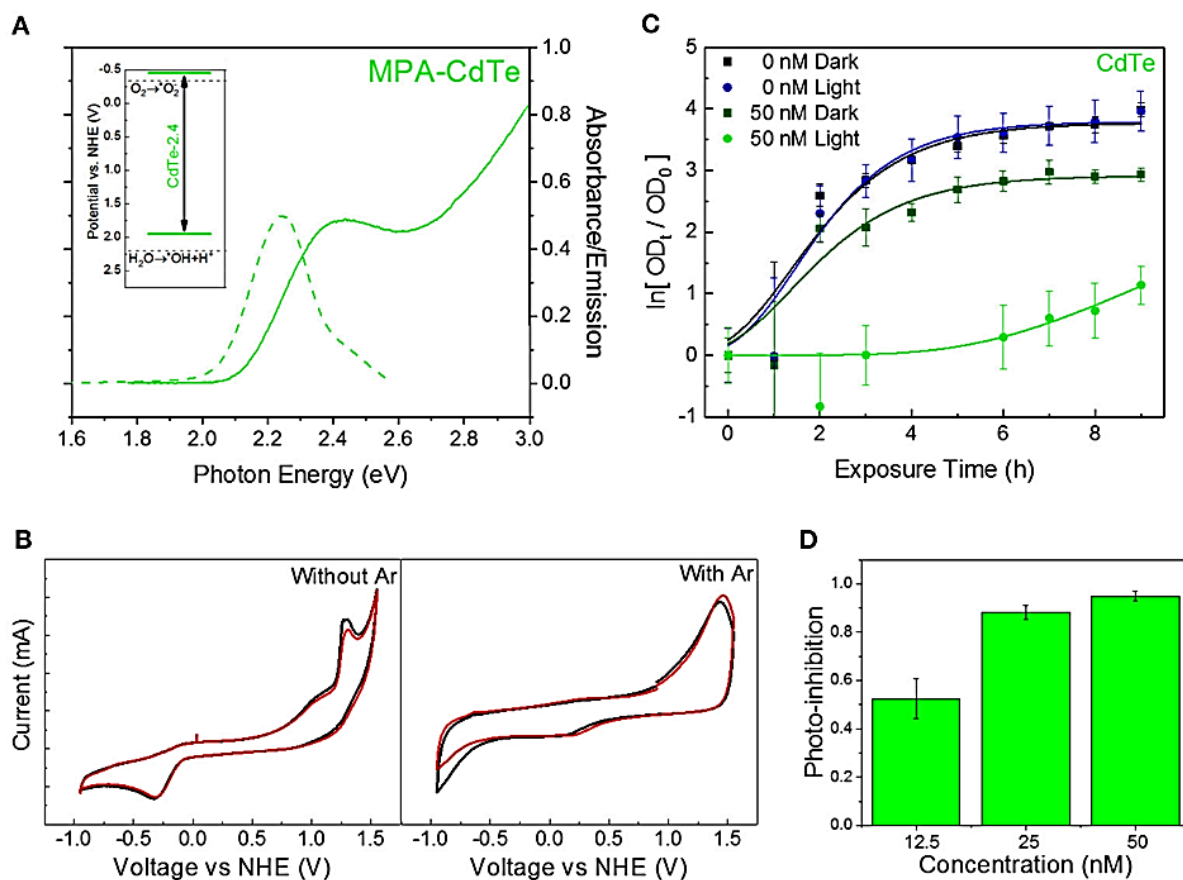
FIGURE 1 | Choice of QD core material and size for superoxide generation. (A) Absorbance (solid curve) and PL emission (dashed curve) spectra for CdTe-2.4. Inset shows band positions on NHE scale. (B) Cyclic voltammetry measurements for CdTe suspensions in PBS before (left) and after (right) bubbling with argon to remove dissolved oxygen. (C) Normalized optical density growth curves of *E. coli* with and without CdTe-2.4 core treatment in light and dark. Solid lines were added by fitting the data to a version of the Gompertz function. (D) Photo-inhibition as a function of QD concentration. Data shown in C, D is an average of three biological replicates and error bars denote standard deviation.

Ligand Selection

We engineered the QD surface charge by using three different QD ligands with CdTe-2.4 QDs: positively-charged cysteamine ligand-coated QDs (CA-CdTe), negatively-charged mercaptopropionic ligand-coated QDs (MPA-CdTe), and zwitterionic cysteine coated QDs (Cys-CdTe), as shown in **Figure 2A** and Figure S1. To observe only charge related effects, all ligands had similar sizes and used the same thiol group attachment to the Cd-rich facets on the CdTe QD surface. At the other end, a deprotonated carboxylic acid group and/or amine group provided enough electrostatic repulsion to yield colloidal stability in water. The charge on the surface of nanoparticles can have an important influence on their cellular uptake through the predominantly negatively charged lipid bilayers (especially for MDR gram-negative bacteria studied here) (Lovric et al., 2005 ´). To monitor the effect of QD surface charge on cellular uptake and consequent bacterial inhibition, we grew bacterial cultures in the presence of positively-charged CA-CdTe and zwitterionic Cys-CdTe QDs (both with 2.4 eV bandgaps) and compared the results with MPA coated CdTe-2.4. Bacterial growth in the presence of positively-charged QDs (CdTe-CA) exhibit much greater dark toxicity than their negatively-charged and zwitterionic counterparts (**Figures 2B,C**). While positively charged CdTe QDs show more than two-fold increase in cellular uptake compared to MPA and cysteine coated QDs (**Figure 2D**), at concentrations of 12.5 nM, there is no measurable cell growth even after 9 h, when inhibition in both light and dark approach the maximum value of 1. The increased toxicity of using positively-charged ligands has also been reported for other nanoparticles in both Gram-positive and Gram-negative bacteria (Nagy et al., 2012; Feng et al., 2015). This indiscriminate toxicity can be caused due to the strong attachment of the positively charged QDs to the cellular membrane, negatively charged DNA, RNA, proteins thereby inhibiting key

cellular functions leading to cell death. While such indiscriminate cellular killing makes a positively charged ligand unsuitable for selective therapy, the zwitterionic ligands significantly reduce such interactions in biological media, as measured by the hydrodynamic radius, when compared to charged ligands (Choi et al., 2007). The zwitterionic Cys-CdTe showed similar uptake to MPA-CdTe. Zwitterionic ligands have been shown to dramatically increase clearance of QDs from living systems by reducing the hydrodynamic radius (Choi et al., 2007). Taken together with the results showing similar stability and therapeutic effect to MPA-CdTe, we concluded that cysteine would be the optimal choice of ligand for QD design.
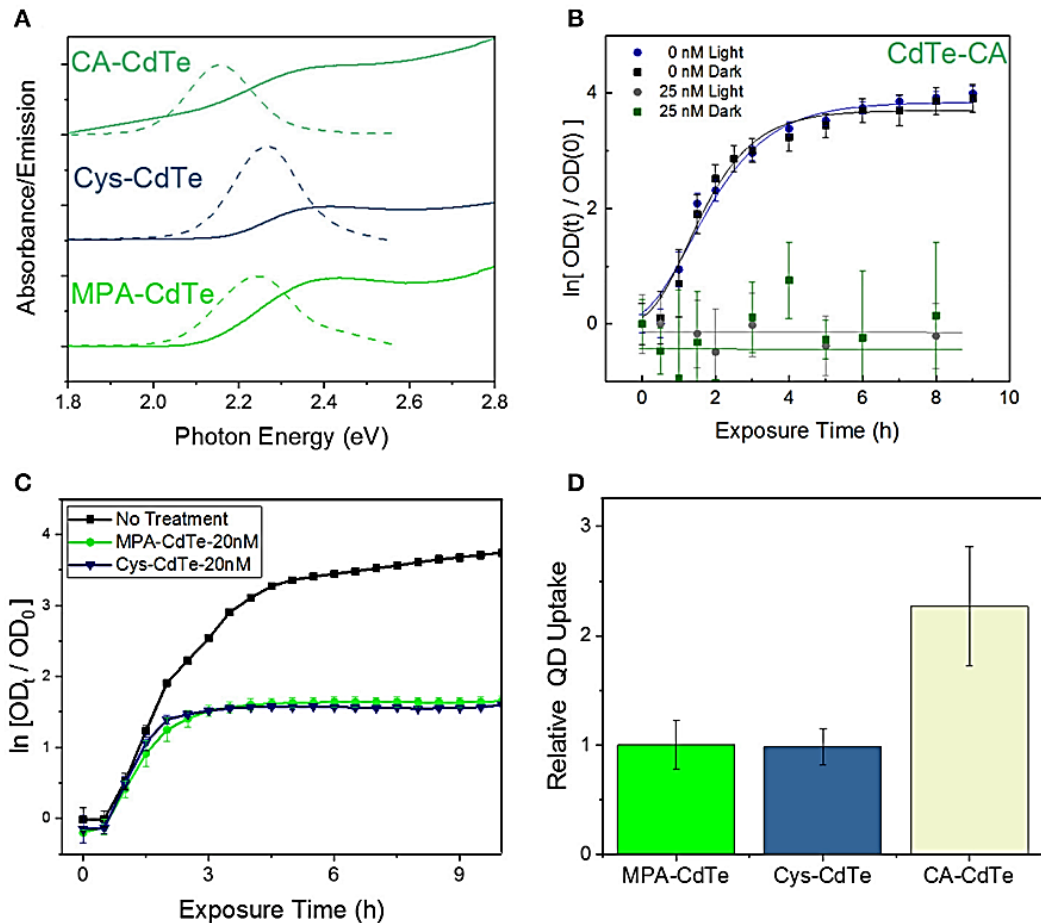
FIGURE 2 | Design of QD ligand and surface charge. (A) Optical properties of CdTe QDs coated with MPA, Cys, and CA. (B) Optical density (OD) growth curves of *E. coli* normalized

to time $t = 0$ exposed to CA-CdTe in light and dark. (C) Optical density growth curves of *E. coli* normalized to time $t = 0$ exposed to Cys-CdTe and MPA-CdTe in light. (D) Uptake of the MPA, CA, Cys coated QDs into *E. coli*. Data shown in (B–D) is an average of three biological replicates and error bars denote standard deviation.

Core-Shell QDs

One of the limitations of the light-activated therapy is the limited length of time that the particles are active (4–6 h) after which surface oxidation leads to vanishingly small therapeutic action (Dumas et al., 2010). To quantify the degradation kinetics, an experiment was conducted where the absorbance and emission spectra of CdTe cores were measured over time in phosphate buffered saline (PBS) with and without light exposure. Using the photoluminescence spectra (**Figure 3A**), there is a clear attenuation in signal intensity over time during illumination. Additionally, results show significant shifts in the peak position and an increase in the peak full-width at half maximum—all of which are representative of surface oxidation in a biological media (Schneider et al., 2009). Tracking the position of the emission peak reveals different regimes of particle degradation (**Figure 3B**). Starting from the initial state (α) there is a regime of general red-shifting (β) which lasts until hours 4 and 6 in light and dark, respectively. This behavior, which has previously been observed *in vitro* (Lu et al., 2008), likely corresponds to the creation of oxygen defects on the nanoparticle surface, which act as lower energy recombination centers. Long duration X-ray photoelectron spectroscopy (XPS) studies of bulk CdTe exposed to aqueous environments report an oxygen-rich surface, consisting primarily of CdO and TeO_2 (Zeng et al., 2015). After the maximum redshift there is a rapid blue-shifting regime (γ) which indicates that the diameter of the emissive CdTe core is

steadily shrinking as CdO and TeO_2 form. This regime experiences the largest reduction in luminescence intensity. By hour 7, no emission was detectable in the light-exposed sample, indicating that the oxidized shell makes non-radiative recombination the kinetically favored relaxation pathway for photogenerated charges. While the change in photoluminescence intensity may indicate that fewer photoexcited charge carriers are available for charge injection, the main result of the degradation is the shifting of redox potentials and the inclusion of a charge injection barrier against interaction with the external medium. Therefore, we evaluated different surface treatment methods to increase the QD stability while retaining the light-activated antimicrobial action.

A method of increasing the stability of QDs is to use a thin shell of a more stable material around the core. Such core-shell QDs have been used for fluorescent labeling, employing a type-I semiconductor heterostructure between an emissive CdX core enveloped in a thin shell of ZnS (CdX/ZnS) which protects the emission and decreases the toxicity (Kirchner et al., 2005; Chan et al., 2006; Cho et al., 2007). For therapeutic applications, the added stability from thicker shells is offset by an increased tunneling barrier for moving photogenerated charges from the core material to the adsorbate on QD surface (Ipe et al., 2005), thereby reducing the generation of light-activated redox species. There is also the potential effect of different adsorbate-binding affinities between the core and shell material, which can impact the therapeutic effect. Therefore, to minimize any negative impacts on the therapeutic action, we investigated CdTe/ZnS core-shell QDs with sub-monolayer thick shells. ZnS shell deposition was identified spectroscopically by characteristic changes in the absorbance spectra and red shifting emission with increasing shell thickness (Tsay et al., 2004; **Figure 3C**). Although the shell formation does not have a strong impact on the fluorescence quantum yield (QY) in

relation to the cores alone, characterizing the degradation kinetics of the CdTe/ZnS core-shell reveals different regimes of changes and a greater innate stability than the cores (**Figure 3D**). There is an initial regime of slowly blue-shifting emission (δ). This effect is transient, and a subsequent red-shifting is observed, as seen in the cores (ϵ), followed by a rapid blue-shift and collapse of the emission intensity (η). These core-shell QDs also show enhanced stability in dark, and the very small blue-shifting observed may be due to the UV light used to test the emission.

Testing the phototherapeutic effect of these stable core-shell CdTe/ZnS QDs reveals a light-activated photo-toxic effect on *E. coli* and a concentration-dependent dark toxicity, in good agreement with previous observations (**Figures 3E, F**). There is, however, a decrease in the phototherapeutic effect, likely due to the shell material interfering with redox activity of these nanoparticles. This reduction in redox activity is reflected by the growth curves since these changes were not due to different levels of uptake between the cores and core-shell QDs (**Figure 3G**), despite the core-shell QDs being slightly larger than their uncoated counterparts (Figures S2–S4 in the ESI†). This indicates that, for this size regime, the main factor in cell uptake QD surface charge and not QD material. While the CdTe/ZnS core-shell QDs exhibit higher stability in the biological medium, they are less effective as therapeutics due to the reduction in redox activity and perturbation of the electronic structure at the hetero-interface.
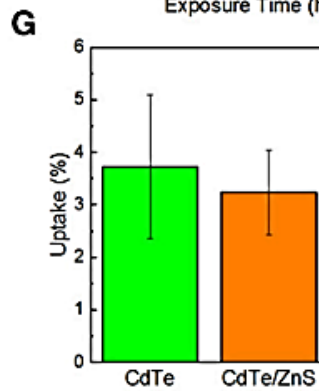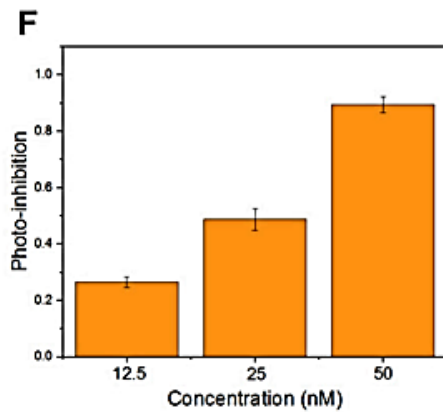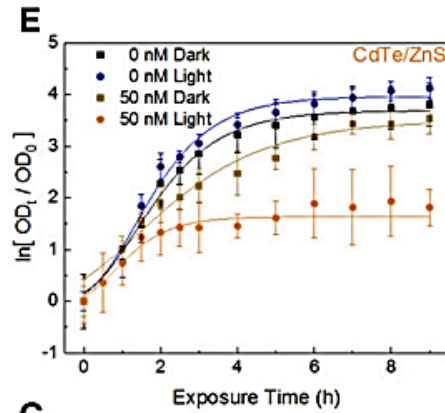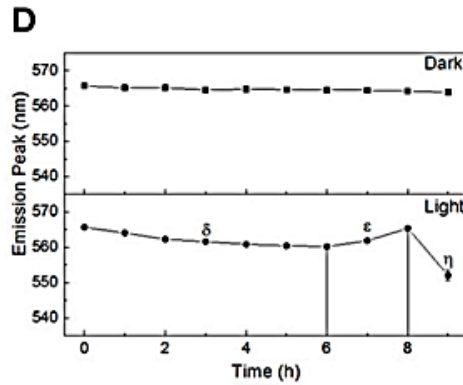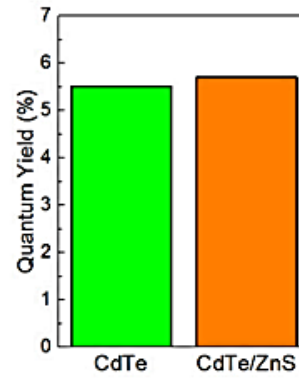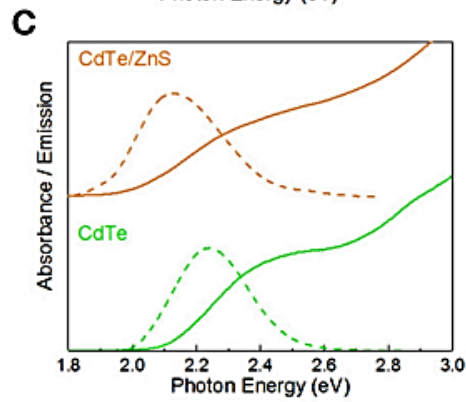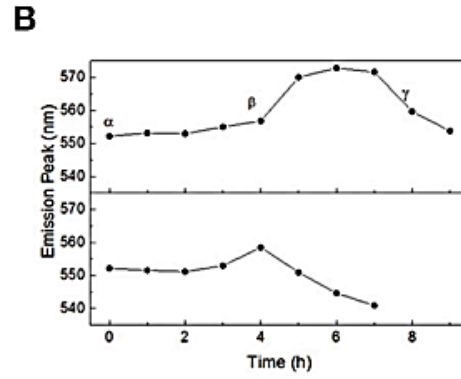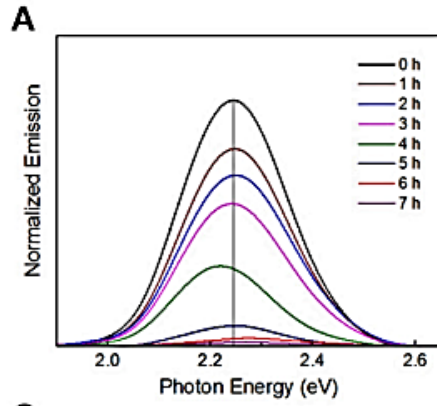
FIGURE 3 | Core-shell QDs for improved stability. (A) Normalized emission spectra of QDs over time in PBS during illumination, exhibiting decreased intensity, and shifts in the emission maxima. (B) Peak positions as a function of time, exhibiting different regimes of oxidation-instability. (C) Optical spectra and quantum yields of the CdTe cores and CdTe/ZnS core-shells. (D) Degradation profiles of CdTe/ZnS in PBS with and without illumination. (E) Normalized optical density growth curves (with respect to time $t = 0$) of *E. coli* exposed to the core-shells in light and dark. (F) Inhibition as a function of QD concentration. (G) Uptake of CdTe/ZnS core-shell QDs compared to CdTe cores. Data shown in (E–G) is an average of three biological replicates and error bars denote standard deviation.

Constituent Element Overcoat

An alternative to using a core-shell heterojunction for QD passivation is surface treatment by depositing more of the constituent elements on the surface to enhance stability. Depositing excess tellurium, or creating Te-rich facets on the surface, decreases QD stability and degrades the optical properties (Figure S5 in the ESI†). However, creating cadmium rich facets by treatment with excess $CdCl_2$ can increase the diameter slightly, thus decreasing the optical bandgap. In addition, the chemical and colloidal stability would likely increase due to the larger number of ligand binding sites (Katari et al., 1994). CdTe/Cd QDs were synthesized by combining CdTe cores (2 µM) with a mixture of CdCl2 and MPA in a 1:1 ratio, followed by reacting at 98◦C for 15 min. Elemental analysis of these particles indicates there is a 30% increase in cadmium content compared to the cores (0.6 MLE coverage), implying complete passivation of the tellurium facets. The reduction in defects is reflected by the increase in the photoluminescence QY of the cadmium overcoated nanoparticles (Glozman et al., 2001), which is over twice that of the untreated cores, while the slight redshift in absorbance confirms their larger size (**Figure 4A**). The cadmium overcoated samples consistently outperformed both the

cores and CdTe/ZnS core-shell QDs (**Figure 4B**). Unlike either, the CdTe/Cd QDs were still luminescent after 24 h of irradiation and underwent much slower rates of degradation during the first 9 h. The degradation curve also consists of the characteristic single monotonic phase of slow blue-shifting. These results also point to a potential application of these CdTe/Cd QDs for optical tracking and bio-imaging due to their apparent high QY and stability in biological media. As there are no exposed tellurium-rich facets to readily oxidize, degradation only involves CdO buildup on the surface followed by slow inward diffusion. In addition, minimal QD aggregation was observed during emission measurements, indicative of an increase in the number of bound capping ligands on the surface which predicts superior colloidal stability. When tested *in vitro*, the CdTe/Cd QDs induced a stronger photo-toxic effect than the CdTe/ZnS core-shell QDs, while the inherent-toxicity remained consistent within the measured concentration range (**Figures 4C, D**). As with the CdTe/ZnS core-shell QDs, there was also no observed difference in uptake between the CdTe/Cd and CdTe core nanoparticles (**Figure 4E**).
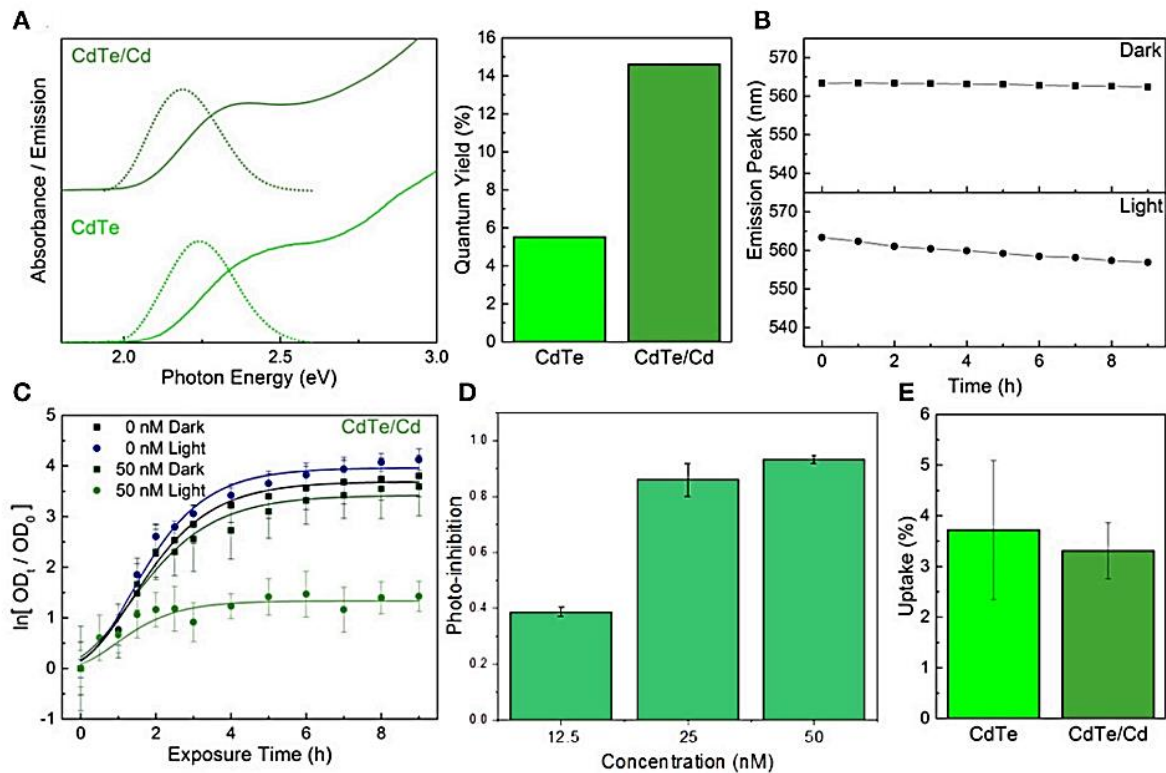
FIGURE 4 | Constituent element overcoat for improved stability and therapeutic effect. (A) Optical properties and fluorescence quantum yield of the CdTe/Cd particles compared to cores. (B) Emission peak changes during exposure to PBS in light and dark conditions of the core-shells. (C) Normalized optical density growth curves of *E. coli* exposed to CdTe/Cd. (D) Photo-inhibition as a function of QD concentration. (E) Uptake of the CdTe/Cd surface treated QDs compared to CdTe cores into *E. coli*. Data shown in C–E is an average of three biological replicates and error bars denote standard deviation.

Spectroscopic evaluation of QD design

Electrochemistry

Following light-activation, photogenerated charges in the QDs are transported to the surface near sites of adsorbed chemical species and are subsequently injected into the

adsorbate which forms the products of the photochemical process (**Figure 5A**). The kinetics of these photo redox processes and the resistance to each step can be characterized using electrochemical impedance spectroscopy (EIS). Using analysis of Bode and Nyquist plot, and an equivalent circuit diagram to obtain the solution resistance, resistance to charge injection to adsorbate (RCT), capacitance of the electrical double layer (CDL), and inherent resistance to charge transport and defect state density for the semiconductor QDs (**Figures 5B, C**). Comparing resistance to charge injection between CdTe core, CdTe/ZnS core-shell, and CdTe/Cd overcoated QDs, we observed that CdTe core QDs have the lowest resistance, as expected. CdTe/ZnS and CdTe/Cd were found to have 5- and 8-fold higher resistance to charge injection (**Table 1**).

TABLE 1 | Charge injection rate for photogenerated electrons (k), interfacial resistance to charge injection (RCT), and capacitance of double layer (due to charge trapping at the interface, CDL), measured using electrochemical impedance spectroscopy

	CdTe	CdTe/ZnS	CdTe/Cd
$k\ (\text{ms}^{-1})$	0.344 ± 0.001	0.317 ± 0.002	0.31 ± 0.01
			0.92 ± 0.05
$R_{CT}\ (\text{k}\Omega\cdot\text{cm}^2)$	1.02 ± 0.02	5.03 ± 0.01	8.74 ± 0.03
$C_{DL}\ (\mu\text{F}\cdot\text{cm}^{-2})$	73.4 ± 0.4	63.5 ± 0.2	35.0 ± 0.1

Also, while the double layer capacitance of CdTe cores and core-shell QDs was similar, the Cd overcoated QDs had lower capacitance, indicating easier transport of redox species even though the interfacial charge injection resistance is higher. This can likely be explained by a higher adsorption affinity of the chemical species (oxygen) on the cadmium-rich

surface. Further analysis of trapped charges and transport within the semiconductor QD did not reveal any appreciable differences.

To further probe the interfacial redox kinetics for therapeutic interventions, we also tracked the open circuit potential (OCP) decay in the respective QDs as a function of time (**Figure 5D**).The kinetics of OCP decay shows the overall photochemical process is faster in CdTe core QDs compared to the CdTe/ZnS core-shell QDs (**Figure 5C**).
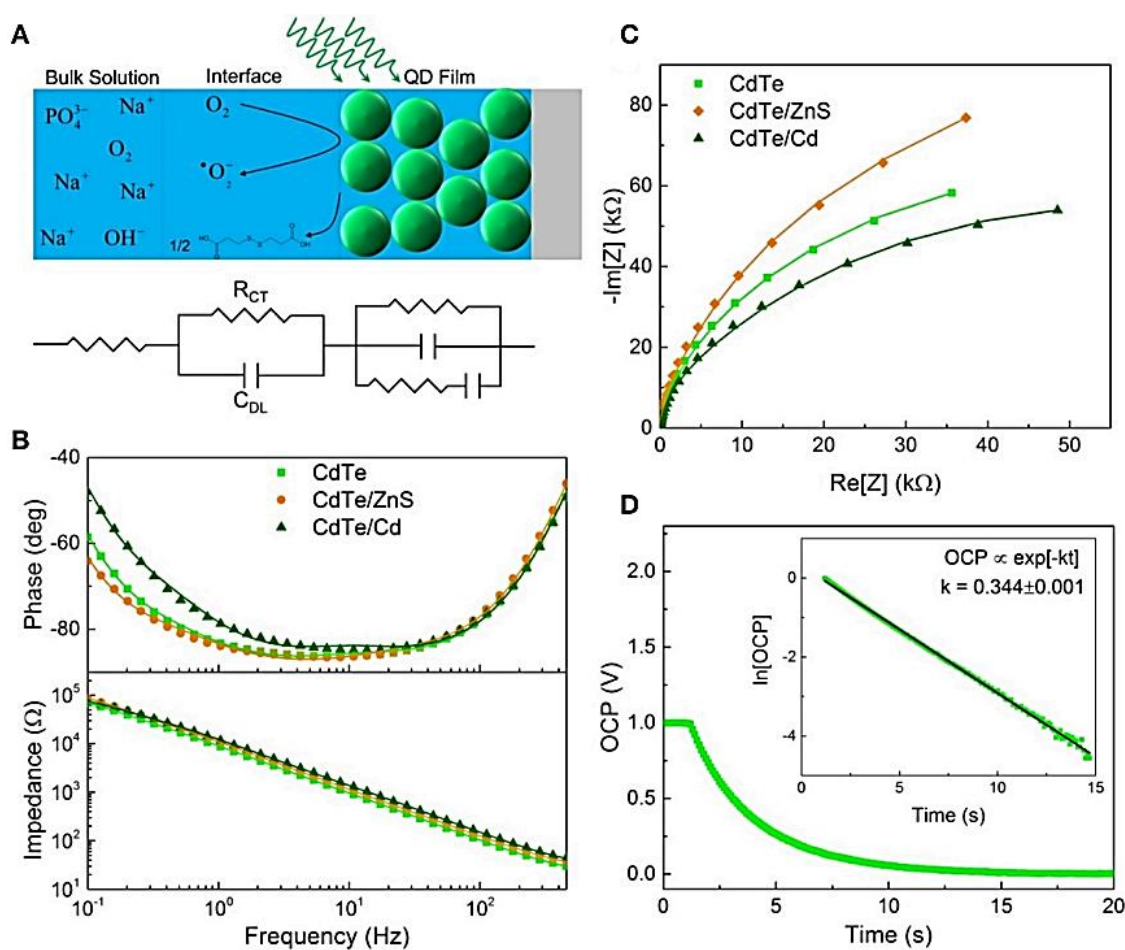
FIGURE 5 | Electrochemical characterization of QD design. (A) Schematic illustrating EIS measurement and equivalent circuit components for each part. (B) Bode and (C) Nyquist plots used to determine the interfacial parameters reported in Table 1. (D) Open circuit potential decay of the cores with the linearized plot used to extract the rate of charge injection inset.

This observation is consistent with the quantified ROS radical generation observed via quantitative measurements of these radical species via Electron Paramagnetic Resonance Spectroscopy (EPR, **Figure 6**) and phototherapeutic effect *in vitro*. In CdTe/Cd overcoated dots, we observed two modes of decay: one is the faster recombination between photogenerated charge carriers, and the second is the charge injection and photochemical generation of radical species. This observation explains the anomaly between higher QY and depressed ROS generation observed by EPR. While CdTe/Cd overcoated QDs improve the QY and have higher number of photogenerated charges for ROS radical formation, the increased resistance to charge injection leads to recombination (radiative and non-radiative) before they can be injected into the adsorbed oxygen to form superoxide radicals. Therefore, these measurements provide detailed insights and important design rules for making optimizing LARS production.
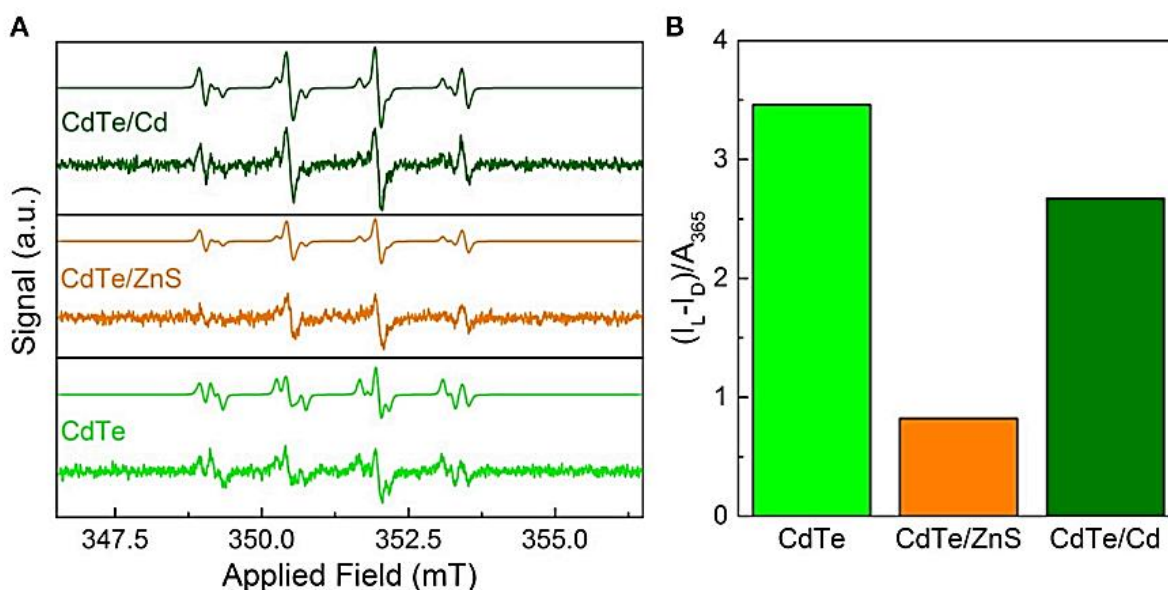
FIGURE 6 | Superoxide radical characterization via EPR for optimal QD design. (A) EPR spectra of the cores and core-shells before after 30 s of 365 nm irradiation with simulations based on a combination of hydroxyl- and superoxide-DMPO adducts. The dismutation of

superoxide radical generated by QDs leads to hydroxyl radical during EPR measurements (Courtney et al., 2017). (B) Integrated radical signal after dark subtraction (IL–ID) and normalization by the sample absorbance at the exciting wavelength.

EPR Spectroscopy

To probe the efficacy of phototherapeutic action in both cores and surface treated QDs (CdTe/ZnS core-shell QDs and CdTe/Cd overcoated QDs), we tested them using EPR spectroscopy. Previous studies have shown the formation of radicals upon light stimulation of nanoparticles (Ipe et al., 2005; Gao et al., 2014). These measurements were performed with the goal of identifying any short-lived radical species that are formed upon illumination using 5,5-dimethyl-pyrroline-N-oxide (DMPO) as a long-lived spin trap. The spectra of samples exposed to light show two components corresponding to DMPO adducts formed from hydroxyl and superoxide radicals (**Figure 6A**) (Finkelstein et al., 1980). This was confirmed by simulating the spectra as a combination of the two adducts using hyperfine coupling constants of $a_N =$ 14.90 G and $a_H{}^\beta = 14.93$ G for DMPO-OH and $a_N = 14.2$ G, $a_H{}^\beta = 11.4$ G, and $aH\gamma 1 = 1.2$ G for DMPO-OOH in good agreement with established characteristic hyperfine constants (Buettner, 1987). The presence of hydroxyl and superoxide radicals indicate ROS as the toxic mechanism. These features are consistent for the cores and both core-shell particles, indicating that neither the interfacial states in CdTe/ZnS nor the increased size of the CdTe/Cd alters the electronic structure sufficiently to change the mechanism. In dark, there was a minor signal originating from the DMPO hydroxyl radical adduct in each case, likely due to ambient light stimulation during sample preparation, during which completely light-free conditions were not possible. To further quantify the phototherapeutic effect observed, we measured the relative free-radical

production by each QD by integrating the EPR spectra and normalizing to the QD absorbance (**Figure 6B**). Our experiments clearly show that CdTe core QDs have significantly higher yield of ROS species compared to CdTe/ZnS core-shell QDs, which explains the observed difference in their respective phototherapy. The production from CdTe/Cd shows attenuation to a lesser degree. Together, these measurements provide valuable design rules for QD surface treatments towards nanotherapeutic applications, we conducted EIS investigations of the kinetics of redox generation in core and surface treated CdTe QDs.

In-vitro testing of QD design

We evaluated the therapeutic effect of optimal QD design, especially ligand selection and surface treatment, by *in vitro* testing and comparison between Cys-CdTe/Cd when compared to untreated MPA-CdTe (**Figures 7A,B**). In cell culture with light exposure, we found that desired phototoxic effect was consistent between the Cys-CdTe/Cd and MPA-CdTe. While phototoxicity of Cys-CdTe/Cd was like uncoated MPA-CdTe, their increased stability provides sustained therapeutic effect against pathogens. We also investigated the therapeutic efficacy of these stability-enhanced CdTe/Cd nanoparticles QDs in countering a WHO priority I MDR Enterobacteriaceae *Klebsiella pneumoniae* expressing New Delhi metallo-beta-lactamase 1 (NDM-1), an enzyme that resists a broad range of beta-lactam antibiotics including last-resort antibiotics such as carbapenems. This highlights the pandemic problem of drug-resistance and the need for novel antibiotics, and it served as an important test for our nano therapy. Low concentrations (50 nM) of CdTe/Cd nanoparticles were added to the growth media with these isolates, and the MDR strain grew well in dark (**Figure 7C**). Nevertheless, on light-activation, no growth was observed in these strains when measuring OD. To further probe the bactericidal effect of the CdTe/Cd nanotherapeutic using colony forming unit (CFU)

analysis. Our results show that while untreated strains grew more than 100-fold in 4–8 h, we saw > 90% reduction in 4 h and >99% killing of *K. pneumoniae* at 8 h, compared to the initial bacterial population at $t = 0$ h (**Figure 7D**). This highlights the efficacy of our nanotherapeutic against potent MDR clinical strains. Taken together, the stability, photo-toxicity, and uptake measurements clearly indicate that a Cd-overcoat is a better choice for the nanotherapeutic QDs than a ZnS shell or no surface treatment.
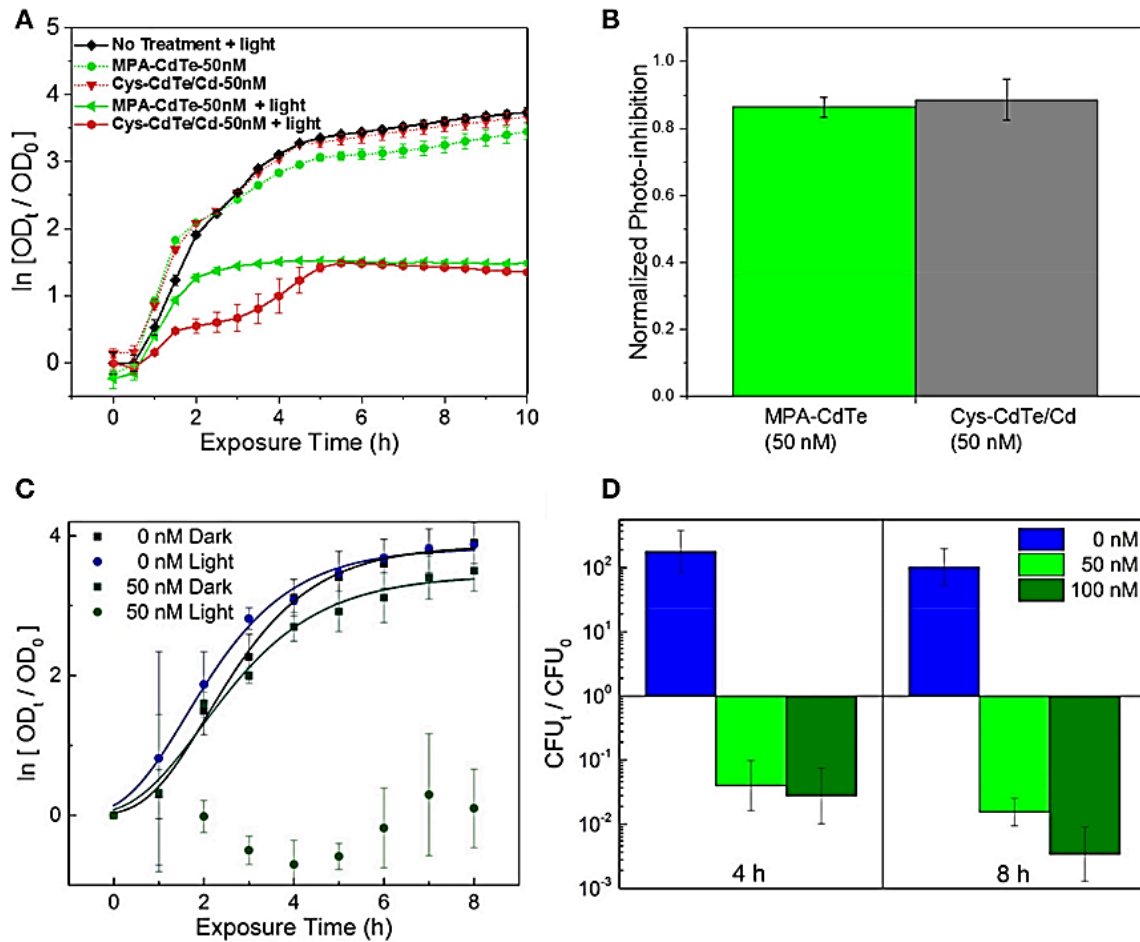
FIGURE 7 | Efficacy of optimal QD design in *in vitro* cultures. (A) Normalized optical density growth curves (with respect to time $t = 0$) of *E. coli* exposed to Cys-CdTe/Cd and MPA-CdTe. (B) Growth inhibition from rationally designed Cys-CdTe/Cd compared to MPA-CdTe. (C) Optical density growth curves of NDM-1 expressing *K. pneumoniae* exposed to CdTe/Cd in light and dark. (D) Colony forming unit (CFU) analysis of NDM-1 expressing *K. pneumoniae*

cultures at 4 and 8 h of light exposure with respect to CFU at time $t = 0$. Data in A–D represents average of three biological replicates and error bars denote standard deviation.

Conclusion

In conclusion, we have demonstrated the design of an effective QD-based selective-redox therapeutic, as well as the effect of different surface treatments on this QD light-activated nanotherapy. We showed that while different QD materials demonstrate different biocompatibility, the cellular uptake is primarily governed by the charge on the QD surface. Positively charged CA-coated CdTe QDs showed higher uptake by the cells compared with the negatively charged (MPA) and zwitterionic (Cys) CdTe QDs. While CdTe/ZnS core-shell QDs improve the chemical and colloidal stability of QDs in biologically relevant media, the enhanced resistance to charge injection for photoredox processes and changes in the interfacial electronic states makes them less attractive as candidates for antimicrobial applications. Using cationic over-coating with CdTe/Cd QDs we demonstrate higher stability and maintain phototherapeutic effect as the CdTe cores, makings them better candidates for those applications. We also tested these CdTe/Cd as therapeutic against a clinical isolate of *K. pneumoniae* expressing NDM- 1, which was resistant to β-lactams including carbapenem, and found that it killed more than 99% of the initial bacterial population in 8 h, indicating the potential for application of this nanotherapeutic. Finally, we showed that Cys-coated CdTe/Cd QDs offer improved chemical stability without inhibiting phototoxicity. Therefore, this study provides detailed physical insights into the mechanism and kinetics of QD nanotherapeutics

and provides important design rules for utilizing surface treatments to improve the stability and selective redox interventions using colloidal QDs.

Methods

Core Synthesis

CdTe cores were synthesized using the materials and methods described in our previous publication (Courtney et al., 2016). Briefly, a reaction mixture was made by mixing a stock solution of degassed $CdCl_2$ (0.4 mg/mL; Sigma) and MPA (1 mg/mL; Fischer) in DDW with additional degassed DDW in equal volumes (e.g., 500 µL Cd solution, 500 µL DDW), 0.5 M NaOH (volume: 2% of total), and a solution of NaHTe (40 mg/mL, volume: 0.2% of total). The reaction mixture was then split into 100 µL aliquots and heated to 98°C for 1.5 h in a thermocycler. The resulting QDs are sterile if autoclaved materials are used throughout. Before use in plate assays the QDs were first bulk centrifuged at 15 k rpm for 3 min to pellet unreacted starting material and poorly-passivated dots, and 200 µL of the QD stock was then filtered and washed twice with 100 µL of sterile pH 11 water in an ethanol sterilized 4K Nanosep filter (Pall)—5 min at 10 k rpm for each filtration and wash step, residual ethanol was removed prior by rinsing the filter with 100 µL pH 11 water. After the final wash, the dots were re-dispersed in pH 11 water and the concentration was determined using optical correlations (Yu et al., 2003). QDs were mixed with the relevant medium before integration with cells.

Cysteamine Ligand Exchange

A stock of cysteamine-hydrochloride (CA; Sigma) was created by dissolving CA (7.7 mg, 0.10 mmol) in 1 mL of pH 6 water. This was used to re-disperse CdTe-2.4 cores which were filtered and washed twice with double-distilled water (DDW). The QDs were then kept in the dark at room temperature overnight. Prior to use the particles were bulk-centrifuged at 10 k rpm for 5 min to remove poorly-passivated QDs and washed in a similar manner using PBS (Lovric et al., 2005 ´).

ZnS Core-Shell Synthesis

A stock 100X solution of zinc and sulfur sources was created by dissolving $Zn(NO_3)_2 \cdot 6H_2O$ (609 mg, 5.57 mmol; Sigma) and thiourea (75 mg, 1.0 mmol; Sigma) in 10 mL ddH2O. For a synthesis, 100 μL of the 100X stock was diluted into 10 mL of freshly de-gassed ddH2O which served as the zinc-sulfur precursor stock. 200 μL of CdTe-2.4 stock was filtered, washed twice and re-dispersed with pH 11 water. This solution was then diluted to 2 μM. The reaction solution consisted of the filtered QDs and the precursor stock in a 1:1 ratio, with 10 μL of 0.5 M NaOH per 500 μL of reaction volume. This mixture was then divided into 100 μL PCR tubes and reacted at 98∘C for 1 h. Prior to use in cell cultures, they were filtered and washed as previously described. Due to changes in the optical properties the absorbance after synthesis was used to calculate the extinction coefficient at 400 nm for the 1 μM stock, which was then used to calculate the concentrations post-filtering.

Cd-Overcoat Synthesis

A Cd-MPA stock was prepared and degassed as previously described for the core syntheses. 200 µL of CdTe-2.4 stock was filtered, washed twice, re-dispersed with pH 11 water, and then diluted to 2 µM. The QD and Cd-MPA stocks were mixed in equal volumes with 10 µL of 0.5 M NaOH per 500 µL of reaction volume. The reaction solution was then divided into 100 µL PCR tubes and reacted at 98°C for 15 min.

Synthesis Chemicals

3-Mercaptopropionic acid (≥99%) was purchased from Acros Organics. Cadmium(II) chloride (technical grade), ammonium fluoride (≥98%), and hexamethylenetetramine (≥99.0%) were purchased from Sigma Aldrich. Tellurium -325 mesh powder (99.99% metal basis) was purchased from Alfa Aesar. Sodium borohydride (98%), sodium hydroxide (≥97.0%), and ethylene glycol (certified) were purchased from Fisher Scientific. Compressed nitrogen (prepurified) and oxygen (ultrahigh purity) were purchased from Airgas. Ethanol (200 proof) was purchased from Decon Laboratories INC.

Culture Conditions

Colonies of *E. coli* (MG1655) were grown on solid Luria Bertani (LB, Sigma Aldrich)-agar media overnight at 37∘C from freezer stocks (40% glycerol, -80∘C) and stored at 4∘C. For a microplate assay, three individual colonies were grown overnight in LB and diluted 1:100 when incorporated with the various QDs in fresh media. Separate 96-well flat-bottom plates were prepared for light and dark conditions, the OD of which was measured using a Tecan GENios at 562 nm. Plates were shaken at 225 rpm in a 37∘C incubator between

measurements. The dark plate was wrapped in aluminum foil while the edge of the light plate was sealed with parafilm to reduce evaporation. The light source was modulated before each experiment to provide the desired intensity and was equipped with a 400 nm longpass filter (ThorLabs FGL400) and a 350-700 nm bandpass filter (FGS900-A) to remove UV and IR light. The fits were done using Gompertz function, with growth rate (μ), stationary phase population (S) and λ is the lag time: (Zwietering et al., 1990).

$$\ln \left(\frac{OD_t}{OD_0} \right) = S \cdot \exp \left\{ - \exp \left[\frac{\mu \cdot \exp(1)}{S} (\lambda - t) + 1 \right] \right\} \quad (2)$$

Nanoparticle Characterization

All absorbance measurements were obtained with a VWR UV-1600PC spectrometer at 1 nm resolution. Quantum yields (QY) were determined via comparison with a fluorescein isothiocyanate (FITC, Sigma) standard using a NIST calibrated Photon Technologies International fluorimeter for each sample, with emission measured from 485 to 800 nm using 475 nm excitation. Each QY was calculated using Equation (3) (Grabolle et al., 2009). High-resolution transmission electron micrographs (Figures S4, S5) were obtained in the CAMCOR facility at the University of Oregon, and with a Philips CM 100 at 80 kV. Cores exhibited an average diameter of 2.9 ± 0.3 nm, with the core-shells being slightly larger with CdTe/ZnS and CdTe/Cd averaging 3.2 ± 0.5 and 3.1 ± 0.5 nm, which matches the ICP observations of single monolayer-regime coverage.

$$\frac{\Phi_{QD}}{\Phi_{FITC}} = \frac{A_{FITC} \int_{485}^{800} I_{QD} \lambda d\lambda}{A_{QD} \int_{485}^{800} I_{FITC} \lambda d\lambda} \quad (3)$$

Degradation Studies

QDs were centrifuged and filtered in the same manner used to prepare stocks for biological assays. Two samples of each type were prepared in PBS to simulate a biologically relevant medium. One was kept in dark, while the other was illuminated using the same light intensity as the assays. Emission spectra were recorded using 365 nm excitation and a calibrated Ocean Optics USB4000 detector.

Uptake Studies

Three cultures were grown overnight and diluted 1:10 into PBS with the QDs at 100 nM total concentration. The cultures were then shaken for 1 h at 37∘C and collected into centrifuge tubes.The tubes were spun at 15 k rpm at 3 min and the supernatant was removed. The cell pellet was then washed twice with PBS and once with DDW using this procedure. The pellet was then dispersed in ~300 µL DDW for storage (final volume was recorded after dispersion). ICP-MS samples were prepared by diluting 25 µL of the samples to 1 mL total volume. Standards were prepared within the limits of the possible concentration range for comparison. This analysis provided the raw element composition of the samples, which was used to calculate the signal corresponding to specific concentrations. The monolayers-equivalent addition of Cd and Zn for the CdTe/ZnS and CdTe/Cd samples was calculated by translating the signal to the number of atoms in the core initially (calculated based on the measured core diameter using TEM) and adding the overcoated atoms to the surface and calculating that effective area relative to the initial surface area of the particles. The percentage uptake reported in the figure are defined using a mass balance comparing the total number of particles associated with the cells with the initial number introduced into the cultures.

EPR Spectroscopy

Nanoparticle samples were filtered and washed three times with pH 11 water and once with DDW before DMPO (Dojindo) was added (1 vol%) and were then kept in dark conditions as much as possible prior to measuring. Spectra were obtained on a Bruker Elexsys E 500 spectrometer with an SHQE cavity at 7 mW microwave intensity. Samples were loaded into four quartz capillaries for measurement. Samples were first measured in dark to provide a baseline signal, then were illuminated with 365 nm light for 30 s and immediately re-measured. Quantification of the radical products was accomplished by fitting the spectra to a sum of the theoretical spectra using the following hyperfine coupling constants to simulate each adduct. DMPO-OH: a_N = 14.90 G, $a_H{}^\beta$ = 14.93 G; DMPO-OOH: a_N = 14.2 G, $a_H{}^\beta$ = 11.4 G, $a_H{}^\gamma 1$ =1.2 G. Quantification was done by calculating the double integral of the fit spectrum and normalizing the resulting area by the sample absorbance at 365 nm.

EIS

Electrochemical Impedance Spectroscopy (EIS) was conducted using a Bio-logic SP-200 potentiostat/galvanostat. Using a three electrode (working electrode: CdTe NPs drop-casted thin film, counter electrode: platinum wire, reference electrode: Ag/AgCl) configuration, the experiments were conducted in a frequency range from 100 kHz to 100 mHz, with an amplitude of 10 mV AC polarization on open-circuit potential (OCP) vs. reference electrode. Bode plot and Nyquist plot were extracted from the measurements and fitted to the suggested equivalent circuit using the Z-fit function in EC-lab software (Bio-logic). Open circuit potential (OCP) decay/relaxation was conducted using the same three-electrode setup to evaluate the charge transfer characteristics on the QD-electrolyte surface. The measurements were first

taken in the dark until stable open-circuit potential was obtained followed by irradiating it with a 300 W xenon lamp. The irradiation was turned off once stable open-circuit potential was reached. The OCP decay curve was recorded until the OCP no longer changed.

Supplementary Figures
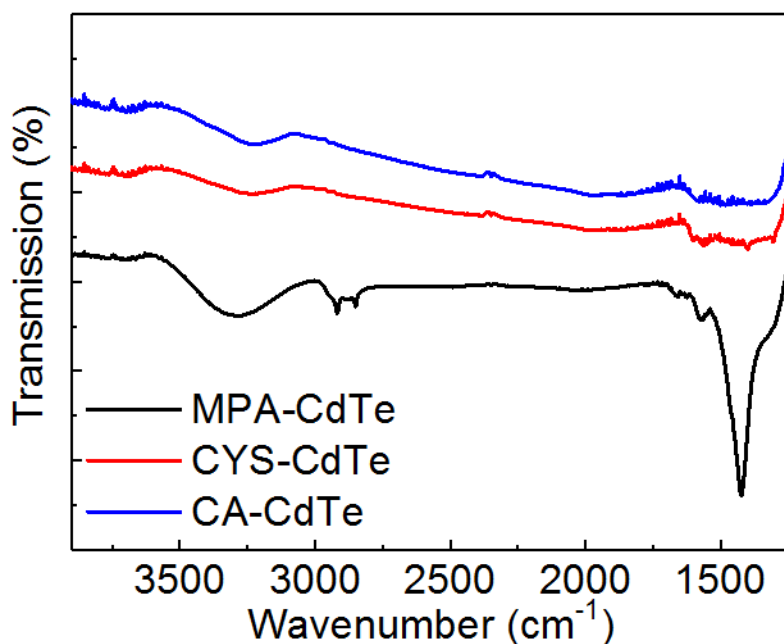
Figure S1 – Fourier-transform infrared spectroscopy measurements of CdTe with different organic ligands. MPA- and Cys-CdTe prepared as described in methods. CA-CdTe also prepared as described—with ligand exchange method starting from MPA-CdTe. Peak near 1500 cm^{-1} indicative of MPA attachment to QD surface. Broad peaks near 3200 cm^{-1} (and absence of MPA peaks) indicate appropriate cysteine and cysteamine attachment.
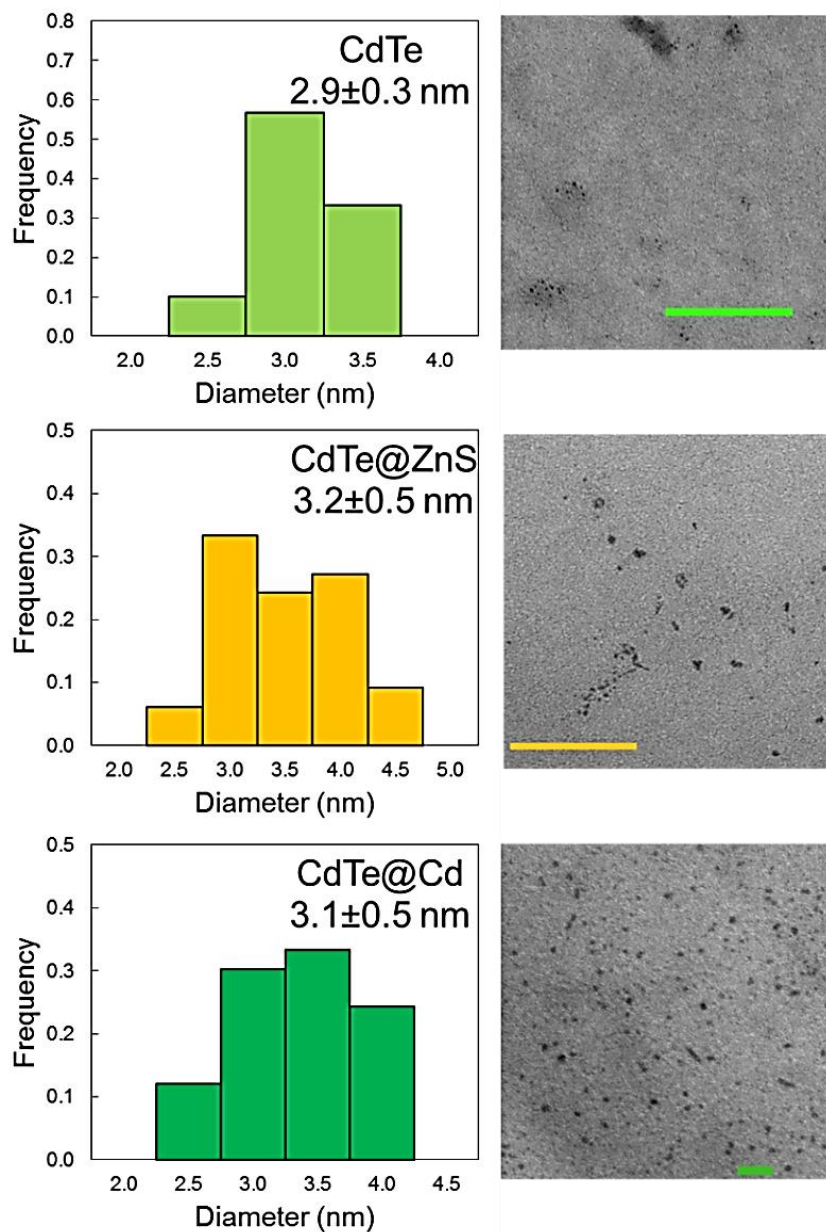
Figure S2 – TEM images and size distribution histograms of the core and core-shell particles. Distributions and average diameters are the result of the analysis of 30 particles. Scale bars are 100 nm for CdTe and CdTe@ZnS and 20 nm for CdTe@Cd
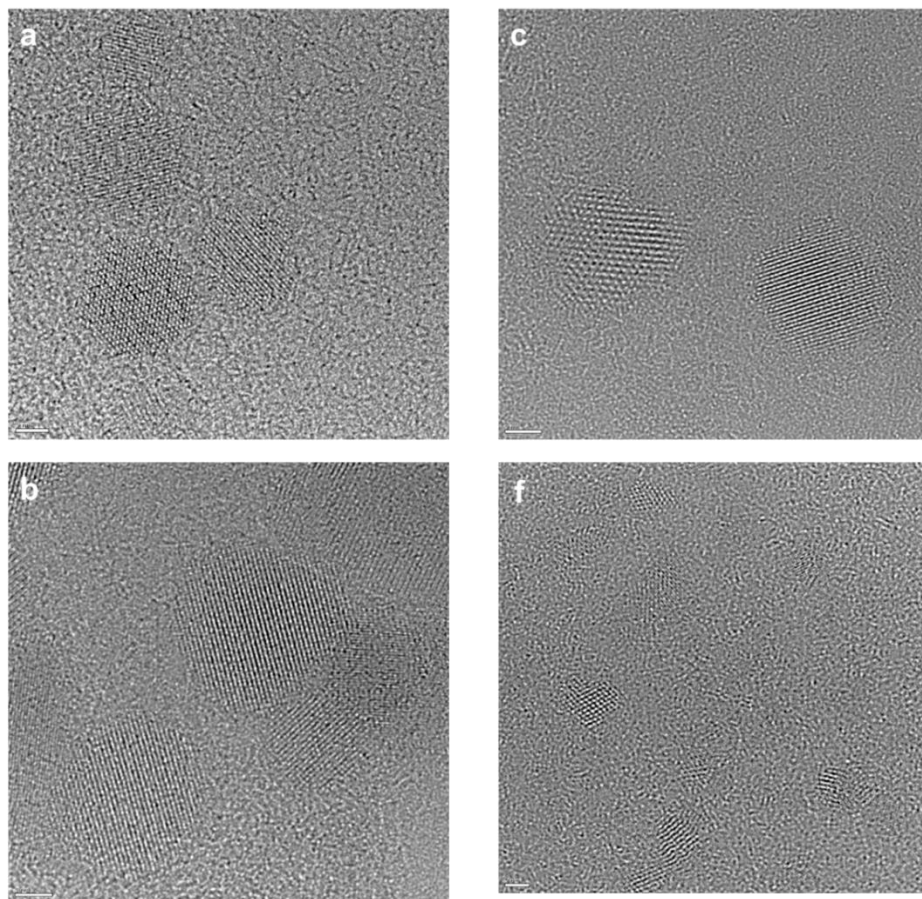
Figure S3 – HRTEM images of CdTe. Scale bar: 2nm
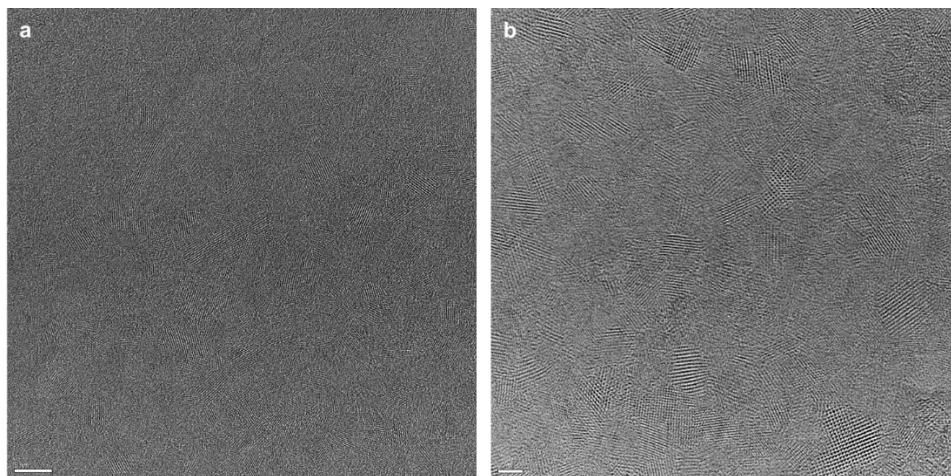
Figure S4 – HRTEM images of CdTe. a) Scale bar: 5 nm; b) scale bar: 2 nm
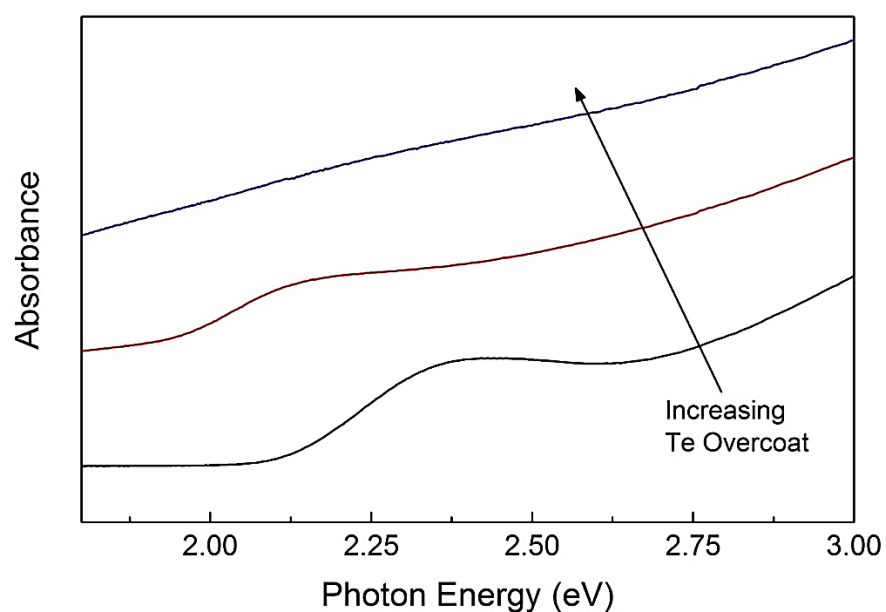
Figure S5 – Absorbance spectra showing the effect of adding an analogous Te overcoat (CdTe@Te) on the optical properties of the nanoparticles. Compared to the cores (black line) adding additional tellurium causes a large red-shift in the peak position and causes the background to assume scattering features (red line). Adding the same molar equivalent Te as used in the CdTe@Cd core-shells results in a spectrum devoid of excitionic features which is dominated by scattering extinction (blue line).

References

1) Apel, K., and Hirt, H. (2004). Reactive oxygen species: metabolism, oxidative stress, and signal transduction. *Annu. Rev. Plant Biol.* 55, 373–399.doi: 10.1146/annurev.arplant.55.031903.141701

2) Bonnett, R. (1995). Photosensitizers of the porphyrin and phthalocyanine series for photodynamic therapy. *Chem. Soc. Rev.* 24, 19–33.doi:10.1039/cs9952400019

3) Buettner, G. R. (1987). Spin trapping: esr parameters of spin adducts. *Free Radic. Biol. Med.* 3, 259–303. doi: 10.1016/S0891-5849(87)80033-3

4) Chan, W., Shiao, N., and Lu, P. (2006). CdSe quantum dots induce apoptosis in human neuroblastoma cells via mitochondrial-dependent pathways and inhibition of survival signals. *Toxicol. Lett.* 167, 191–200. doi:10.1016/j.toxlet.2006.09.007

5) Cho, S. J., Maysinger, D., Jain, M., Röder, B., Hackbarth, S., and Winnik, F. M. (2007). Long-Term exposure to CdTe quantum dots causes functional impairments in live cells. *Langmuir*23,1974–1980.doi:10.1021/la060093j

6) Choi, H. S., Liu, W., Misra, P., Tanaka, E., Zimmer, J. P., Ipe, B. I., et al. (2007). Renal clearance of quantum dots. *Nat. Biotechnol.* 25, 1165–1170. doi: 10.1038/nbt1340

7) Connor, E. E., Mwamuka, J., Gole, A., Murphy, C. J., and Wyatt, M. D. (2005). Gold nanoparticles are taken up by human cells but do not cause acute cytotoxicity. *Small* 1, 325–327.doi:10.1002/smll.200400093

8) Courtney, C. M., Goodman, S. M., McDaniel, J. A., Madinger, N. E., Chatterjee, A., and Nagpal, P. (2016). Photoexcited quantum dots for killing multidrugresistant bacteria. *Nat. Mater.*15,529–534.doi:10.1038/nmat4542

9) Courtney, C. M., Goodman, S. M., Nagy, T. A., Levy, M., Bhusal, P., Madinger, N. E., et al. (2017). Potentiating antibiotics in drug-resistant clinical isolates via stimuli-activated superoxide generation. *Sci. Adv.* 3:e1701776. doi: 10.1126/sciadv.1701776

10) Dai, T., Huang, Y.-Y., and Hamblin, M. R. (2010). Photodynamic therapy for localized infections – state of the art. *Photodiagn. Photodyn. Ther*. 6, 170–188. doi: 10.1016/j.pdpdt.2009.10.008

11) Dumas, E., Gao, C., Suffern, D., Bradforth, S. E., Dimitrijevic, N. M., and Nadeau, J. L. (2010). Interfacial charge transfer between CdTe quantum dots and gram-negative vs gram positive bacteria. *Environ. Sci. Technol.* 44, 1464–1470. doi: 10.1021/es902898d

12) Feng, Z. V., Gunsolus, I. L., Qiu, T. A., Hurley, K. R., Nyberg, L. H., Frew, H., et al. (2015). Impacts of gold nanoparticle charge and ligand type on surface binding and

toxicity to gram-negative and gram-positive bacteria. *Chem. Sci.* 6, 5186–5196. doi: 10.1039/C5SC00792E

13) Finkelstein, E., Rosen, G. M., and Rauckman, E. J. (1980). Spin trapping of superoxide and hydroxyl radical: practical aspects. *Arch. Biochem. Biophys.* 200, 1–16. doi: 10.1016/0003-9861(80)90323-9

14) Gao, L., Liu, R., Gao, F., Wang, Y., Jiang, X., and Gao, X. (2014). Plasmon Mediated generation of reactive oxygen species from near-infrared light excited gold nanocages for photodynamic therapy *in vitro*. *ACS Nano* 8, 7260–7271.doi: 10.1021/nn502325j

15) Gao, X., Cui, Y., Levenson, R. M., Chung, L. W. K., and Nie, S. (2004). *In vivo* cancer targeting and imaging with semiconductor quantum dots. *Nat. Biotechnol.* 22, 969–976. doi:10.1038/nbt994

16) Glozman, A., Lifshitz, E., Hoppe, K., Rogach, A. L., Welllr, H., and Echymüller, A. (2001). Optically detected magnetic resonance of thiol-capped CdTe nanocrystals. *Isr. J. Chem.*41,39–44.doi:10.1560/GVFT-60DT-8Y0E-7DR9

17) Gomes, S. A. O., Vieira, C. S., Almeida, D. B., Santos-Mallet, J. R., MennaBarreto, R. F. S., Cesar, C. L., et al. (2011). CdTe and CdSe quantum dots cytotoxicity: a comparative study on microorganisms. *Sensors* 11, 11664–11678. doi: 10.3390/s111211664

18) Grabolle, M., Spieles, M., Lesnyak, V., Gaponik, N., Eychmüller, A., and ReschGenger, U. (2009). Determination of the fluorescence quantum yield of quantum dots: suitable procedures and achievable uncertainties. *Anal. Chem.*81, 6285–6294. doi: 10.1021/ac900308v

19) Hamblin, M. R., and Hasan, T. (2014). Photodymamic therapy: a new antimicrobial approach to infectious disease? *Photochem. Photobiol. Sci.* 3, 436–450. doi: 10.1039/b311900a

20) World Health Organization (2018). *WHO Antimicrobial Resistance.* Available Online at: http://www.who.int/mediacentre/factsheets/fs194/en/

21) Hirsch, L. R., Stafford, R. J., Bankson, J. A., Sershen, S. R., Rivera, B., Price, R. E., et al. (2003). Nanoshell-Mediated near-infrared thermal therapy of tumors under magnetic resonance guidance. *Proc. Natl. Acad. Sci. U.S.A.* 100, 13549–13554. doi: 10.1073/pnas.2232479100

22) Huang, X., El-Sayed, I. H., Qian, W., and El-Sayed, M. A. (2006). Cancer cell imaging and photothermal therapy in the near-infrared region by using gold nanorods. *J. Am. Chem. Soc.*128,2115–2120.doi:10.1021/ja057254a

23) Imlay, J. A. (2013). The molecular mechanisms and physiological consequences of oxidative stress: lessons from a model bacterium. *Nat. Rev. Microbiol.* 11, 443–454. doi: 10.1038/nrmicro3032

24) Ipe, B. I., Lehnig, M., and Niemeyer, C. M. (2005). On the generation of free radical species from quantum dots. *Small* 1, 706–709. doi: 10.1002/smll.200500105

25) Jarvi, M. T., Niedre, M. J., Patterson, M. S., and Wilson, B. C. (2006). Singlet Oxygen Luminescence Dosimetry (SOLD) for photodynamic therapy: current status , challenges and future prospects. *Photochem. Photobiol.* 82, 1198–1210. doi: 10.1562/2006-05-03-IR-891

26) Katari, J. E. B., Colvin, V. L., and Alivisatos, A. P. (1994). X-ray photoelectron spectroscopy of CdSe nanocrystals with applications to studies of the nanocrystal surface. *J.Phys.Chem.*98,4109–4117.doi:10.1021/j100066a034

27) Kirchner, C., Liedl, T., Kudera, S., Pellegrino, T., Javier, A. M., Gaub, H. E., et al. (2005). Cytotoxicity of colloidal CdSe and CdSe/ZnS nanoparticles. *Nano Lett.* 5, 331–338. doi: 10.1021/nl047996m

28) Lovric, J., Bazzi, H. S., Cuie, Y., Fortin, G. R. A., Winnik, F. M., and ´ Maysinger, D. (2005). Differences in subcellular distribution and toxicity of green and red emitting CdTe quantum dots. *J. Mol. Med.* 83, 377–385. doi: 10.1007/s00109-004-0629-x

29) Lu, Z., Li, C. M., Bao, H., Qiao, Y., Toh, Y., and Yang, X. (2008). Mechanism of antimicrobial activity of CdTe quantum dots. *Langmuir* 24, 5445–5452. doi: 10.1021/la704075r

30) Ma, J., Chen, J. Y., Idowu, M., and Nyokong, T. (2008). Generation of singlet oxygen via the composites of water-soluble thiol-capped CdTe quantum dotssulfonated aluminum phthalocyanines. *J. Phys. Chem. B* 112, 4465–4469. doi: 10.1021/jp711537j

31) Medintz, I. L., Uyeda, H. T., Goldman, E. R., and Mattoussi, H. (2005). Quantum dot bioconjugates for imaging, labelling and sensing. *Nat. Mater.* 4, 435–446. doi: 10.1038/nmat1390

32) Michalet, X., Pinaud, F. F., Bentolil, L. A., Tsay, J. M., Doose, S., Li, J. J., et al. (2005). Quantum dots for live cells, *in vivo* imaging and diagnostics. *Science* 307, 538–545. doi: 10.1126/science.1104274

33) Nagy, A., Steinbrück, A., Gao, J., Doggett, N., Hollingsworth, J. A., and Iyer, R. (2012). Comprehensive analysis of the effects of cdse quantum dot size, surface charge, and functionalization on primary human lung cells. *ACS Nano* 6, 4748–4762. doi: 10.1021/nn204886b

34) Pitout, J. D. D., and Laupland, K. B. (2008). Extended-Spectrum β-LactamaseProducing Enterobacteriaceae: an emergin public-health concern. *Lancet* 8, 159–166. doi: 10.1016/S1473-3099(08)70041-0

35) Reynolds, T. S., Courtney, C. M., Erickson, K. E., Wolfe, L. M., Chatterjee, A., Nagpal, P., et al. (2017). ROS mediated selection for increased NADPH availability in *Escherichia Coli*. *Biotechnol. Bioeng.* 114, 2685–2689. doi: 10.1002/bit.26385

36) Schneider, R., Wolpert, C., Guilloteau, H., Balan, L., Lambert, J., and Merlin, C. (2009). The exposure of bacteria to CdTe-core quantum dots: the importance of surface chemistry on cytotoxicity. *Nanotechnology* 20:225101. doi: 10.1088/0957-4484/20/22/225101

37) Thannickal, V. J., and Fanburg, B. L. (2000). Reactive oxygen species in cell signaling. *Am. J. Physiol. Lung Cell. Mol. Physiol.* 279, L1005–L1028. doi: 10.1152/ajplung.2000.279.6.L1005

38) Trachootham, D., Alexandre, J., and P, H. (2009). Targeting cancer cells by ROSmediated mechanisms: a radical therapeutic approach? *Nat. Rev. Drug Discov.* 8, 579–591. doi: 10.1038/nrd2803

39) Tsay, J. M., Pflughoefft, M., Bentolila, L. A., and Weiss, S. (2004). Hybrid approach to the synthesis of highly luminescent CdTe/ZnS and CdHgTe/ZnS nanocrystals. *J. Am. Chem.Soc.*126,1926–1927.doi:10.1021/ja039227v

40) Valko, M., Leibfritz, D., Moncol, J., Cronin, M. T. D., Mazur, M., and Telser, J. (2007). Free radicals and antioxidants in normal physiological functions and human disease. *Int. J. Biochem. Cell Biol.* 39, 44–84. doi: 10.1016/j.biocel.2006.07.001

41) Wondrak, G. T. (2009). Redox-Directed cancer therapeutics: molecular mechanisms and opportunities. *Antioxid. Redox Signal.* 11, 3013–3069. doi: 10.1089/ars.2009.2541

42) Yu, B. P. (1994). Cellular defenses against damage from reactive oxygen species. *Physiol.Rev.*74,139–162.doi:10.1152/physrev.1994.74.1.139

43) Yu, W. W., Qu, L., Guo, W., and Peng, X. (2003). Experimental determination of the extinction coefficient of CdTe, CdSe, and CdS nanocrystals. *Chem. Mater.* 15, 2854–2860. doi:10.1021/cm034081k

44) Zeng, C., Ramos-Ruiz, A., Field, J. A., and Sierra-Alvarez, R. (2015). Cadmium Telluride (CdTe) and Cadmium Selenide (CdSe) leaching behavior and surface chemistry in response to pH and O2. *J. Environ. Manage.* 154, 78–85. doi: 10.1016/j.jenvman.2015.02.033

45) Zwietering, M. H., Jongenburger, I., Rombouts, F. M., and Vant Riet, K. (1990). Modeling of the bacterial growth curve. *Appl. Environ. Microbiol.* 56, 1875–1881.

Chapter 4

Zn$_{(1-x)}$Cd$_x$Te alloy quantum dot as more biocompatible nanotherapeutic agent by reduction of cadmium content

Reproduced with permission from Max Levy, <u>Partha P. Chowdhury</u>, Kristen Eller, Anushree Chatterjee, Prashant Nagpal. Tuning ternary Zn$_{1-x}$Cd$_x$Te quantum dot composition: Engineering bandgap, electronic states, electrochemical potential, and light-activated superoxide generation as therapeutic against multidrug-resistant bacteria. *ACS Biomaterials Science & Engineering* (under review)

Introduction

Considerable attention has been given to the rise of multi-drug resistant pathogens as a critical impending problem in global health. In a 2014 commissioned study on antimicrobial resistance, the impact was estimated to be upwards of 300 million lives and $100 trillion by 2050. [1] More recently, this mounting risk prompted the World Health Organization (WHO) to release a first-ever list of "priority pathogens," classified by three tiers of urgency: critical, high, medium. The highest tier corresponds to existing pathogens with resistance to carbapenem—a last resort antibiotic—and includes strains of *Escherichia coli*. The problem is compounded by a steady decline in new antibiotics entering the market, growing resistance in pathogens against traditional small molecule therapies, and a lack of financial incentives and scientific breakthroughs in designing a new class of antibiotics now for more than 30 years. As an alternative approach, nanoparticle-based therapeutics offer stability, facile transport, low-cost, and scalable synthesis. Many groups have focused on causing physical and chemical

changes in the nanoparticles' surrounding environment by using electromagnetic stimuli such as light, resulting in alternative approaches such as photothermal therapy,[2,3] photodynamic therapy,[4,5] and light-activated quantum dot (QD) therapeutics.[6-9] While photothermal therapy uses decay of surface plasmon polaritons and consequent conversion of incident light energy into heat to kill cells, the mechanism of action for photodynamic and QD therapies often use the generation of reactive oxygen species (ROS). The ROS classification includes several species—hydroxyl radical ($OH^\bullet$), superoxide radical ($O_2^\bullet$), hydrogen peroxide (H_2O_2), and singlet oxygen ($^1O_2$)—which have very different roles and reactivity in cells.[9-11] Light-activated QD therapeutics offer a unique opportunity to modulate the nanoparticle's quantum-confined conduction and valence band states using size, composition, and shape, thereby rationally changing its reduction and oxidation potentials for photochemistry and selectively generating ROS and reactive nitrogen species (RNS).[6-9] While the flux of several ROS/RNS species can kill MDR pathogens, superoxide stands out as an effective therapeutic agent to eliminate infection without harming the host. QDs, which generate superoxide intracellularly by donating electrons to dissolved oxygen upon excitation with visible light, were identified as a potential candidate for selective therapeutic.

This process for rational design of superoxide-generating QDs using visible light relies on having a small bandgap (for visible light activation), a sufficiently high conduction band position to donate electrons to dissolved oxygen and produce superoxide selectively, a valence band position low enough to prevent generation of indiscriminately reactive hydroxyl species on light activation, and appropriate QD surface and ligand charge to ensure small hydrodynamic radius for facile transport and uptake by cells. Concerns over the potential use of cadmium QDs have motivated work to prevent Cd^{2+} leaching for applications such as bio-imaging and drug

delivery.[12-14] In addition, we have shown that zinc sulfide can be used to cover facets on the CdTe surface, but that this ZnS shell must be very thin to allow required charge injection.[8] Replacing a majority of the cadmium within the quantum dots with non-toxic zinc would improve innate host biocompatibility.[15] Here, we report composition-tuning a ternary zinc cadmium telluride ($Zn_{1-x}Cd_xTe$) nanotherapeutic with a vanishing small overall concentration of cadmium (parts per billion, or ppb) to achieve the same therapeutic effect. The ternary QDs are nontoxic to mammalian cells and can kill MDR pathogens, including tier-1 critical carbapenem-resistant (CRE) *Escherichia coli*, using visible light.

MATERIALS AND METHODS:

Quantum Dot Synthesis. CdTe quantum dot synthesis was carried out via hydrothermal method per our previous reports. [6,7] ZnTe and $Zn_{1-x}Cd_xTe$ quantum dots were synthesized in a similar manner. The tellurium precursor was prepared by dissolving 33 mg of sodium borohydride (Fisher) in 1 mL degassed water for injection into a 2 mL vial containing 40 mg tellurium powder (Alfa Aesar). The Te-precursor was left to react in a fume hood for 90 minutes until a magenta colored solution (NaHTe) was obtained. 6.48 mg of Zinc nitrate hexahydrate (21.8 mmol; Sigma) was added to 10 mL of degassed water containing 1.8 µL 3-mercaptopropionic acid (MPA; Alfa Aesar) to serve as a cationic precursor. The reaction mixture (750 µL Zn^{2+} precursor; 750 µL degassed water; 2.5 µL Te precursor) was adjusted to pH 11 and allowed to react at 98˚C for 60 minutes until a colorless ZnTe QD suspension was obtained. For $Zn_{1-x}Cd_xTe$ QDs, the cationic precursor solutions varied in their Zn^{2+}:Cd^{2+} molar ratios—1:1, 5:1, 10:1, 20:1. A greater volume (10 µL) of Te precursor was used in the reaction mixture in order to favor ZnTe bond formation. $Zn_{1-x}Cd_xTe$ QDs reaction proceeded for 30

minutes at 98˚C. CdTe, ZnTe, and $Zn_{1-x}Cd_xTe$ quantum dots were washed 3 times with pH 11 water using Nanosep 3k filters (Pall) and centrifugation at 10,000 rpm for 7 minutes per cycle. Poorly passivated quantum dots were separated by centrifugation (4000 rpm). Sterile techniques were maintained during all quantum dot synthesis.

Quantum Dot Characterization. Quantum dot UV-vis absorbance spectra were measured using a VWR UV-1600PC UV/VIS spectrophotometer. Emission spectra were obtained on a calibrated PTI fluorimeter. QD composition was determined using inductively coupled plasma mass spectrometry (ICP-MS). Composition data represents the average of three replicates and error bars span two standard deviations from the average.

Electrochemical Measurements. We used differential Pulse Voltammetry (DPV) with a Bio-logic SP-200 potentiostat/galvanostat to determine $Zn_{1-x}Cd_xTe$ conduction and valence band positions. Using a three-electrode (working electrode: glassy carbon; counter electrode: platinum wire; reference electrode: Ag/AgCl) configuration, the experiments were conducted using a scanning rate of 20 mV/s (parameters: 50 ms pulse width, 50 mV pulse height, 200 ms step width and 4 mV step height). The forward scan range was from -0.5 V to 1.5 V. The backward scan range was from 0.5 V to -1.8 V. We used deionized water purged with Argon (30 minutes) as a solvent, and sodium sulfate (Fisher) as the electrolyte. All the experiments were carried out at room temperature.

Superoxide Detection. Superoxide generation was confirmed using a Bruker Elexsys E 500 electron paramagnetic resonance (EPR) spectrometer with an SHQE resonator operated in a dark room. We used a power of 5 W and a microwave attenuation of 16 dB. 100 µL aliquots of QD suspensions were prepared for EPR by adding 1 µL of spin-trapping agent 5,5-dimethyl-1-pyrroline N-oxide (DMPO) in dark conditions. DMPO forms stable detectable

adducts with radical species such as superoxide.[16] After loading sample suspension into quartz capillaries, a baseline EPR spectrum was measured in the dark. Then, the sample was exposed to 45 seconds of a visible light source and quickly returned to the EPR for measurement. Excitation for ZnTe involved ultraviolet light (312 nm). All EPR measurements represent the average of 10 successive scans (20.48 s each). Radicals were identified and quantified using Bruker's SpinFit program and characteristic hyperfine coupling constants for the superoxide adduct, DMPO-OOH (a_N = 14.2 G, a_H^β = 11.4 G, $a_H^{\Upsilon 1}$ = 1.2 G) and the hydroxyl radical adduct, DMPO-OH (a_N = 14.90 G, a_H^β = 14.93 G).[17]

Cell Culture and Therapeutic Analysis. Individual colonies of *E. coli* MG1655 were picked from solid Luria-Bertani (LB; Sigma) medium (2% LB; 1.5% agar; Fisher) and added to 1 mL LB broth (2%) for overnight incubation (16 h; 37°C; 225 rpm shaking). Resulting cultures were diluted 1:100 in fresh LB medium (2%) for experiments in culture plates (96-well plates; Greiner). CdTe, ZnTe, $Zn_{1-x}Cd_xTe$ suspensions were washed and re-dispersed in LB and added to respective wells as a treatment. Bacterial growth was monitored via optical density (590 nm; 30-minute intervals) using a microplate reader (Tecan GENios). A thin LED sheet was taped to the ceiling of the microplate reader to provide a constant light source. The temperature was held fixed at 37°C. Clinical isolate (carbapenem-resistant *E. coli*) was obtained from the University of Colorado Anschutz campus. CRE *E. coli* cell culture was conducted in the same manner as described above, except for the medium used: cation-adjusted Mueller Hinton broth (CAMHB; VWR). Data represents the average of three biological replicates and error bars span two standard deviations.

HeLa Cell Culture. HeLa cells, maintained long-term in 10% dimethyl sulfoxide (DMSO) freezer stocks, were cultured in Dulbecco's Modified Eagle Medium (DMEM, Fisher

Scientific), 10% Fetal Bovine Serum (FBS, Advanced, Atlanta Biologics), and 50 units/mL

Penicillin Streptomycin (P/S; Fisher Scientific). HeLa cells were started from a freezer stock at

passage and split into three separate biological replicates which were continuously passaged as

separate biological replicates; experiments were performed at passage 6. Cells were grown at

$37°C$, 5% CO_2, and controlled humidity to 80% confluency and passaged using 0.25% trypsin

(HyClone) on to 96 well tissue culture treated plates (Fisher Scientific) at a density of 4,500

cells/well 24 hours prior to QD addition.

Lactate Dehydrogenase Assay. Following 18 hours of incubation with

QDs, 50 µL of water was added to each well to achieve 150 µL of supernatant, and 90 µL of

this supernatant was used to measure lactate dehydrogenase (LDH) release by cells with the

CytoSelect™ LDH Cytotoxicity Assay Kit LDH release correlates to cell toxicity and percent

toxicity can be measured using the following equation:

$$Percent\ Toxicity = \frac{\left(Abs_{450\ nm}^{Treatment} - Abs_{450\ nm}^{Negative\ Control}\right)}{\left(Abs_{450\ nm}^{Positive\ Control} - Abs_{450\ nm}^{Negative\ Control}\right)} \tag{1}$$

Growth Calculations. Normalized inhibition was calculated according to

the equations (1-2). The change in bacterial optical density (ΔOD) is measured with respect to

OD in the absence of treatment.

$$\Delta OD_{treatment} = OD_{treatment,\ t} - OD_{no\ treatment,\ t} \tag{2}$$

$$Inhibition = \frac{\Delta OD_{treatment}}{OD_{control}} \tag{3}$$

GIC50 Method. To determine GIC_{50} values for use in subsequent calculations, we used phototoxicity data obtained from our bacterial cell culture in the presence of QDs and light. GIC_{50} values were calculated individually for each QD of varying composition (x). First, inhibition at t=12 hours was calculated using Equation 3. We selected t=12 hours as this time-point showed equilibrated growth in our no-treatment control. Because we tested discrete values of QD dosage (12.5, 25, 50, 100 nM), we selected each GIC_{50} as the minimum dosage which demonstrated *at least* 50% inhibition (Fig. S5).

Effective cadmium content for nano-therapy. Effective cadmium content for therapy using these QDs was determined by analyzing the peak phototherapeutic effect versus cadmium content. Data from ICP-MS yielded amounts of cadmium per QD suspension with units of (ppb Cd_{2+}/nM QD). Next, cell culture data provided the concentrations necessary for each different QD to inhibit bacterial growth by 50% (GIC_{50} values) in units of nM. The product of these two values is a metric (with units in ppb) that corresponds to a cadmium content for therapeutic effect. We deem the QD with the lowest value to be optimal, as this corresponds to a minimum of cadmium content. ZnTe was not included in this analysis because it contained no cadmium and presented no therapeutic effects.

RESULTS AND DISCUSSIONS

To reduce the cadmium content in a QD-superoxide therapy, we began by synthesizing zinc telluride QDs. Zinc telluride is a semiconductor with a direct band gap of 2.26 eV in bulk (versus 1.5 eV for CdTe in bulk). Synthesized ZnTe QDs showed a weak excitonic peak at around 330 nm and a broad tail extending to higher wavelengths (Fig. 1a). In contrast,

CdTe-2.4 QDs clearly showed visible light absorbance with an excitonic peak near 520 nm. CdTe-2.4 QDs also showed a strong fluorescence peak centered ~549] nm (Fig. 1a). As reported in other studies, the ZnTe QDs exhibited negligible fluorescence when measured (Fig. S1). [19,20] The observed band gap of synthesized ZnTe QDs was 3.3 eV, versus 2.4 eV for CdTe-2.4 QDs. Due to the heavy-hole states from tellurium, as well as other reports in the literature, we did not observe a significant difference in the position of the ZnTe QD VB relative to that of CdTe-2.4 QDs (Fig. S2). [21,22] With their similar VB position and large bandgap, ZnTe QDs had a higher (more negative) CB position and greater consequent reduction in electrochemical measurements. As observed in our DPV measurements, the ZnTe QD CB shifts up relative that of CdTe-2.4 QDs to well above the threshold for superoxide generation (Fig. 1b). In order to validate the ability of ZnTe QDs to generate superoxide radicals, we used electron paramagnetic resonance (EPR) spectroscopy coupled with spin-trapping. Upon illumination with a UV light source, we detected characteristic peaks corresponding to superoxide and hydroxyl radical adducts—DMPO-OOH and DMPO-OH, respectively (Fig. 1c). As previously reported with CdTe-2.4 and other sources of superoxide, the DMPO-OH adduct was formed indirectly via decomposition of DMPO-OOH, and not via direct injection of photogenerated holes from the QDs to water for hydroxyl radical generation.[9,23,24] This is supported by the VB position for both CdTe-2.4 and ZnTe QDs which lies below the threshold for OH• generation, as well as further electrochemical measurements in presence and absence of dissolved oxygen. A comparable EPR spectra was observed for CdTe-2.4 QDs illuminated by visible light (Fig. 1c); ZnTe QDs generated no measurable radical species when illuminated by visible light.

To evaluate the composition-tuned ternary $Zn_{1-x}Cd_xTe$ for intracellular superoxide generation and their therapeutic potential, we utilized CdTe-2.4 QDs as a positive control and monitored the superoxide generation responsible for the selective killing of bacteria in the presence of visible light (Fig. 1d).[6–9] ZnTe QDs (x=0) could not generate intracellular superoxide with visible light. As such, further tests on bacterial growth in cell culture in the presence of visible light and ZnTe QDs confirmed their inefficacy as visible-light activated QD therapeutics (Fig. 1e). Despite its favorable CB position, ZnTe could not serve as a nanotherapeutic alternative to CdTe- 2.4 because of its large bandgap in the ultraviolet (UV). UV is more harmful than visible light and less able to penetrate surfaces such as skin. To reduce the risk of cadmium toxicity, while maintaining visible light photochemical properties, we synthesized different $Zn_{1-x}Cd_xTe$ QDs (varying x, Fig. 1f), via a modified hydrothermal method (see methods). [25–28]
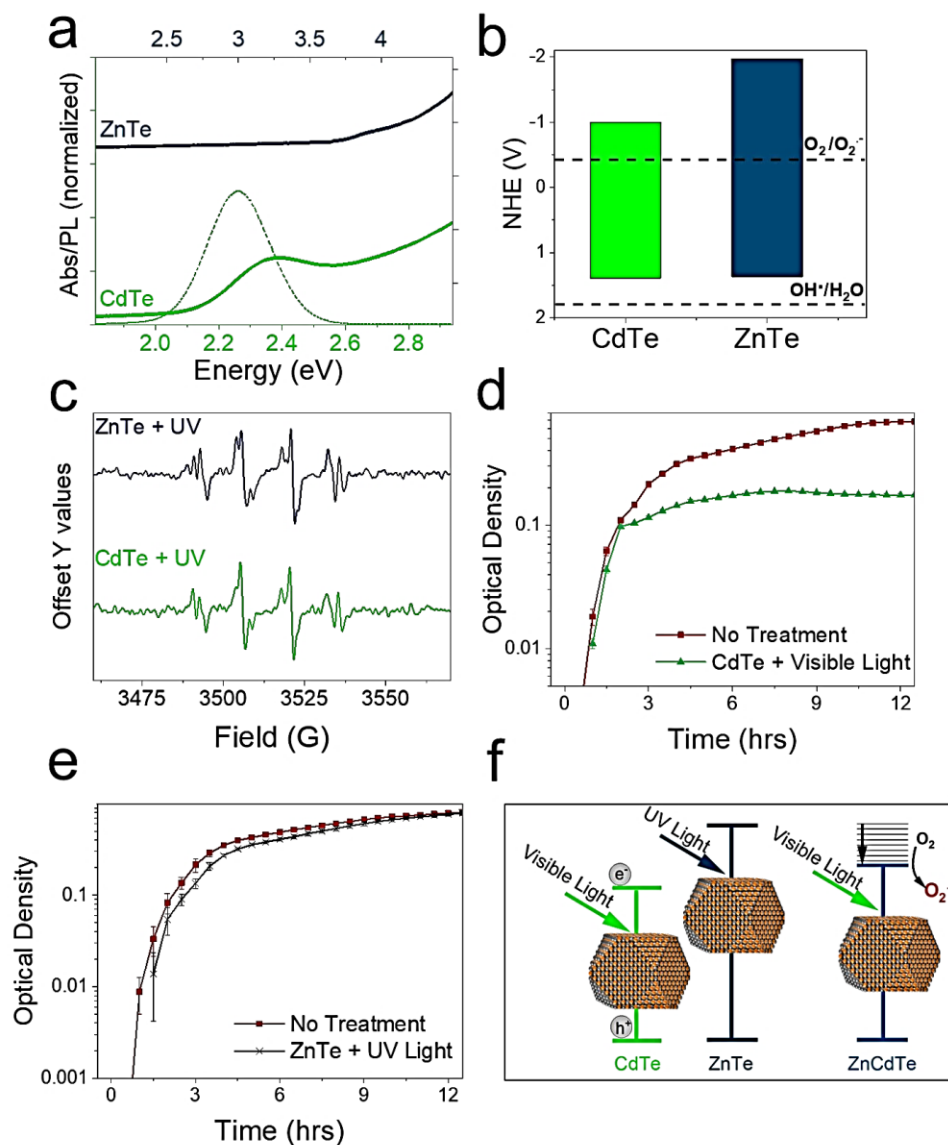
Figure 1. Design of ternary Zn1-xCdxTe QDs. a) Absorption/photoluminescence spectra (solid/dashed) for CdTe-2.4 (green) and ZnTe (blue) on respective scales. ZnTe QDs showed negligible fluorescence. **b)** CB-VB positions (vs. NHE) of CdTe-2.4 (green) and ZnTe (blue) QDs compared to redox potentials for water oxidation/reduction reactions (dashed lines). Band alignment shows that superoxide generation should be energetically favorable. **c)** EPR spectra of ZnTe QDs illuminated with UV light (top), and CdTe-2.4 QDs illuminated with visible light (bottom), confirming superoxide generation. **d-e)** Normalized growth curve for *E. coli* MG1655 in the presence and absence of photo-activated CdTe **(d)** and ZnTe **(e)** in LB medium. CdTe-2.4

photo-inhibition can be attributed to the generation of intracellular superoxide radicals which impair cell growth beyond a relatively low nominal threshold. ZnTe displays no phototherapeutic effect **f)** Schematic depicting visible light activity of CdTe-2.4 (left), UV requirement for ZnTe (middle), and proposed visible light active ternary Zn1-xCdxTe QDs (right). Minimal cadmium content may be sufficient for desired photochemistry and the resultant phototherapeutic behavior via superoxide generation

Using inductively coupled plasma mass spectrometry (ICP-MS) we found that increased zinc loading in precursor solutions yields greater zinc incorporation (Fig. 2a). Precursor Zn_{2+}:Cd_{2+} ratios used—1:1, 5:1, 10:1, 20:1—produced $Zn_{1-x}Cd_xTe$ QDs of $1-x = 0.04$, 0.11, 0.63 and 0.68, respectively. High molar ratios of Zn_{2+} to Cd_{2+} are required because cadmium's reactivity with tellurium is higher than that of zinc. [29] Zinc ultimately becomes the primary cation in the 10:1 and 20:1 mixture, where the degree of zinc incorporation levels out near 70%. Precursor cation ratios above 20:1 did not produce stable QDs, likely due to a combination of high cation loading and ZnTe instability— observations consistent with other reports in the literature. [25] In characterizing the different $Zn_{1-x}Cd_xTe$ QDs, we observed that zinc incorporation leads to electronic properties approaching those of ZnTe. Photoluminescence (PL) measurements show a clear blue-shift in PL peak position with increasing zinc content, as well as a concomitant decrease in fluorescence intensity (Fig. 2b). The same trend of blue-shifting is apparent from the UV-vis absorbance spectra (Fig. S3). These observations can be explained by the formation of ZnTe bonds in place of CdTe bonds. Compared to CdTe-2.4, ZnTe has shorter, stronger bonds. [26,29] The greater covalent nature raises dislocation energies, thus shifting absorption and PL values towards higher energy blue wavelengths. Further, decreased fluorescence intensity likely results from intrinsic zinc defects or TeO facets

on the QD surface. [8,15]. Following investigations of their bandgaps and optical properties, we characterized the electrochemical redox properties of composition-tuned $Zn_{1-x}Cd_xTe$ QDs. As with the change from CdTe-2.4 to ZnTe QDs (x=1 to 0), we hypothesized that the CB would shift upwards (higher energy) with increasing zinc content. Additionally, increasing x (cadmium element presence) should introduce lower energy states and impart a lower band gap than that of ZnTe.[15] Using DPV, we confirmed that zinc incorporation increases the QD band gap relative to CdTe by moving the CB (Fig. 2c). As predicted, all the $Zn_{1-x}Cd_xTe$ QDs have the electrochemical capacity for superoxide generation and have band gaps significantly lower than that of ZnTe.
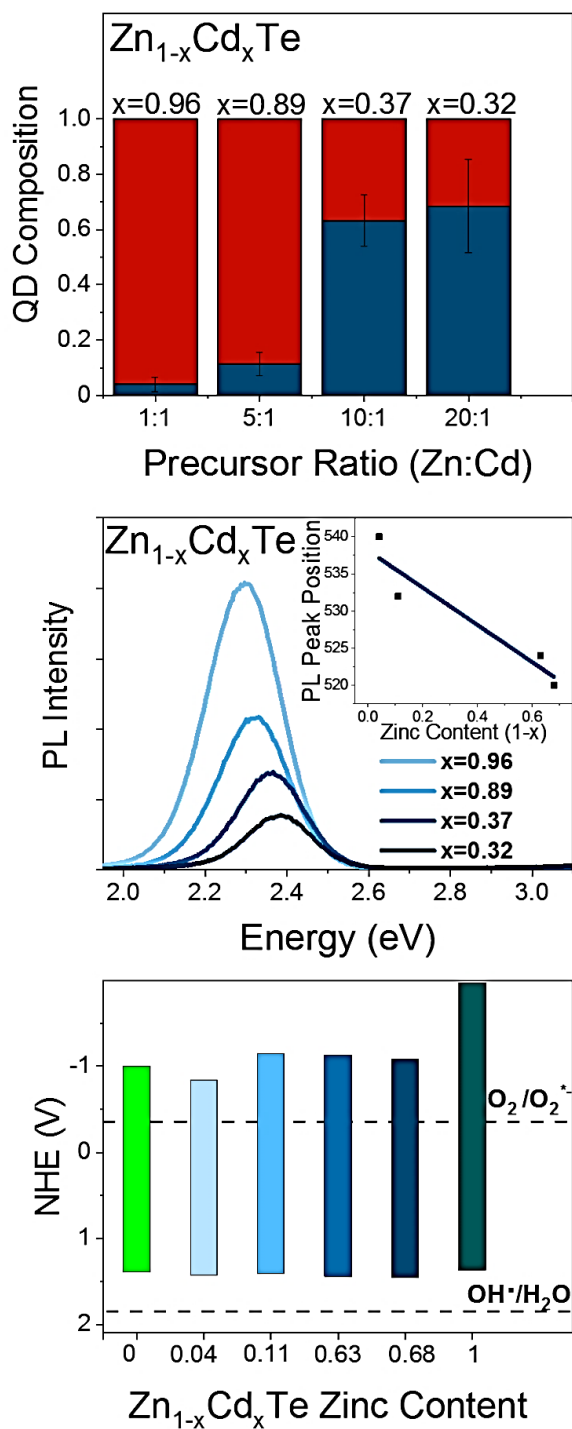
Figure 2. Tuning the bandgap, electronic states, and CB-VB position in Zn1-xCdxTe QDs.
a) Breakdown of cation composition in Zn1-xCdxTe QDs obtained from different synthetic conditions. Zinc incorporation (blue) increases with increasing Zn:Cd precursor ratio, relative

to cadmium (red). Composition measurements obtained via ICP-MS. **b)** Photoluminescence spectra for $Zn_{1-x}Cd_xTe$ of varying composition. As zinc incorporation increases, QDs display a blue shift in emission peak **(inset)**—consistent with their increasing band gap. **c)** CB-VB positions (vs. NHE) of QDs showing that superoxide generation occurs. Darker shades of blue denote greater zinc incorporation.

We used EPR to verify radical generation upon excitation with visible light. After 45 seconds of illumination, EPR spectra show characteristic peaks corresponding to superoxide radical adducts (Fig. S4). All samples, spanning different degrees of zinc incorporation, demonstrated a response to visible light (Fig. 3a). Most $Zn_{1-x}Cd_xTe$ QDs with varying compositions showed comparable, or higher superoxide generation than the CdTe-2.4 QDs (x=1) used as a positive control. Intracellular superoxide generation is the mechanism of action and the strongest indicator of QD therapeutic effectiveness.[6–9] Therefore, following the successful characterization of the visible bandgap, electronic states, electrochemical potential, and superoxide generation, we assessed the $Zn_{1-x}Cd_xTe$ QD therapeutic effect *in vitro*. We performed cell culture of *E. coli* MG1655 treated with $Zn_{1-x}Cd_xTe$ QDs in the presence of light. In all four cases (*1-x* = 0.04, 0.11, 0.63 and 0.68) $Zn_{1-x}Cd_xTe$ QDs significantly inhibited bacterial growth (Fig. 3b).
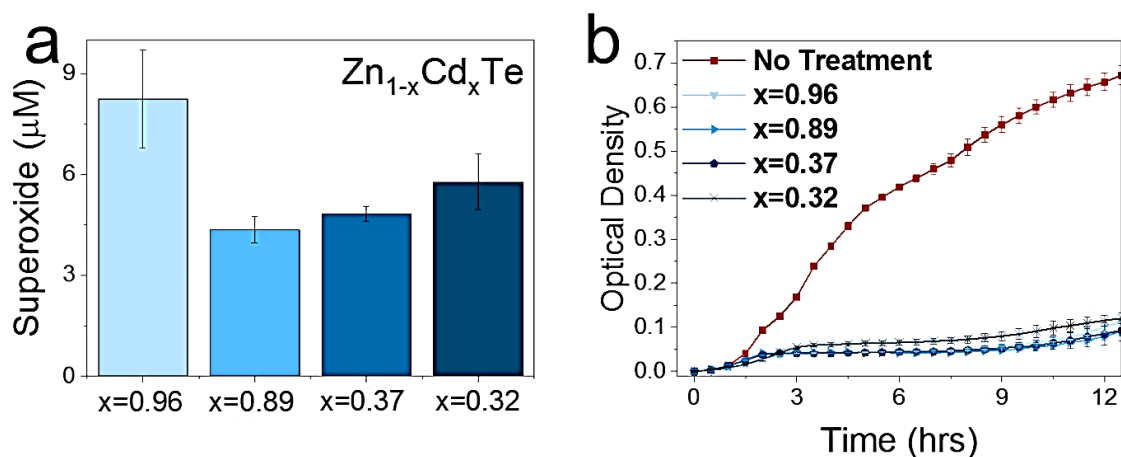
Figure 3. Zn1-xCdxTe displays strong photo-inhibition by generating intracellular superoxide. a) Quantification of superoxide generated by Zn1-xCdxTe suspensions after visible light illumination during EPR spectroscopic measurement. Unlike ZnTe, all ternary Zn1-xCdxTe QDs generate strong superoxide signals with visible light. Darker shades of blue denote greater zinc incorporation. **b)** Normalized growth curve for *E. coli* MG1655 in the presence and absence of photo-activated Zn1-xCdxTe. Equal concentrations (12.5 nM) of each ternary QDs were used *in vitro* bacterial cell culture tests.

Remarkably, these composition-tuned QDs retained the phototherapeutic effect of CdTe-2.4 with drastically lower levels of cadmium. To evaluate the extent of the cadmium content reduction while maintaining the same therapeutic effect, we analyzed our data to develop a metric for the 50% growth inhibition concentration (GIC$_{50}$) multiplied by the cadmium content (in ppb via ICP-MS) for this therapeutic (Fig. S5). This provided us with a metric for cadmium content in the dose required for eliminating pathogenic bacteria, thereby maintaining effectiveness (superoxide dosage) while minimizing cadmium content (Fig. 4a). Using CdTe-2.4 QDs as a positive control, modest effectiveness of the therapeutic led to low GIC$_{50}$ values, but the cadmium content was higher, and would require ~300 ppb of cadmium

for therapeutic effect. Decreasing the cadmium content while maintaining high effectiveness led to a rapid improvement—the cadmium required for the therapy reduced to lower than 50 ppb for $Zn_{0.63}Cd_{0.37}Te$ QD therapy. However, further reducing cadmium content resulted in a gradual decrease in effectiveness and a resulting increase in GIC_{50} values, thereby increasing the effective cadmium content for the same therapeutic action with $Zn_{0.68}Cd_{0.32}Te$ QDs. $Zn_{0.63}Cd_{0.37}Te$ QDs showed optimal therapeutic effect with the lowest cadmium content for effective therapy using visible light. Further elevated levels of zinc incorporation (ZnTe QDs) led to poor photo-activation with visible light and ineffective therapy. [8] The observed phototherapeutic effect was directly attributable to superoxide generation in visible light. Superoxide, being a radical anion, is known to seek out enzymatic and free iron through electrostatic interactions, and hence better able to target potential pathogens. [9,30] Its stability and mechanism of action results in a targeted pathogen killing, unlike other ROS which cause non-specific oxidative stress. [31–33] Normally, intracellular superoxide concentrations are tightly controlled by the enzyme superoxide dismutase (SOD). But this homeostasis is readily perturbed by exogenous sources of the radical—steady-state concentrations of 0.2 nM are known to inhibit bacterial growth. [34] In this case, exogenous superoxide radicals formed by $Zn_{1-x}Cd_xTe$ QDs overwhelmed the *E. coli* defenses. Replacing most of cadmium content by incorporating non-toxic zinc also improves innate host biocompatibility. [16] We evaluated host biocompatibility using mammalian cell culture in the presence of photoactivated $Zn_{1-x}Cd_xTe$. HeLa cells exposed to high doses of illuminated QDs were cultured in comparison to positive and negative toxicity controls. Using a lactate dehydrogenase (LDH) toxicity assay, we found that $Zn_{0.63}Cd_{0.37}Te$ QDs at therapeutic dosages (25 and 50 nM) were not toxic after 18 hours of exposure (Fig. 4b). LDH detection for even the high dose of 50 nM was negligible compared

to the no treatment condition. HeLa cell health was also evaluated by microscopy (Fig. S6). As with the no treatment (negative control), HeLa cells exposed to photoactivated $Zn_{0.63}Cd_{0.37}Te$ were still morphologically healthy. These results signaled a degree of effectiveness that can be used to fight multi-drug resistant infections in humans. To assess the effectiveness of $Zn_{1-x}Cd_xTe$ QDs in countering other MDR bacterial pathogens, we conducted a cell culture with a carbapenem-resistant *E. coli* clinical isolate. CRE *E. coli* is a "Priority 1" critical pathogen, as designated by the World Health Organization. Upon treatment with $Zn_{0.63}Cd_{0.37}Te$, we observed considerable growth inhibition at nanomolar doses (Fig. 4c). After 9 hours of growth, $Zn_{0.63}Cd_{0.37}Te$ QD treatment resulted in strong photo-inhibition (Fig. 4c). Photo-inhibition was apparent, even at 6.25 nM, and it became more apparent as the dosage increased. A 25 nM dose of $Zn_{0.63}Cd_{0.37}Te$ resulted in approximately 80% inhibition of the Priority 1 antibiotic-resistant pathogen.
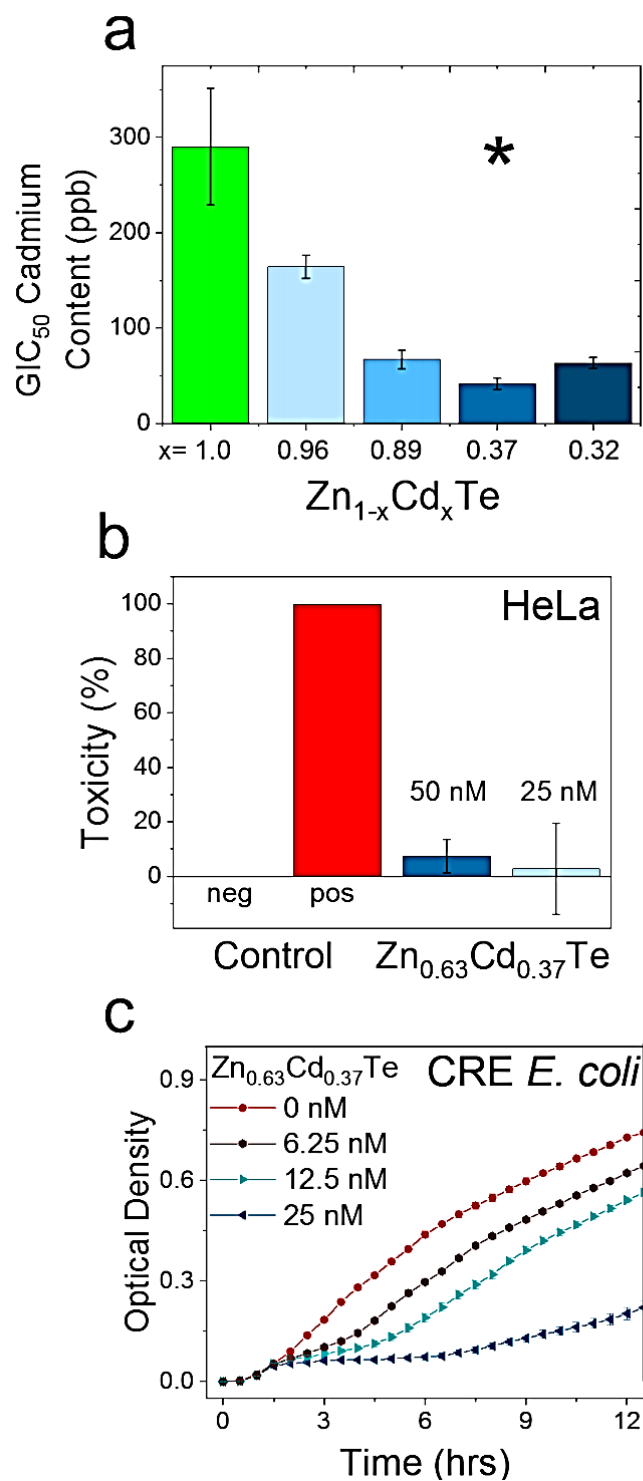
Figure 4. Zn1-xCdxTe kills Priority 1 pathogen with minimal cadmium and shows no toxicity in mammalian cells. a) Effective cadmium content calculated using the product of

GIC50 and parts per billion (ppb) cadmium content of the QDs, for the different Zn1-xCdxTe QDs. Zn0.63Cd0.37Te (*) requires the least cadmium to inhibit bacterial growth by 50%. **b)** LDH toxicity assay results for photoactivated Zn0.63Cd0.37Te. Negligible toxicity apparent, even at 50 nM QD concentration. **c)** Normalized growth curve for CRE *E. coli* in the presence and absence of photoactivated Zn0.63Cd0.37Te. Despite its evolved resistance to known antibiotics (including last-resort antibiotic carbapenem), CRE *E. coli* displays growth inhibition due to killing by intracellular generation of superoxide. Phototherapeutic effect of the ternary QDs increases with dosage.

CONCLUSION:

In this study, we demonstrated the composition-tuning of ternary $Zn_{1-x}Cd_xTe$ QDs and elucidated its effect on optical bandgap, electronic states, electrochemical potentials, generation of selective superoxide anions as a therapeutic, and the QD effectiveness in selectively killing "Priority 1" MDR pathogen using visible light. These rationally designed $Zn_{1-x}Cd_xTe$ QDs showed negligible toxicity in mammalian cells and generated intracellular superoxide radical using visible light to provide selective and effective therapy. To further quantify their effectiveness with reducing cadmium content, using CdTe-2.4 QDs as a positive control, our results indicate that, together with a nanomolar dosage, $Zn_{1-x}Cd_xTe$ QDs provides considerable therapeutic effects with minimal cadmium content ($GIC_{50}\times$ppb Cd<50ppb, close to the detection limit of our instrument). This work demonstrates the potential to design a nanotherapeutic that is more benign in its constituent materials and maintains high selectivity towards eliminating a broad range of MDR pathogens, while demonstrating negligible effect on the growth, health, and metabolism of host mammalian cells. Our results highlight the rational design approach towards

developing other effective QD candidates for superoxide-mediated therapeutics, to counter the growing threat of antimicrobial resistance and MDR bacterial infections.

Supplementary Figures
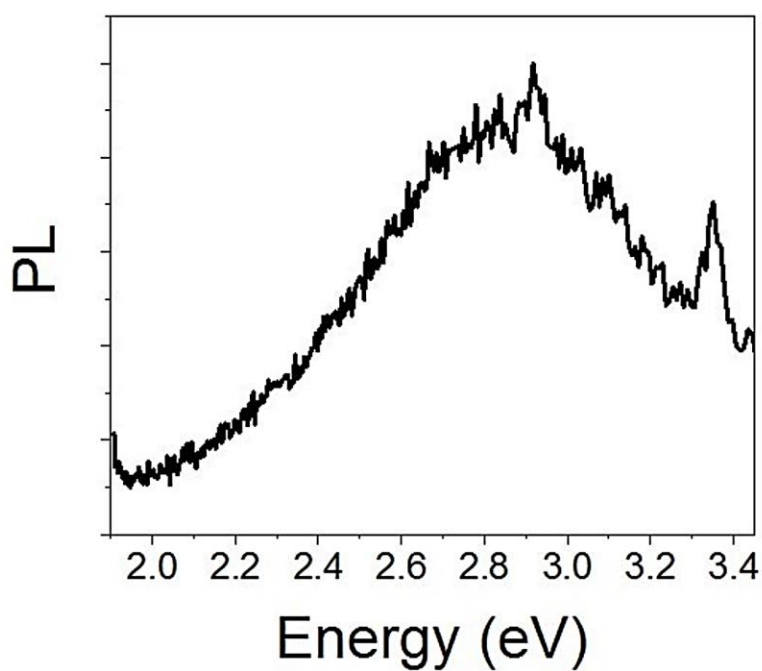
Figure S1. ZnTe Photoluminescence (PL) spectra. ZnTe QDs show negligible fluorescence with a very weak peak around 3.0 eV
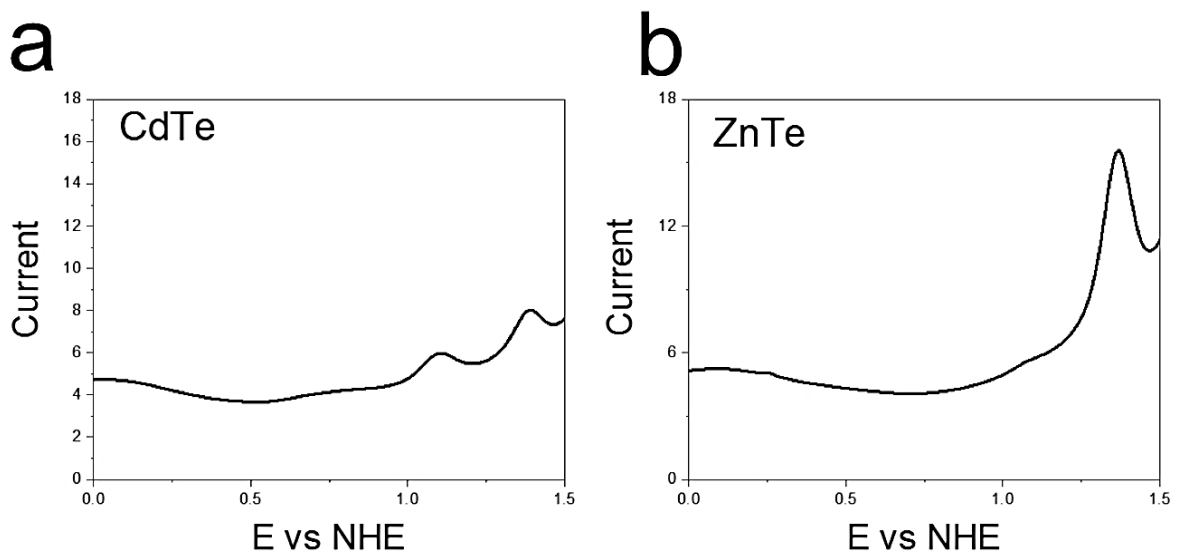
Figure S2. CdTe-2.4 and ZnTe Differential Pulse Voltammetry. DPV measurements show band positions for the two different QDs
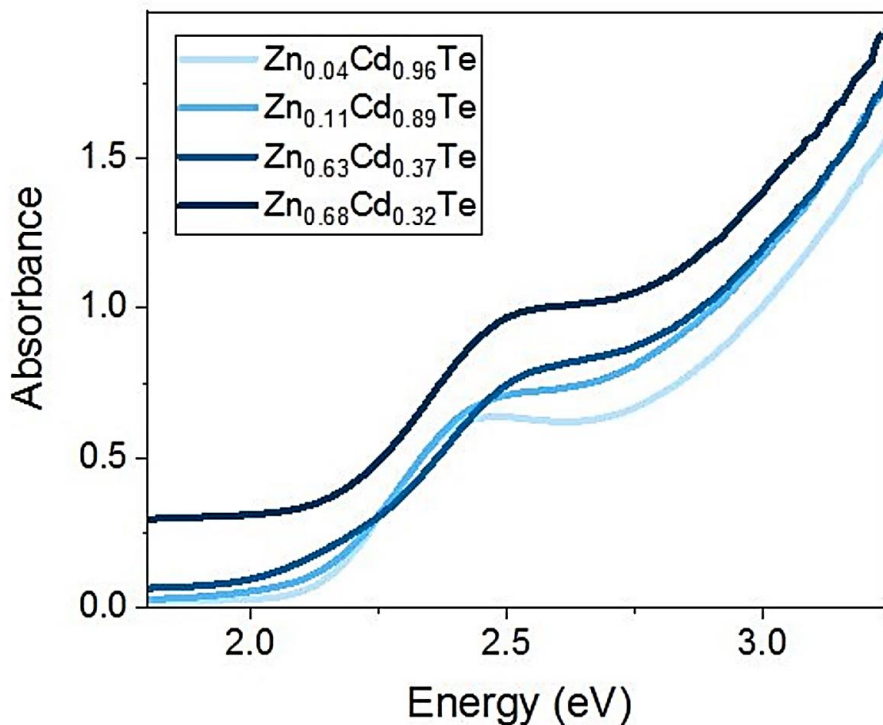
Figure S3. Zn1-xCdxTe absorbance spectra. Increasing zinc composition of Zn1-xCdxTe causes a blue shift in excitonic peaks
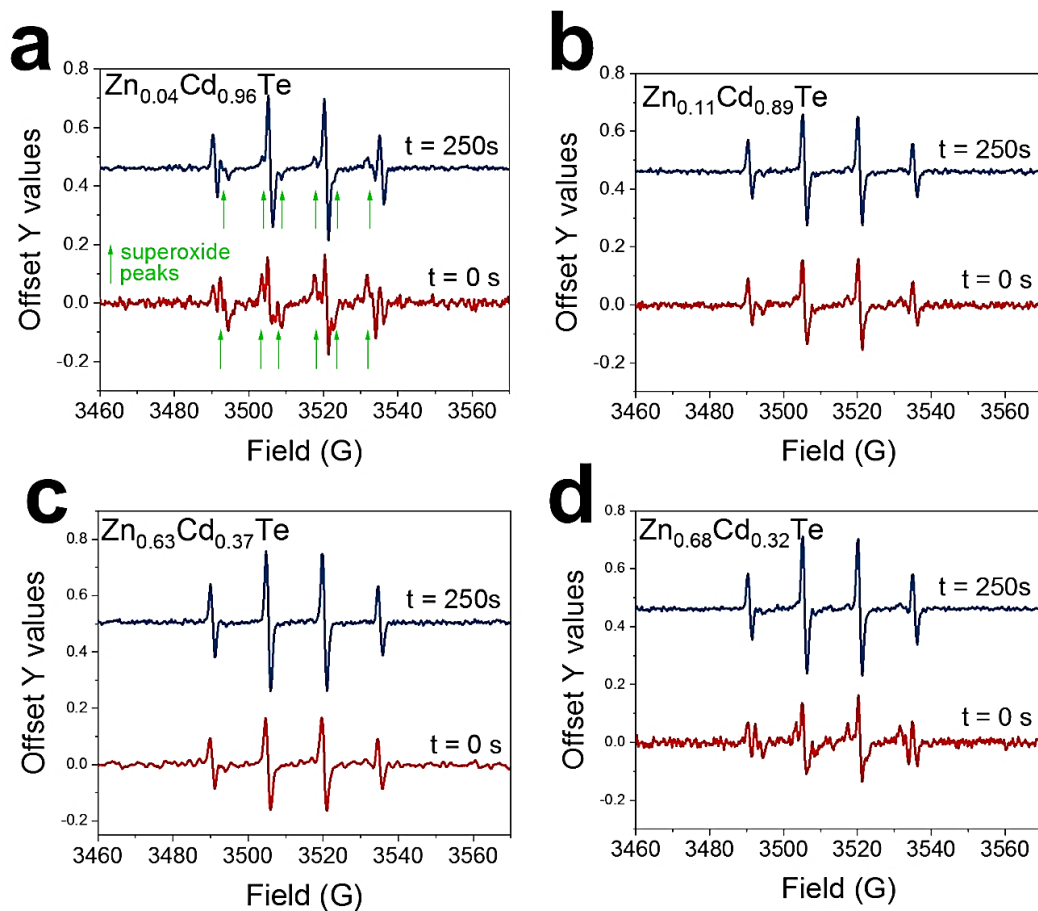
Figure S4. Zn1-xCdxTe shows superoxide generation in EPR. a-d) Zn1-xCdxTe QDs with progressively increasing zinc composition continues to show superoxide generation upon visible light activation. Note that direct superoxide detection (green arrows) is difficult given the short life time (~45s) of DMPO-OOH. Previous reports on this topic, as well as our own studies, have proven that DMPO-OH signal observed here (persistent at t = 250s) from hydroxyl radicals is a direct consequence of superoxide generation and dismutation to hydroxyl radicals.
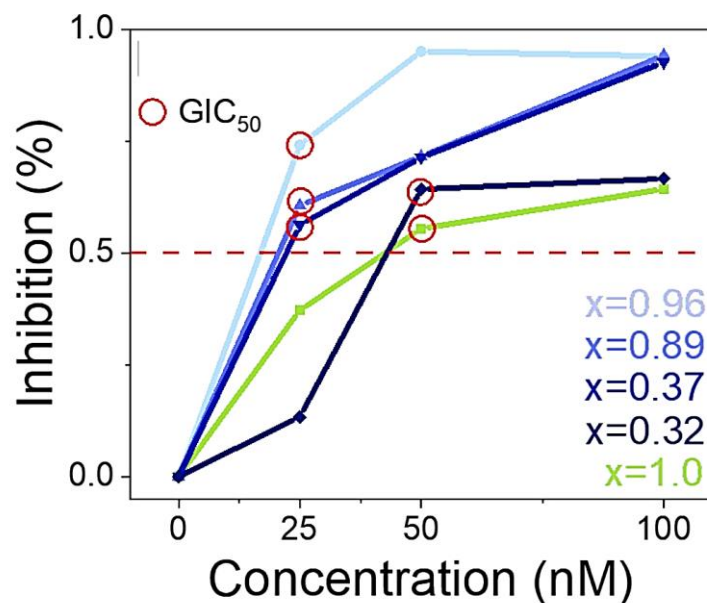
Figure S5. Determination GIC50 values individually for each QD of varying composition (x). First, inhibition at t=12 hours was calculated using Equation 3. We selected 12 hours as this timepoint showed equilibrated growth in our no-treatment control. Because we tested discrete values of QD dosage (12.5, 25, 50, 100 nM), we selected each GIC50 as the minimum dosage which demonstrated *at least* 50% inhibition
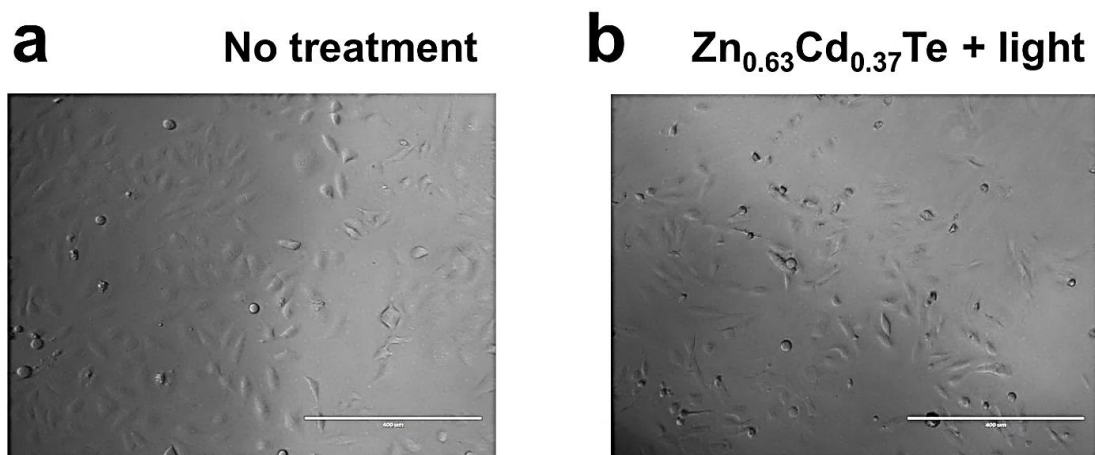
Figure S6. Zn1-xCdxTe QDs show negligible HeLa cell toxicity. a) 10x magnification images of HeLa cell growth after 18 hours of no treatment condition (negative control **b**) 10x

magnification images of HeLa cells treated with 50 nM Zn0.63Cd0.37Te QDs. Cells appear adherent and healthy compared to positive and negative controls. The scale bars show 400 μm. All conditions were exposed to the same light source for the same duration.

References

1. The review on antimicrobial resistance. *Tackling drug-resistant infections globally: Final reportandrecommendations*;2016.

2. Hirsch, L. R.; Stafford, R. J.; Bankson, J. A.; Sershen, S. R.; Rivera, B.; Price, R. E.; Hazle, J. D.; Halas, N. J.; West, J. L. Nanoshell-Mediated near-Infrared Thermal Therapy of Tumors under Magnetic Resonance Guidance. *Proc. Natl. Acad. Sci. U. S. A.* **2003**, *100* (23),13549–13554.

3. Huang, X.; El-Sayed, I. H.; Qian, W.; El-sayed, M. A. Cancer Cell Imaging and Photothermal Therapy in the near-Infrared Region by Using Gold Nanorods. *J. Am. Chem. Soc.* **2006**, *128* (6), 2115–2120.

4. Hamblin, M. R.; Hasan, T. Photodymamic Therapy: A New Antimicrobial Approach to Infectious Disease? *Photochem Photobiol Sci.* **2014**, *3* (5), 436–450.

5. Dai, T.; Huang, Y.-Y.; Hamblin, M. R. Photodynamic Therapy for Localized Infections –StateoftheArt.*NIHPublicAccess***2010**,*6*(617),170–188.

6. Courtney, C. M.; Goodman, S. M.; McDaniel, J. A.; Madinger, N. E.; Chatterjee, A.; Nagpal, P. Photoexcited Quantum Dots for Killing Multidrug-Resistant Bacteria. *Nat. Mater.***2016**,*15*(5), 529–534.

7. Courtney, C. M.; Goodman, S.; Nagy, T.; Levy, M.; Bhusal, P.; Madinger, Nancy E. Detweiler, C.; Nagpal, P.; Chatterjee, A. Potentiating Clinical Drug Resistant Bacteria via Stimuli-Activated Superoxide Generation. *Sci. Adv.* **2017**, *3* (October), e1701776.

8. Goodman, S. M.; Levy, M.; Li, F.-F.; Ding, Y.; Courtney, C. M.; Chowdhury, P. P.; Erbse, A.; Chatterjee, A.; Nagpal, P. Designing Superoxide-Generating Quantum Dots forSelectiveLight-ActivatedNanotherapy.*Front.Chem.***2018**,*6*,46.

9. Levy, M.; Courtney, C. M.; Chowdhury, P. P.; Ding, Y.; Grey, E. L.; Goodman, S. M.; Chatterjee, A.; Nagpal, P. Assessing Different Reactive Oxygen Species as Potential Antibiotics: Selectivity of Intracellular Superoxide Generation Using Quantum Dots. *ACS Appl.BioMater.***2018**.

10. Di Meo, S.; Reed, T. T.; Venditti, P.; Victor, V. M. *Role of ROS and RNS Sources in Physiological and Pathological Conditions*; 2016; Vol. 2016.

11. D'Autréaux, B.; Toledano, M. B. ROS as Signalling Molecules: Mechanisms That Generate Specificity in ROS Homeostasis. *Nat. Rev. Mol. Cell Biol.* **2007**, *8* (10), 813–824.

12. Choi, H. S.; Liu, W.; Misra, P.; Tanaka, E.; Zimmer, J. P.; Ipe, B. I.; Bawendi, M. G.; Frangioni, J. V. Renal Clearance of Quantum Dots. *Nat. Biotechnol.* **2007**, *25* (10), 1165–1170.

13. Xu, G.; Zeng, S.; Zhang, B.; Swihart, M. T.; Yong, K. T.; Prasad, P. N. New Generation Cadmium-Free Quantum Dots for Biophotonics and Nanomedicine. *Chem. Rev.* **2016**, *116* (19), 12234–12327.

14. Derfus, A. M.; Chan, W. C. W.; Bhatia, S. N. Probing the Cytotoxicity of Semiconductor QuantumDots.*NanoLett.***2004**,*4*(1),11–18.

15. Jing, L.; Kershaw, S. V.; Li, Y.; Huang, X.; Li, Y.; Rogach, A. L.; Gao, M. Aqueous Based Semiconductor Nanocrystals. *Chem. Rev.* **2016**, *116* (18), 10623–10730.

16. Du, J.; Li, X.; Wang, S.; Wu, Y.; Hao, X.; Xu, C.; Zhao, X. Microwave-Assisted Synthesis of Highly Luminescent Glutathione-Capped Zn1-xCdxTe Alloyed Quantum Dots with ExcellentBiocompatibility.*J.Mater.Chem.***2012**,*22*(22),11390.

17. Buettner, G. R. The Spin Trapping of Superoxide and Hydroxyl Free Radicals with Dmpo Dimethylpyrroline-N-Oxide):More About Iron. *Free Radic. Res. Commun.* **1993**, *19* (sup1),s79–s87.

18. Buettner, G. R. Spin Trapping: ESR Parameters of Spin Adducts. *Free Radic. Biol. Med.* **1987**,*3*(4),259–303.

19. Xu, S.; Wang, C.; Xu, Q.; Zhang, H.; Li, R.; Shao, H.; Lei, W.; Cui, Y. Key Roles of Solution pH and Ligands in the Synthesis of Aqueous ZnTe Nanoparticles. *Chem. Mater.* **2010**,*22*(21),5838–5844.

20. Cheng, T.; Li, D.; Li, J.; Ren, B.; Wang, G.; Cheng, J. Aqueous Synthesis of High Fluorescence ZnTe Quantum Dots. *J. Mater. Sci. Mater. Electron.* **2015**, *26* (6), 4062–4068.

21. Caldwell, R. S.; Fan, H. Y. Optical Properties of Tellurium and Selenium. *Phys. Rev.* **1959**, *114*(3),664–675.

22. Goodman, S. M.; Singh, V.; Ribot, J. C.; Chatterjee, A.; Nagpal, P. Multiple Energy Exciton Shelves in Quantum-Dot - DNA Nanobioelectronics. *J. Phys. Chem. Lett.* **2014**, *5*, 3909–3913.

23. Finkelstein, E.; Rosen, G. M.; Rauckman, E. J. Production of Hydroxyl Radical by Decomposition of Superoxide Spin-Trapped Adducts. *Molecular pharmacology*. 1982, pp262–265.

24. Buettner, G. R. On the Reaction of Superoxide with DMPO/.OOH. *Free Radic. Res Com* **1990**,*10*(1–2),11–15.

25. Cheng, J.; Li, D.; Cheng, T.; Ren, B.; Wang, G.; Li, J. Aqueous Synthesis of High Fluorescence CdZnTe Alloyed Quantum Dots. *J. Alloys Compd.* **2014**, *589*, 539–544.

26. Li, W.; Liu, J.; Sun, K.; Dou, H.; Tao, K. Highly Fluorescent Water Soluble CdxZn1-xTe Alloyed Quantum Dots Prepared in Aqueous Solution: One-Step Synthesis and the Alloy EffectofZn.*J.Mater.Chem.***2010**,*20*(11),2133.

27. Wang, Q.; Fang, T.; Liu, P.; Deng, B.; Min, X.; Li, X. Direct Synthesis of High-Quality Water-Soluble CdTe:Zn 2+ Quantum Dots. *Inorg. Chem.* **2012**, *51* (17), 9208–9213.

28. Matos, C. R. S.; Candido, L. P. M.; Souza, H. O.; da Costa, L. P.; Sussuchi, E. M.; Gimenez, I. F. Study of the Aqueous Synthesis, Optical and Electrochemical Characterization of Alloyed ZnxCd1-xTe Nanocrystals. *Mater. Chem. Phys.* **2016**, *178*, 104–111.

29. Liu, F. C.; Cheng, T. L.; Shen, C. C.; Tseng, W. L.; Chiang, M. Y. Synthesis of Cysteine Capped ZnxCd1-xSe Alloyed Quantum Dots Emitting in the Blue-Green Spectral Range. *Langmuir***2008**,*24*(5),2162–2167.

30. Imlay, J. A. Iron-Sulphur Clusters and the Problem with Oxygen. *Molecular Microbiology*.2006,pp1073–1082.

31. Imlay, J. A. Pathways of Oxidative Damage. *Annu. Rev. Microbiol.* **2003**, *57* (1), 395–418.

32. Hawkins, C. L.; Davies, M. J. Generation and Propagation of Radical Reactions on Proteins.*Biochim.Biophys.Acta-Bioenerg.***2001**,*1504*(2–3),196–219.

33. Davies, M. J. Singlet Oxygen-Mediated Damage to Proteins and Its Consequences. *Biochem.Biophys.Res.Commun.***2003**,*305*(3),761–770.

34. Imlay, J. A.; Fridovich, I. Assay of Metabolic Superoxide Production in Escherichia Coli. *J. Biol. Chem.* **1991**, *266* (11), 6957–6965.

Bibliography

D. Branton, D. W. Deamer, A. Marziali, H. Bayley, S. A. Benner, T. Butler, M. Di Ventra, S. Garaj, A. Hibbs, X. Huang, S. B. Jovanovich, P. S. Krstic, S. Lindsay, X. S. Ling, C. H. Mastrangelo, A. Meller, J. S. Oliver, Y. V Pershin, J. M. Ramsey, R. Riehn, G. V Soni, V. Tabard-Cossa, M. Wanunu, M. Wiggin, J. A. Schloss, *Nat. Biotechnol.* **2008**, *26*, 1146.

E. A. Pozzi, M. D. Sonntag, N. Jiang, J. M. Klingsporn, M. C. Hersam, R. P. Van Duyne, *ACS Nano* **2013**, *7*, 885.

E. L. Van Dijk, H. Auger, Y. Jaszczyszyn, C. Thermes, *Trends Genet.* **2014**, *30*, 418.

S. Goodwin, J. D. McPherson, W. R. McCombie, *Nat. Rev. Genet.* **2016**, *17*, 333.

R. A. Copeland, M. P. Moyer, V. M. Richon, *Oncogene* **2013**, *32*, 939.

P. Jares, D. Colomer, E. Campo, *Nat. Rev. Cancer* **2007**, *7*, 750.

S. K. Gire, A. Goba, K. G. Andersen, R. S. G. Sealfon, D. J. Park, L. Kanneh, S. Jalloh, M. Momoh, M. Fullah, G. Dudas, S. Wohl, L. M. Moses, N. L. Yozwiak, S. Winnicki, C. B. Matranga, C. M. Malboeuf, J. Qu, A. D. Gladden, S. F. Schaffner, X. Yang, P.-P. Jiang, M. Nekoui, A. Colubri, M. R. Coomber, M. Fonnie, A. Moigboi, M. Gbakie, F. K. Kamara, V. Tucker, E. Konuwa, S. Saffa, J. Sellu, A. A. Jalloh, A. Kovoma, J. Koninga, I. Mustapha, K. Kargbo, M. Foday, M. Yillah, F. Kanneh, W. Robert, J. L. B. Massally, S. B. Chapman, J. Bochicchio, C. Murphy, C. Nusbaum, S. Young, B. W. Birren, D. S. Grant, J. S. Scheiffelin, E. S. Lander, C. Happi, S. M. Gevao, A. Gnirke, A. Rambaut, R. F. Garry, S. H. Khan, P. C. Sabeti, *Science* **2014**, *345*, 1369.

P. W. Laird, *Nat. Rev. Cancer* **2003**, *3*, 253.

J. Deng, R. Shoemaker, B. Xie, A. Gore, E. M. LeProust, J. Antosiewicz-Bourget, D. Egli, N. Maherali, I.-H. Park, J. Yu, G. Q. Daley, K. Eggan, K. Hochedlinger, J. Thomson, W. Wang, Y. Gao, K. Zhang, *Nat. Biotechnol.* **2009**, *27*, 353.

E. Bailo, V. Deckert, *Angew. Chem., Int. Ed.* **2008**, *47*, 1658.

A. Barhoumi, D. Zhang, F. Tam, N. J. Halas, *J. Am.* **2008**, *130*, 5523.

L. Guerrini, Ž. Krpetić, D. Van Lierop, R. A. Alvarez-Puebla, D. Graham, *Angew. Chem., Int. Ed.* **2015**, *127*, 1160.

L. Xu, Z. Lei, J. Li, C. Zong, C. J. Yang, B. Ren, *J. Am. Chem. Soc.* **2015**, *137*, 5149.

J. Morla-Folch, H. N. Xie, P. Gisbert-Quilis, S. G. De Pedro, N. Pazos-Perez, R. A. Alvarez Puebla, L. Guerrini, *Angew. Chem., Int. Ed.* **2015**, *127*, 13854.

S. Lal, N. K. Grady, J. Kundu, C. S. Levin, J. B. Lassiter, N. J. Halas, *Chem. Soc. Rev.* **2008**, *37*, 898.

K. Kneipp, Y. Wang, H. Kneipp, L. T. Perelman, I. Itzkan, R. R. Dasari, M. S. Feld, *Phys. Rev.Lett.* **1997**, *78*, 1667.

E. J. Blackie, E. C. Le Ru, P. G. Etchegoin, *J. Am. Chem. Soc.* **2009**, *131*, 14466.

K. Nakamoto, *Handbook of Vibrational Spectroscopy*, John Wiley & Sons, Inc., Hoboken, NewJersey **2006**.

D. Zhang, K. F. Domke, B. Pettinger, *ChemPhysChem* **2010**, *11*, 1662.

R. Treffer, R. Böhme, T. Deckert-Gaudig, K. Lau, S. Tiede, X. Lin, V. Deckert, *Biochem. Soc.Trans.* **2012**, *40*, 609.

S. Najjar, D. Talaga, L. Schue, Y. Coffnier, S. Szunerits, R. Boukherroub, L. Servant, V. Rodriguez, S. Bonhommeau, *J.Phys.Chem.C* **2014**, *118*, 1174.

N. C. Lindquist, P. Nagpal, A. Lesuffleur, D. J. Norris, S. H. Oh, *Nano Lett.* **2010**, *10*, 1369.

P. Nagpal, N. C. Lindquist, S.-H. Oh, D. J. Norris, *Science* **2009**, *325*, 594.

N. C. Lindquist, P. Nagpal, K. M. McPeak, D. J. Norris, S.-H. Oh, *Rep. Prog. Phys.* **2012**, *75*, 36501.

C. Ropers, C. C. Neacsu, T. Elsaesser, M. Albrecht, M. B. Raschke, C. Lienau, *Nano Lett.* **2007**, *7*, 2784.

A. Bouhelier, M. Beversluis, A. Hartschuh, L. Novotny, *Phys. Rev. Lett.* **2003**, *90*, 13903.

Q. C. Sun, H. Mundoor, J. C. Ribot, V. Singh, I. I. Smalyukh, P. Nagpal, *Nano Lett.* **2013**, *14*,101.

N. A. Janunts, K. S. Baghdasaryan, K. V. Nerkararyan, B. Hecht, *Opt. Commun.* **2005**, *253*, 118.

M. Mathlouthi, A.-M. Seuvre, J. L. Koenig, *Carbohydr. Res.* **1984**, *131*, 1.

C. Otto, T. van den Tweel, F. de Mul, J. Greve, *J. Raman Spectrosc.* **1986**, *17*, 289.

J. De Gelder, K. De Gussem, P. Vandenabeele, L. Moens, *J. Raman Spectrosc.* **2007**, *38*, 1133.

R. Treffer, X. Lin, E. Bailo, T. Deckert-Gaudig, V. Deckert, *Beilstein J. Nanotechnol.* **2011**,*2*, 628.

M. Mathlouthi, A.-M. Seuvre, J. L. Koenig, *Carbohydr. Res.* **1984**, *134*, 23.

M. Mathlouthi, A.-M. Seuvre, J. L. Koenig, *Carbohydr. Res.* **1986**, *146*, 1.

M. Mathlouthi, A.-M. Seuvre, J. L. Koenig, *Carbohydr. Res.* **1984**, *146*, 15.

A.-M. Seuvre, M. Mathlouthi, *Carbohydr. Res.* **1987**, *169*, 83.

A. Barhoumi, N. J. Halas, *J. Phys. Chem. Lett.* **2011**, *2*, 3118.

F. Pashaee, M. Tabatabaei, F. A. Caetano, S. S. G. Ferguson, F. Lagugné-Labarthet, *Analyst* **2016**,*141*,3251.

S. Afsari, L. E. Korshoj, G. R. Abel Jr., S. Khan, A. Chatterjee, P. Nagpal, *ACS Nano* **2017**, *11*, 11169.

Di Meo, S.; Reed, T. T.; Venditti, P.; Victor, V. M. Role of ROS and RNS Sources in Physiological and Pathological Conditions. Oxid.Med.Cell.Longevity 2016, 1245049, 1-44.

D'Autreaux, B.; Toledano, M. B. ROS as Signalling Molecules:́ Mechanisms That Generate Specificity in ROS Homeostasis. Nat. Rev. Mol. Cell Biol. 2007, 8 (10), 813-824.

Crack, J. C.; Green, J.; Cheesman, M. R.; Le Brun, N. E.; Thomson, A. J. Superoxide-Mediated Amplification of the Oxygen Induced Switch from [4Fe-4S] to [2Fe-2S] Clusters in the

Transcriptional Regulator FNR. Proc. Natl. Acad. Sci. U. S. A. 2007, 104 (7), 2092-2097.

Zheng, M.; Aslund, F.; Storz, G. Activation of the OxyR Transcription Factor by Reversible Disulfide Bond Formation. Science 1998, 279 (March), 1718-1722.

Lee, J. W.; Helmann, J. D. The PerR Transcription Factor Senses H2O2 by Metal-Catalysed HistidineOxidation.Nature2006,440(7082),363-367.

Fuangthong, M.; Atichartpongkul, S.; Mongkolsuk, S.; Helmann, J. D. OhrR Is a Repressor of ohrA, a Key Organic Hydroperoxide Resistance Determinant in Bacillus Subtilis. J. Bacteriol. 2001,183(14),4134-4141.

Bogdan, C. Nitric Oxide and the Immune Response. Nat. Immunol. 2001, 2 (10), 907-916.

Vatansever, F.; de Melo, W. C. M. A.; Avci, P.; Vecchio, D.; Sadasivam, M.; Gupta, A.; Chandran, R.; Karimi, M.; Parizotto, N. A.; Yin, R.; Tegos, G. P.; Hamblin, M. R. Antimicrobial Strategies Centered around Reactive Oxygen Species - Bactericidal Antibiotics, Photodynamic Therapy, and beyond. FEMS Microbiol. Rev. 2013, 37 (6),955-989.

Davies, M. J. The Oxidative Environment and Protein Damage. Biochim. Biophys. Acta, ProteinsProteomics2005,1703(2),93-109.

Davies, M. J. Singlet Oxygen-Mediated Damage to Proteins and Its Consequences. Biochem. Biophys. Res. Commun. 2003, 305 (3), 761-770.

Finkel, T.; Holbrook, N. J. Oxidants, Oxidative Stress and the Biology of Ageing. Nature 2000,408(6809),239-247.

Radi, R. Peroxynitrite, a Stealthy Biological Oxidant. J. Biol. Chem. 2013, 288 (37), 26464-26472.

Pacher, P.; Beckman, J. S.; Liaudet, L. Nitric Oxide and Peroxynitrite in Health and Disease. Physiol.Rev.2007,87(1),315-424.

Candeias, L. P.; Wardman, P. Introduction to Fenton Chemistry. Radiat. Res. 1996, 145 (5), 523-531.

Bielski, B. H. J.; Allen, A. O.; Schwarz, H. A. Mechanism of the Disproportionation of Superoxide Radicals. J. Am. Chem. Soc. 1981, 103 (12), 3516-3518.

McCord, J. M., Fridovich, I. Superoxide Dismutase. Methods Enzymol. 1969, 349.

Pryor, W. A.; Squadrito, G. L. The Chemistry of Peroxynitrite: A Product from the Reaction of Nitric Oxide with Superoxide. Am. J. Physiol. 1995, 268, L699-722.

Hirsch, L. R.; Stafford, R. J.; Bankson, J. A.; Sershen, S. R.; Rivera, B.; Price, R. E.; Hazle, J. D.; Halas, N. J.; West, J. L. NanoshellMediated near-Infrared Thermal Therapy of Tumors under Magnetic Resonance Guidance. Proc. Natl. Acad. Sci. U. S. A. 2003, 100 (23), 13549-13554.

Huang, X.; El-Sayed, I.; Qian, W.; El-sayed, M. A. Cancer Cell Imaging and Photothermal Therapy in the Near-Infrared Region by Using Gold Nanorods. J. Am. Chem. Soc. 2006, 128 (3), 2115-2120

Hamblin, M. R.; Hasan, T. Photodymamic Therapy: A New Antimicrobial Approach to Infectious Disease? Photochem. Photobiol. Sci. 2004, 3 (5), 436-450.

Dai, T.; Huang, Y.-Y.; Hamblin, M. R. Photodynamic Therapy for Localized Infections - State of the Art. Photodiagn. Photodyn. Ther. 2009, 6, 170-188.

Lu, K.; He, C.; Lin, W. J. Am. Chem. Soc. 2014, 136, 2-5.

Lu, K.; He, C.; Lin, W. A Chlorin-Based Nanoscale MetalOrganic Framework for Photodynamic Therapy of Colon Cancers. J. Am. Chem. Soc. 2015, 137 (24), 7600-7603.

Toufektsian, M.; Boucher, F.; Tanguy, S.; Morel, S.; Leiris, J. Cardiac Toxicity of Singlet Oxygen: Implication in Reperfusion Injury. Antioxid. Redox Signaling 2001, 3 (1), 63-69.

DeRosa, M. C.; Crutchley, R. J. Photosensitized Singlet Oxygen and Its Applications. Coord. Chem.Rev.2002,233-234,351-371.

Jarvi, M. T.; Niedre, M. J.; Patterson, M. S.; Wilson, B. C. Singlet Oxygen Luminescence Dosimetry (SOLD) for Photodynamic Therapy: Current Status, Challenges and Future Prospects. Photochem.Photobiol.2006,82,1198-1210.

Bonnett, R. Photosensitizers of the Porphyrin and Phthalocyanine Series for Photodynamic Therapy.Chem.Soc.Rev.1995,24(1),19-33.

Courtney, C. M.; Goodman, S. M.; McDaniel, J. A.; Madinger, N. E.; Chatterjee, A.; Nagpal, P. Photoexcited Quantum Dots for Killing Multidrug-Resistant Bacteria. Nat. Mater. 2016, 15

(5),   529-534.

Choi, H. S.; Liu, W.; Misra, P.; Tanaka, E.; Zimmer, J. P.; Ipe, B. I.; Bawendi, M. G.; Frangioni, J. V. Renal Clearance of Quantum Dots. Nat. Biotechnol. 2007, 25 (10), 1165-1170.

Chan, W. C. W.; Nie, S. Quantum Dot Bioconjugates for Ultrasensitive Nonisotopic Detection.Science1998,281,2016-2018.

Farokhzad, O. C.; Karp, J. M.; Langer, R. Nanoparticle- aptamer Bioconjugates for Cancer Targeting.   Expert   Opin.   Drug   Delivery   2006,   3   (3),   311-324.

Ipe, B. I.; Lehnig, M.; Niemeyer, C. M. On the Generation of Free Radical Species from QuantumDots.Small2005,1(7),706-709.

Harbour, J. R.; Hair, M. L. Superoxide Generation in the Photolysis of Aqueous Cadmium Sulfide Dispersions. Detection by Spin Trapping. J. Phys. Chem. 1977, 81 (18), 1791-1793.

Buettner, G. R.; Mason, R. P. Spin-Trapping Methods for Detecting Superoxide and Hydroxyl Free Radicals in Vitro and in Vivo. Methods Enzymol. 1990, 186 (4), 127-133.

Imlay, J. A. Pathways of Oxidative Damage. Annu. Rev. Microbiol. 2003, 57 (1), 395-418.

Imlay, J. A.; Linn, S.; Imlay, J. A.; Linn, S. Science 2016, 240 (4857), 1302-1309.

Nakamura, J.; Purvis, E. R.; Swenberg, J. A. Micromolar Concentrations of Hydrogen Peroxide Induce Oxidative DNA Lesions More Efficiently than Millimolar Concentrations in Mammalian   Cells.   Nucleic   Acids   Res.   2003,   31   (6),   1790-1795.

Li, C.-Q.; Pang, B.; Kiziltepe, T.; Trudel, L. J.; Engelward, B. P.; Dedon, P. C.; Wogan, G. N. Threshold Effects of Nitric OxideInduced Toxicity and Cellular Responses in Wild-Type and p53-Null Human Lymphoblastoid Cells. Chem. Res. Toxicol. 2006, 19 (3), 399-406.

Courtney, C. M.; Goodman, S.; Nagy, T.; Levy, M.; Bhusal, P.; Madinger, N. E.; Detweiler, C.; Nagpal, P.; Chatterjee, A. Potentiating Clinical Drug Resistant Bacteria via Stimuli-Activated   Superoxide   Generation.   Sci.   Adv.   2017,   3   (10),   e1701776.

Finkelstein, E. L. I. D.; Surgery, R. G.; Rosen, O. D. M.; Durham, R.; Carolina, N. Production of hydroxyl radical by decomposition of superoxide spin-trapped adducts. Mol. Pharmacol.

1982, 262-265.

Goodman, S. M.; Levy, M.; Li, F.-F.; Ding, Y.; Courtney, C. M.; Chowdhury, P. P.; Erbse, A.; Chatterjee, A.; Nagpal, P. Designing Superoxide-Generating Quantum Dots for Selective Light-Activated Nanotherapy. Front. Chem. 2018, 6 (46), 1-12.

Yamazaki, I.; Piette, L.; Grover, T. A. Kinetic Studies on Spin Trapping of Superoxide and Hydroxyl Radicals Generated Reductase Paraquat Systems. J. Biol. Chem. 1990, 265 (2), 652-659.

Imlay, J. A. The Molecular Mechanisms and Physiological Consequences of Oxidative Stress: Lessons from a Model Bacterium. Nat. Rev. Microbiol. 2013, 11 (7), 443-454.

Imlay, J. A. Iron-Sulphur Clusters and the Problem with Oxygen. Mol. Microbiol. 2006, 59 (4),1073-1082.

Cabelli, D.; Bielski, B. H. J. Kinetics and Mechanism for the Oxidation of Ascorbic Acid/Ascorbate by HO2/O2- Radicals. J. Phys. Chem. 1983, 87, 1809-1812.

Mizuno, M.; Nishitani, Y. Scavenging Rate Constants of Hydrophilic Antioxidants against Multiple Reactive Oxygen Species. J. Clin. Biochem. Nutr. 2013, 52 (May), 202-207.

Sato, Y.; Itagaki, S.; Kurokawa, T.; Ogura, J.; Kobayashi, M.; Hirano, T.; Sugawara, M.; Iseki, K. In Vitro and in Vivo Antioxidant Properties of Chlorogenic Acid and Caffeic Acid. Int. J.Pharm.2011,403(1-2),136-138.

Buxton, G. V.; Greenstock, C. L.; Helman, W. P.; Ross, A. B. Critical Review of Rate Constants for Reactions of Hydrated Electrons, Hydrogen Atoms and Hydroxyl Radicals (·OH/·O- In Aqueous Solution. J. Phys. Chem. Ref. Data 1988, 17 (2), 513-886.

Sawyer, D. T.; Valentine, J. S. How Super Is Superoxide? Acc. Chem. Res. 1981, 14 (12), 393-400.

Sawyer, D. T.; Valentine, J. S. How Innocuous Is Superoxide? Comments. Acc. Chem. Res. 1982,15(7),200.

Fridovich, I. How Innocuous Is Superoxide? Comments. Acc. Chem. Res. 1982, 15 (7), 200.

Carlioz, A; Touati, D. Isolation of Superoxide Dismutase Mutants in Escherichia Coli: Is Superoxide Dismutase Necessary for Aerobic Life? EMBO J. 1986, 5 (3), 623-630.

Iglewski, B.; Clark, V. Molecular Basis of Bacterial Pathogenesis; 1990.

Pan, X.; Yang, Y.; Zhang, J.-R. Molecular Basis of Host Specificity in Human Pathogenic Bacteria. Emerging Microbes Infect. 2014, 3 (3), e23.

Lancaster, J.R. Nitric Oxide: Principles and Actions; 1996.

Imlay, J. A.; Fridovich, I. Assay of Metabolic Superoxide Production in Escherichia Coli. J. Biol.Chem.1991,266(11),6957-6965.

Winterbourn, C. C. Reconciling the Chemistry and Biology of Reactive Oxygen Species. Nat. Chem.Biol.2008,4(5),278-286.

Krumova, K.; Cosa, G. Chapter I: Overview of Reactive Oxygen Species. Singlet Oxyg. Appl. Biosci.Nanosci.2016,1(1),1-21.

Skovsen, E.; Snyder, J. W.; Lambert, J. D. C.; Ogilby, P. R. J. Phys. Chem. B 2005, 109, 8570-8573.

Ragas, X.; Agut, M.; Nonell, S. Singlet Oxygen in Escherichià Coli: New Insights for Antimicrobial Photodynamic Therapy. Free Radical Biol. Med. 2010, 49 (5), 770-776.

Gort, A. S.; Imlay, J. A. Balance between Endogenous Superoxide Stress and Antioxidant Defenses. J. Bacteriol. 1998, 180 (6), 1402-1410.

Apel, K., and Hirt, H. (2004). Reactive oxygen species: metabolism, oxidative stress, and signal transduction. *Annu. Rev. Plant Biol.* 55, 373–399.doi:10.1146/annurev.arplant.55.031903.141701

Bonnett, R. (1995). Photosensitizers of the porphyrin and phthalocyanine series for photodynamic therapy. *Chem. Soc. Rev.* 24, 19–33.doi:10.1039/cs9952400019

Buettner, G. R. (1987). Spin trapping: esr parameters of spin adducts. *Free Radic. Biol. Med.* 3, 259–303. doi: 10.1016/S0891-5849(87)80033-3

Chan, W., Shiao, N., and Lu, P. (2006). CdSe quantum dots induce apoptosis in human neuroblastoma cells via mitochondrial-dependent pathways and inhibition of survival signals. *Toxicol. Lett.* 167, 191–200. doi:10.1016/j.toxlet.2006.09.007

Cho, S. J., Maysinger, D., Jain, M., Röder, B., Hackbarth, S., and Winnik, F. M. (2007). Long-Term exposure to CdTe quantum dots causes functional impairments in live cells. *Langmuir* 23,1974–1980.doi:10.1021/la060093j

Choi, H. S., Liu, W., Misra, P., Tanaka, E., Zimmer, J. P., Ipe, B. I., et al. (2007). Renal clearance of quantum dots. *Nat. Biotechnol.* 25, 1165–1170. doi: 10.1038/nbt1340

Connor, E. E., Mwamuka, J., Gole, A., Murphy, C. J., and Wyatt, M. D. (2005). Gold nanoparticles are taken up by human cells but do not cause acute cytotoxicity. *Small* 1, 325–327.doi:10.1002/smll.200400093

Courtney, C. M., Goodman, S. M., McDaniel, J. A., Madinger, N. E., Chatterjee, A., and Nagpal, P. (2016). Photoexcited quantum dots for killing multidrugresistant bacteria. *Nat. Mater.* 15,529–534.doi:10.1038/nmat4542

Courtney, C. M., Goodman, S. M., Nagy, T. A., Levy, M., Bhusal, P., Madinger, N. E., et al. (2017). Potentiating antibiotics in drug-resistant clinical isolates via stimuli-activated superoxide generation. *Sci. Adv.* 3:e1701776. doi: 10.1126/sciadv.1701776

Dai, T., Huang, Y.-Y., and Hamblin, M. R. (2010). Photodynamic therapy for localized infections – state of the art. *Photodiagn. Photodyn. Ther*. 6, 170–188. doi: 10.1016/j.pdpdt.2009.10.008

Dumas, E., Gao, C., Suffern, D., Bradforth, S. E., Dimitrijevic, N. M., and Nadeau, J. L. (2010). Interfacial charge transfer between CdTe quantum dots and gram-negative vs gram positive bacteria. *Environ. Sci. Technol.* 44, 1464–1470. doi: 10.1021/es902898d

Feng, Z. V., Gunsolus, I. L., Qiu, T. A., Hurley, K. R., Nyberg, L. H., Frew, H., et al. (2015). Impacts of gold nanoparticle charge and ligand type on surface binding and toxicity to gram-negative and gram-positive bacteria. *Chem. Sci.* 6, 5186–5196. doi: 10.1039/C5SC00792E

Finkelstein, E., Rosen, G. M., and Rauckman, E. J. (1980). Spin trapping of superoxide and hydroxyl radical: practical aspects. *Arch. Biochem. Biophys.* 200, 1–16. doi: 10.1016/0003-9861(80)90323-9

Gao, L., Liu, R., Gao, F., Wang, Y., Jiang, X., and Gao, X. (2014). Plasmon Mediated generation of reactive oxygen species from near-infrared light excited gold nanocages for photodynamic therapy *in vitro*. *ACS Nano* 8, 7260–7271.doi: 10.1021/nn502325j

Gao, X., Cui, Y., Levenson, R. M., Chung, L. W. K., and Nie, S. (2004). *In vivo* cancer targeting and imaging with semiconductor quantum dots. *Nat. Biotechnol.* 22, 969–976. doi:10.1038/nbt994

Glozman, A., Lifshitz, E., Hoppe, K., Rogach, A. L., Welllr, H., and Echymüller, A. (2001). Optically detected magnetic resonance of thiol-capped CdTe nanocrystals. *Isr. J. Chem.*41,39–44.doi:10.1560/GVFT-60DT-8Y0E-7DR9

Gomes, S. A. O., Vieira, C. S., Almeida, D. B., Santos-Mallet, J. R., MennaBarreto, R. F. S., Cesar, C. L., et al. (2011). CdTe and CdSe quantum dots cytotoxicity: a comparative study on microorganisms. *Sensors* 11, 11664–11678. doi: 10.3390/s111211664

Grabolle, M., Spieles, M., Lesnyak, V., Gaponik, N., Eychmüller, A., and ReschGenger, U. (2009). Determination of the fluorescence quantum yield of quantum dots: suitable procedures and achievable uncertainties. *Anal. Chem.*81, 6285–6294. doi: 10.1021/ac900308v

Hamblin, M. R., and Hasan, T. (2014). Photodymamic therapy: a new antimicrobial approach to infectious disease? *Photochem. Photobiol. Sci.* 3, 436–450. doi: 10.1039/b311900a

World Health Organization (2018). *WHO Antimicrobial Resistance.* Available Online at: http://www.who.int/mediacentre/factsheets/fs194/en/

Hirsch, L. R., Stafford, R. J., Bankson, J. A., Sershen, S. R., Rivera, B., Price, R. E., et al. (2003). Nanoshell-Mediated near-infrared thermal therapy of tumors under magnetic resonance guidance. *Proc. Natl. Acad. Sci. U.S.A.* 100, 13549–13554. doi: 10.1073/pnas.2232479100

Huang, X., El-Sayed, I. H., Qian, W., and El-Sayed, M. A. (2006). Cancer cell imaging and photothermal therapy in the near-infrared region by using gold nanorods. *J. Am. Chem. Soc.*128,2115–2120.doi:10.1021/ja057254a

Imlay, J. A. (2013). The molecular mechanisms and physiological consequences of oxidative stress: lessons from a model bacterium. *Nat. Rev. Microbiol.* 11, 443–454. doi: 10.1038/nrmicro3032

Ipe, B. I., Lehnig, M., and Niemeyer, C. M. (2005). On the generation of free radical species from quantum dots. *Small* 1, 706–709. doi: 10.1002/smll.200500105

Jarvi, M. T., Niedre, M. J., Patterson, M. S., and Wilson, B. C. (2006). Singlet Oxygen Luminescence Dosimetry (SOLD) for photodynamic therapy: current status , challenges and future prospects. *Photochem. Photobiol.* 82, 1198–1210. doi: 10.1562/2006-05-03-IR-891

Katari, J. E. B., Colvin, V. L., and Alivisatos, A. P. (1994). X-ray photoelectron spectroscopy of CdSe nanocrystals with applications to studies of the nanocrystal surface. *J.Phys.Chem.*98,4109–4117.doi:10.1021/j100066a034

Kirchner, C., Liedl, T., Kudera, S., Pellegrino, T., Javier, A. M., Gaub, H. E., et al. (2005). Cytotoxicity of colloidal CdSe and CdSe/ZnS nanoparticles. *Nano Lett.* 5, 331–338. doi: 10.1021/nl047996m

Lovric, J., Bazzi, H. S., Cuie, Y., Fortin, G. R. A., Winnik, F. M., and ´Maysinger, D. (2005). Differences in subcellular distribution and toxicity of green and red emitting CdTe quantum dots. *J. Mol. Med.* 83, 377–385. doi: 10.1007/s00109-004-0629-x

Lu, Z., Li, C. M., Bao, H., Qiao, Y., Toh, Y., and Yang, X. (2008). Mechanism of antimicrobial activity of CdTe quantum dots. *Langmuir* 24, 5445–5452. doi: 10.1021/la704075r

Ma, J., Chen, J. Y., Idowu, M., and Nyokong, T. (2008). Generation of singlet oxygen via the composites of water-soluble thiol-capped CdTe quantum dotssulfonated aluminum phthalocyanines. *J. Phys. Chem. B* 112, 4465–4469. doi: 10.1021/jp711537j

Medintz, I. L., Uyeda, H. T., Goldman, E. R., and Mattoussi, H. (2005). Quantum dot bioconjugates for imaging, labelling and sensing. *Nat. Mater.* 4, 435–446. doi: 10.1038/nmat1390

Michalet, X., Pinaud, F. F., Bentolil, L. A., Tsay, J. M., Doose, S., Li, J. J., et al. (2005). Quantum dots for live cells, *in vivo* imaging and diagnostics. *Science* 307, 538–545. doi: 10.1126/science.1104274

Nagy, A., Steinbrück, A., Gao, J., Doggett, N., Hollingsworth, J. A., and Iyer, R. (2012). Comprehensive analysis of the effects of cdse quantum dot size, surface charge, and functionalization on primary human lung cells. *ACS Nano* 6, 4748–4762. doi: 10.1021/nn204886b

Pitout, J. D. D., and Laupland, K. B. (2008). Extended-Spectrum β-LactamaseProducing Enterobacteriaceae: an emergin public-health concern. *Lancet* 8, 159–166. doi: 10.1016/S1473-3099(08)70041-0

Reynolds, T. S., Courtney, C. M., Erickson, K. E., Wolfe, L. M., Chatterjee, A., Nagpal, P., et al. (2017). ROS mediated selection for increased NADPH availability in *Escherichia Coli*. *Biotechnol. Bioeng.* 114, 2685–2689. doi: 10.1002/bit.26385

Schneider, R., Wolpert, C., Guilloteau, H., Balan, L., Lambert, J., and Merlin, C. (2009). The exposure of bacteria to CdTe-core quantum dots: the importance of surface chemistry on cytotoxicity. *Nanotechnology* 20:225101. doi: 10.1088/0957-4484/20/22/225101

Thannickal, V. J., and Fanburg, B. L. (2000). Reactive oxygen species in cell signaling. *Am. J. Physiol. Lung Cell. Mol. Physiol.* 279, L1005–L1028. doi: 10.1152/ajplung.2000.279.6.L1005

Trachootham, D., Alexandre, J., and P, H. (2009). Targeting cancer cells by ROSmediated mechanisms: a radical therapeutic approach? *Nat. Rev. Drug Discov.* 8, 579–591. doi: 10.1038/nrd2803

Tsay, J. M., Pflughoefft, M., Bentolila, L. A., and Weiss, S. (2004). Hybrid approach to the synthesis of highly luminescent CdTe/ZnS and CdHgTe/ZnS nanocrystals. *J. Am. Chem.Soc.*126,1926–1927.doi:10.1021/ja039227v

Valko, M., Leibfritz, D., Moncol, J., Cronin, M. T. D., Mazur, M., and Telser, J. (2007). Free radicals and antioxidants in normal physiological functions and human disease. *Int. J. Biochem. Cell Biol.* 39, 44–84. doi: 10.1016/j.biocel.2006.07.001

Wondrak, G. T. (2009). Redox-Directed cancer therapeutics: molecular mechanisms and opportunities. *Antioxid. Redox Signal.* 11, 3013–3069. doi: 10.1089/ars.2009.2541

Yu, B. P. (1994). Cellular defenses against damage from reactive oxygen species. *Physiol.Rev.*74,139–162.doi:10.1152/physrev.1994.74.1.139

Yu, W. W., Qu, L., Guo, W., and Peng, X. (2003). Experimental determination of the extinction coefficient of CdTe, CdSe, and CdS nanocrystals. *Chem. Mater.* 15, 2854–2860. doi:10.1021/cm034081k

Zeng, C., Ramos-Ruiz, A., Field, J. A., and Sierra-Alvarez, R. (2015). Cadmium Telluride (CdTe) and Cadmium Selenide (CdSe) leaching behavior and surface chemistry in response to pH and O2. *J. Environ. Manage.* 154, 78–85. doi: 10.1016/j.jenvman.2015.02.033

Zwietering, M. H., Jongenburger, I., Rombouts, F. M., and Vant Riet, K. (1990). Modeling of the bacterial growth curve. *Appl. Environ. Microbiol.* 56, 1875–1881.

The review on antimicrobial resistance. *Tackling drug-resistant infections globally: Final reportandrecommendations*;2016.

Hirsch, L. R.; Stafford, R. J.; Bankson, J. A.; Sershen, S. R.; Rivera, B.; Price, R. E.; Hazle, J. D.;

Halas, N. J.; West, J. L. Nanoshell-Mediated near-Infrared Thermal Therapy of Tumors under Magnetic Resonance Guidance. *Proc. Natl. Acad. Sci. U. S. A.* **2003**, *100* (23), 13549–13554.

Huang, X.; El-Sayed, I. H.; Qian, W.; El-sayed, M. A. Cancer Cell Imaging and Photothermal Therapy in the near-Infrared Region by Using Gold Nanorods. *J. Am. Chem. Soc.* **2006**, *128* (6), 2115–2120.

Hamblin, M. R.; Hasan, T. Photodymamic Therapy: A New Antimicrobial Approach to Infectious Disease? *Photochem Photobiol Sci.* **2014**, *3* (5), 436–450.

Dai, T.; Huang, Y.-Y.; Hamblin, M. R. Photodynamic Therapy for Localized Infections – State of the Art. *NIH Public Access* **2010**, *6* (617), 170–188.

Courtney, C. M.; Goodman, S. M.; McDaniel, J. A.; Madinger, N. E.; Chatterjee, A.; Nagpal, P. Photoexcited Quantum Dots for Killing Multidrug-Resistant Bacteria. *Nat. Mater.* **2016**, *15* (5), 529–534.

Courtney, C. M.; Goodman, S.; Nagy, T.; Levy, M.; Bhusal, P.; Madinger, Nancy E. Detweiler, C.; Nagpal, P.; Chatterjee, A. Potentiating Clinical Drug Resistant Bacteria via Stimuli-Activated Superoxide Generation. *Sci. Adv.* **2017**, *3* (October), e1701776.

Goodman, S. M.; Levy, M.; Li, F.-F.; Ding, Y.; Courtney, C. M.; Chowdhury, P. P.; Erbse, A.; Chatterjee, A.; Nagpal, P. Designing Superoxide-Generating Quantum Dots for Selective Light-Activated Nanotherapy. *Front. Chem.* **2018**, *6*, 46.

Levy, M.; Courtney, C. M.; Chowdhury, P. P.; Ding, Y.; Grey, E. L.; Goodman, S. M.; Chatterjee, A.; Nagpal, P. Assessing Different Reactive Oxygen Species as Potential Antibiotics: Selectivity of Intracellular Superoxide Generation Using Quantum Dots. *ACS Appl. Bio Mater.* **2018**.

Di Meo, S.; Reed, T. T.; Venditti, P.; Victor, V. M. *Role of ROS and RNS Sources in Physiological and Pathological Conditions*; 2016; Vol. 2016.

D'Autréaux, B.; Toledano, M. B. ROS as Signalling Molecules: Mechanisms That Generate Specificity in ROS Homeostasis. *Nat. Rev. Mol. Cell Biol.* **2007**, *8* (10), 813–824.

Choi, H. S.; Liu, W.; Misra, P.; Tanaka, E.; Zimmer, J. P.; Ipe, B. I.; Bawendi, M. G.; Frangioni, J. V. Renal Clearance of Quantum Dots. *Nat. Biotechnol.* **2007**, *25* (10), 1165–1170.

Xu, G.; Zeng, S.; Zhang, B.; Swihart, M. T.; Yong, K. T.; Prasad, P. N. New Generation Cadmium-Free Quantum Dots for Biophotonics and Nanomedicine. *Chem. Rev.* **2016**, *116* (19), 12234–12327.

Derfus, A. M.; Chan, W. C. W.; Bhatia, S. N. Probing the Cytotoxicity of Semiconductor Quantum Dots. *Nano Lett.* **2004**, *4* (1), 11–18.

Jing, L.; Kershaw, S. V.; Li, Y.; Huang, X.; Li, Y.; Rogach, A. L.; Gao, M. Aqueous Based Semiconductor Nanocrystals. *Chem. Rev.* **2016**, *116* (18), 10623–10730.

Du, J.; Li, X.; Wang, S.; Wu, Y.; Hao, X.; Xu, C.; Zhao, X. Microwave-Assisted Synthesis of Highly Luminescent Glutathione-Capped Zn1-xCdxTe Alloyed Quantum Dots with Excellent Biocompatibility.*J.Mater.Chem.***2012**,*22*(22),11390.

Buettner, G. R. The Spin Trapping of Superoxide and Hydroxyl Free Radicals with Dmpo Dimethylpyrroline-N-Oxide):More About Iron. *Free Radic. Res. Commun.* **1993**, *19* (sup1), s79–s87.

Buettner, G. R. Spin Trapping: ESR Parameters of Spin Adducts. *Free Radic. Biol. Med.* **1987**,*3*(4),259–303.

Xu, S.; Wang, C.; Xu, Q.; Zhang, H.; Li, R.; Shao, H.; Lei, W.; Cui, Y. Key Roles of Solution pH and Ligands in the Synthesis of Aqueous ZnTe Nanoparticles. *Chem. Mater.* **2010**, *22* (21), 5838–5844.

Cheng, T.; Li, D.; Li, J.; Ren, B.; Wang, G.; Cheng, J. Aqueous Synthesis of High Fluorescence ZnTe Quantum Dots. *J. Mater. Sci. Mater. Electron.* **2015**, *26* (6), 4062–4068.

Caldwell, R. S.; Fan, H. Y. Optical Properties of Tellurium and Selenium. *Phys. Rev.* **1959**, *114*(3),664–675.

Goodman, S. M.; Singh, V.; Ribot, J. C.; Chatterjee, A.; Nagpal, P. Multiple Energy Exciton Shelves in Quantum-Dot - DNA Nanobioelectronics. *J. Phys. Chem. Lett.* **2014**, *5*, 3909–3913.

Finkelstein, E.; Rosen, G. M.; Rauckman, E. J. Production of Hydroxyl Radical by Decomposition of Superoxide Spin-Trapped Adducts. *Molecular pharmacology*. 1982, pp 262–265.

Buettner, G. R. On the Reaction of Superoxide with DMPO/.OOH. *Free Radic. Res Com* **1990**,*10*(1–2),11–15.

Cheng, J.; Li, D.; Cheng, T.; Ren, B.; Wang, G.; Li, J. Aqueous Synthesis of High Fluorescence CdZnTe Alloyed Quantum Dots. *J. Alloys Compd.* **2014**, *589*, 539–544.

Li, W.; Liu, J.; Sun, K.; Dou, H.; Tao, K. Highly Fluorescent Water Soluble CdxZn1-xTe Alloyed Quantum Dots Prepared in Aqueous Solution: One-Step Synthesis and the Alloy Effect

ofZn.*J.Mater.Chem.***2010**,*20*(11),2133.

Wang, Q.; Fang, T.; Liu, P.; Deng, B.; Min, X.; Li, X. Direct Synthesis of High-Quality Water-Soluble CdTe:Zn 2+ Quantum Dots. *Inorg. Chem.* **2012**, *51* (17), 9208–9213.

Matos, C. R. S.; Candido, L. P. M.; Souza, H. O.; da Costa, L. P.; Sussuchi, E. M.; Gimenez, I. F. Study of the Aqueous Synthesis, Optical and Electrochemical Characterization of Alloyed ZnxCd1-xTe Nanocrystals. *Mater. Chem. Phys.* **2016**, *178*, 104–111.

Liu, F. C.; Cheng, T. L.; Shen, C. C.; Tseng, W. L.; Chiang, M. Y. Synthesis of Cysteine Capped ZnxCd1-xSe Alloyed Quantum Dots Emitting in the Blue-Green Spectral Range. *Langmuir***2008**,*24*(5),2162–2167.

Imlay, J. A. Iron-Sulphur Clusters and the Problem with Oxygen. *Molecular Microbiology*. 2006,pp1073–1082.

Imlay, J. A. Pathways of Oxidative Damage. *Annu. Rev. Microbiol.* **2003**, *57* (1), 395– 418.

Hawkins, C. L.; Davies, M. J. Generation and Propagation of Radical Reactions on Proteins. *Biochim.Biophys.Acta-Bioenerg.***2001**,*1504*(2–3),196–219.

Davies, M. J. Singlet Oxygen-Mediated Damage to Proteins and Its Consequences. *Biochem. Biophys.Res.Commun.***2003**,*305*(3),761–770.

Imlay, J. A.; Fridovich, I. Assay of Metabolic Superoxide Production in Escherichia Coli. *J. Biol. Chem.* **1991**, *266* (11), 6957–6965.